

2015

# Development of Multiscale Materials in Microfluidic Devices: Case Study for Viral Separation from Whole Blood

Krissada Surawathanawises  
*Lehigh University*

Follow this and additional works at: <http://preserve.lehigh.edu/etd>

 Part of the [Materials Science and Engineering Commons](#)

---

## Recommended Citation

Surawathanawises, Krissada, "Development of Multiscale Materials in Microfluidic Devices: Case Study for Viral Separation from Whole Blood" (2015). *Theses and Dissertations*. 2829.  
<http://preserve.lehigh.edu/etd/2829>

This Dissertation is brought to you for free and open access by Lehigh Preserve. It has been accepted for inclusion in Theses and Dissertations by an authorized administrator of Lehigh Preserve. For more information, please contact [preserve@lehigh.edu](mailto:preserve@lehigh.edu).

# **Development of Multiscale Materials in Microfluidic Devices: Case Study for Viral Separation from Whole Blood**

by

**Krissada Surawathanawises**

A Dissertation

Presented to the Graduate and Research Committee

of Lehigh University

in Candidacy for the Degree of

Doctor of Philosophy

in

Materials Science and Engineering

Lehigh University

August 2015

© 2015 Copyright  
Krissada Surawathanawises

## CERTIFICATE OF APPROVAL

Approved and recommended for acceptance as a dissertation in partial fulfillment of the requirements of the degree of Doctor of Philosophy

Krissada Surawathanawises

“Development of Multiscale Materials in Microfluidic Devices: Case Study for Viral Separation from Whole Blood”

---

Date

---

Xuanhong Cheng, Ph.D.  
Dissertation Advisor

---

Accepted Date

Committee Members:

---

Xuanhong Cheng, Ph.D.  
Committee Chair

---

John P. Coulter, Ph.D.  
Committee Member

---

Himanshu Jain, Ph.D.  
Committee Member

---

Wojciech Z. Misiolek, Ph.D.  
Committee Member

## ACKNOWLEDGEMENTS

I would like to specially thank my dissertation advisor, Xuanhong Cheng for her invaluable insight throughout my doctoral research, theoretically and practically. Also, thank you to the Materials Science and Engineering department at Lehigh University, and especially my committee members: Professors J.P. Coulter, H. Jain, and W. Misiolek for their advices in my research. Their all advices and knowledge have strengthened my research throughout in the field.

Besides, the supports from colleagues in the Cheng lab have been plentiful through the years of my work. Particularly, I thank C. Zhao for consults on computational fluid dynamics study and C. Multari for preparing biotinylated HIV solution and proofreading my writing. In addition, the Gilchrist lab is greatly thanked for sharing the binary suspension which is an important part of device fabrication. K. Kundrod, an undergraduate student, is a great assistant in fabrication and characterization of spherical pore matrix. She and J. Fraser also continue the research in developing a detection module which pushes the microfluidic technology toward diagnostics promisingly, and their work is really appreciated.

Moreover, my projects would not be accomplished without financial supports. I would like to acknowledge National institute of Allergy and Infectious Diseases (NIAID) under grant number 1R21AI081638 and Pennsylvania Department of Health CURE Formula. I am also very grateful for the support of Royal Thai Scholarship. Indispensably, I thank C. Beitler, M.D. T. Friel and the blood donors from Lehigh Valley Health Network who helped fulfilling my research.

Finally, I would like to recognize my family and friends for their support throughout my graduate life at Lehigh. Without their supports and cheering, I would not be able to step up for my defense. I am glad and wholeheartedly thank you all for being part of my life!

## TABLE OF CONTENTS

<b>List of Tables</b> .....	x
<b>List of Figures</b> .....	xi
<b>Abstract</b> .....	1
<b>Chapter 1: Introduction</b> .....	
1.1 Background and motivation .....	6
1.2 Separations and concentrations for bioparticles .....	8
1.3 Microfluidic technologies for bioparticle separation .....	11
1.4 Integration of multiscale separation in microfluidic devices .....	15
1.5 References .....	20
<b>Chapter 2: Nanoporous anodic aluminum oxide with a long-range order and tunable cell sizes by phosphoric acid anodization on pre- patterned substrates</b> .....	
2.1: Abstract .....	25
2.2: Introduction.....	27
2.3: Experimental details .....	30
2.3.1: Materials .....	30
2.3.2: Overview of the strategy to form tunable AAO pores through nanoimprinting .....	30
2.3.3: Creation of the nanoimprinting mold.....	32
2.3.4: Nanoimprinting of aluminum thin films.....	36
2.3.5: Anodization of nanoimprinted aluminum substrates .....	36
2.3.6: Sample Characterization .....	39
2.4: Results and Discussion .....	40

2.4.1: Nanoimprinting of aluminum thin films.....	40
2.4.2: Anodization of nanoimprinted aluminum substrates .....	45
2.4.3: Effect of anodization voltage on cell size, pore size and porosity.....	46
2.4.4: Effect of H <sub>3</sub> PO <sub>4</sub> concentration on growth rate of AAO films .....	48
2.5: Conclusions.....	57
2.6: References.....	58
<b>Chapter 3: Microfluidic Devices with Regular Macroporous Structures for HIV Viral Capture .....</b>	
3.1: Abstract.....	62
3.2: Introduction.....	64
3.3: Experimental details .....	66
3.3.1: Computational fluid dynamics simulation.....	66
3.3.2: Materials .....	67
3.3.3: Device fabrication.....	67
3.3.4: Sample characterization.....	71
3.3.5: Measurement of fluid permeability.....	71
3.3.6: Surface modification.....	71
3.3.7: Viral production.....	72
3.3.8: Viral capture in microfluidic devices.....	72
3.3.9: Capture of 100-nm fluorescent PS beads in microfluidic devices.....	73
3.4: Results and Discussion .....	74
3.4.1: Computational analysis of nanoparticles captured in porous media.....	74
3.4.2: Fabrication of PMMA and PS macroporous devices.....	79



3.4.3: Permeability in microchannels with macroporous matrices .....	83
3.4.4: Viral capture in microchannels with macroporous matrices .....	84
3.5: Conclusions.....	92
3.6: References.....	93
<b>Chapter 4: Micropatterned Macroporous Structures in Microfluidic Devices for Viral Separation from Whole Blood.....</b>	
4.1: Abstract.....	97
4.2: Introduction.....	99
4.3: Experimental details .....	101
4.3.1: Computational fluid dynamics simulation.....	101
4.3.2: Materials .....	103
4.3.3: Device fabrication.....	103
4.3.4: Sample characterization.....	106
4.3.5: Surface modification.....	106
4.3.6: Viral production.....	106
4.3.7: Transport of fluorescent micro- and nanobeads in the microfluidic device.....	107
4.3.8: Viral capture in the microfluidic devices.....	107
4.4: Results and Discussion .....	108
4.4.1: Computational analysis.....	109
4.4.2: Fabrication of microfluidic channels with multiscale features.....	114
4.4.3: Transport of fluorescent micro- and nanobeads in the devices .....	116
4.4.4: Viral capture in micropatterned devices .....	118

4.5: Conclusions.....	123
4.6: References.....	124
<b>Chapter 5: Summary and Future outlook .....</b>	
5.1: Summary.....	127
5.2: Future outlook.....	130
5.3: References.....	137
<b>Vita .....</b>	<b>138</b>

## LIST OF TABLES

<b>Table 1.1</b>	Conventional methods for viral separations .....	10
<b>Table 1.2</b>	Separation techniques in microfluidic technology.....	14
<b>Table 2.1</b>	Recipes for silica nanobead synthesis.....	34
<b>Table 2.2</b>	Suspension compositions and deposition rates of each nanobead sample .....	35
<b>Table 2.3</b>	Anodization conditions .....	38
<b>Table 3.1</b>	Physical characteristics of the flatbed and macroporous channels fabricated in this work. All channels for the permeability tests have a dimension of 25 mm × 8 mm × 30 μm (Length × Width × Thickness).....	82
<b>Table 4.1</b>	Design variables of micropattern geometry and layout for testing permeation volume fraction .....	102

## LIST OF FIGURES

- Figure 1.1** SEM images of highly ordered porous AAO template viewed from (A) top surface and (B) cross-section. (C) SEM image of a nickel nanopost array molded from the AAO template. (Reprinted from Yanagishita et al., Japanese Journal of Applied Physics 2006) .....18
- Figure 1.2** Schematic of (A) three dimensional assembly of microparticles surrounded by a continuous matrix and (B) spherical pores revealed after removal of microparticles. (C) SEM image of spherical pore network with small interconnected openings. (Reprinted from Gates et al., Chemistry of Materials 1999) .....19
- Figure 2.1** Schematic showing the process to fabricate highly ordered nanoporous AAO thin films by nanobead imprinting. (A) The deposition of monolayer of tightly packed silica as the imprinting mold. (B) A continuous monolayer of nanobeads covering a 3" x 1" glass slide. (C) Imprinting of nanobead mold onto an aluminum substrate. (D) An SEM image of hexagonally packed nanobead array used in (C). (E) The resulting nanodimples on aluminum surface serving as pore nucleation sites in the anodization process. (F) An SEM image of the ordered array of nanodimples matching patterns on the imprinting mold. The inset is a high magnification image showing the arrangement of the indents. (G) An AAO film with a pore arrangement comparable to the imprint mold. (H) A comparison of cell arrangement between patterned and unpatterned areas on the same AAO film. Scale bars are 2  $\mu\text{m}$  .....31
- Figure 2.2** SEM images showing the nanoparticle monolayers used as the imprinting molds (row (A)), the indented aluminum thin films (row (B)), surfaces of the anodized oxide films (row (C)) and cross-section views of anodized oxide films (row (D)). The features were created using monolayers of 280 nm (column 1), 410 nm (column 2), 500 nm (column 3), 645 nm (column 4) and 760 nm (column 5) silica nanoparticles, respectively. The images show a translation of the nanofeature arrangements from the molds to the AAO films. All scale bars are 2  $\mu\text{m}$  .....41
- Figure 2.3** A 500-nm nanobead mold after being used (A) 0, (B) 5, and (C) 10 times. The mold is mostly intact after reuse except for thin stripes (< 10  $\mu\text{m}$ ) silica beads lost from the mold edge. (D) An indented aluminum surface with nanobeads transferred from the mold edge. (E) Occasionally, small islands of nanobeads are lost inside the

	deposited monolayer after imprinting for 10 times. Scale bars are 2 cm in (A)-(C), 10 $\mu\text{m}$ in (D), and 30 $\mu\text{m}$ in (E).....	42
<b>Figure 2.4</b>	(A) An SEM image showing a large area of aluminum indented by 500-nm nanobead mold. (B) An SEM image showing an area of indentation boundary. The aluminum substrate can be indented over the whole surface to the mold boundary. Sometimes, a narrow band of silica beads is transferred from the mold edge to the aluminum surface after imprinting. All scale bars are 5 $\mu\text{m}$ .....	43
<b>Figure 2.5</b>	Topography of aluminum substrate indented by 760-nm beads measured by (A) SEM and (B) AFM. (C) The depth profile extracted from the dash line in (B). The indentation creates nanodimples with a depth of $69.26 \pm 3.75$ nm by AFM measurement. Using bead size of 760 nm and nanodimple opening of $448.69 \pm 13.93$ nm from SEM images, the depth of $73.45 \pm 5.08$ nm can be calculated by trigonometry, which matches the results from AFM measurement. All scale bars are 2 $\mu\text{m}$ .....	44
<b>Figure 2.6</b>	Relationship between the applied voltage ( $V_a$ , volt) and the resulting cell diameter ( $D_c$ , nm), pore diameters ( $D_p$ , nm), and porosity. The linear fit of the cell diameter versus voltage yields $D_c = 2.6038 \times V_a - 8.3497$ . The pore diameter also increases linearly with the anodization voltage by $D_p = 0.5997 \times V_a + 21.91$ . The porosity ( $P$ ) was calculated as $P = (\pi/2\sqrt{3})(D_p/D_c)^2$ , which varies between 6% and 9% in the cell size range fabricated .....	47
<b>Figure 2.7</b>	Relationship between the electrolytic concentration and film growth rate for different nanoindentation periods. For all the cell sizes, the film growth rate ( $GR$ , nm/hr) increases with the acid concentration ( $C$ , mol $\text{dm}^{-3}$ ). The best fittings for each series show an exponential growth rate: $GR = 311.3 \exp(0.3594 * C)$ for interpore distance of 280 nm; $GR = 219.34 \exp(2.187 * C)$ for interpore distance of 410 nm; $GR = 374.18 \exp(8.1051 * C)$ for interpore distance of 500 nm; $GR = 341.38 \exp(100.11 * C)$ for interpore distance of 645 nm; and $GR = 438.12 \exp(155.53 * C)$ for interpore distance of 760 nm. The dash lines indicate the critical concentrations leading to fast current surge within 60 seconds for each indentation period. Anodization of the 280 nm sample is stable even in the high concentration of phosphoric acid of 3 M .....	49
<b>Figure 2.8</b>	The profiles of current density of AAO film formed at 164 V in $\text{H}_3\text{PO}_4$ concentrations of 0.2M, 0.4M, and 0.6M (A) Current	

	profile as a function of time for 60 min. (B) Current density and AAO growth rate as a function of the $H_3PO_4$ concentration .....51
<b>Figure 2.9</b>	$H_3PO_4$ concentration as a function of the applied voltage for different growth rates. The black solid line predicts the critical concentrations which yield a breakdown.....53
<b>Figure 2.10</b>	The profiles of breakdown current density at critical concentrations in different applied voltages.....55
<b>Figure 3.1</b>	Schematics showing the fabrication processes of (A) PMMA and PS flatbed devices, (B) PMMA nanopost devices, and (C) PS spherical pore devices. (A1) A microchannel was formed on the substrate by manual embossing. (A2) The open channel was attached to a second flat sheet of the same material by epoxy glue, creating a flatbed microchannel. (B1) An array of PMMA nanoposts was fabricated through polymerizing MMA in an AAO template. (B2) The aluminum support was chemically removed and the newly opened top was attached to a PMMA roof by MMA and UV-polymerization. (B3) The PMMA nanopost device was created after chemically removing the AAO and sealing the sides. (C1) A binary suspension of silica and PS was deposited onto a PDMS mold. The PS beads were melted and glued to a PS substrate. (C2) The PDMS mold was detached and silica beads were etched away. (C3) A PS roof was attached to the PS porous structure and the sides were sealed, creating a PS spherical pore device .....70
<b>Figure 3.2</b>	Simulation results of streamlines in (A) a hexagonal array of circle islands, (B) an interconnected void array and (C) two parallel plates. The bold boundaries represent the affinity capture surface.....75
<b>Figure 3.3</b>	The effects of the separation distance, $D$ , on the capture efficiency are shown in (A) total capture efficiency, (B) capture efficiency normalized to the capture bed footprint and (C) capture efficiency normalized to the capture surface area.....78
<b>Figure 3.4</b>	Representative SEM images of the templates and the replicated structures. (A) An AAO template with hexagonal arranged pores within each domain. The inset shows a zoom-in image of the AAO pore structure. (B) Standing PMMA nanoposts after templating AAO. The inset shows the separation of the nanoposts. (C) A template of 3D packed silica beads with PS filling the interstitial space. (D) A network of PS porous structure after silica bead

	removal. Scale bars in (A) - (D) are 5 $\mu\text{m}$ and scale bars in the insets are 1 $\mu\text{m}$ .....	81
<b>Figure 3.5</b>	HIV virions captured on functionalized PMMA and PS flat substrates. The PMMA was functionalized with a fixed protocol but PS was exposed to different concentrations of NeutrAvidin from 0 to 20 $\mu\text{g}/\text{mL}$ . PS treated with 10 $\mu\text{g}/\text{mL}$ NeutrAvidin yielded a comparable amount of HIV viral capture to that on PMMA. The error bars represent standard deviation from 4 trials.....	85
<b>Figure 3.6</b>	HIV capture efficiency in the flatbed and macroporous devices with surface treatment by 1% BSA/PBS or NeutrAvidin. The error bars represent standard deviation from 4 trials .....	87
<b>Figure 3.7</b>	Physical retention of 100-nm fluorescent PS nanobeads in (A) a PMMA nanopost device and (B) a PS spherical pore device after rinsing. (C) Fluorescence intensity distribution along the channel length reveals greater non-specific binding of the fluorescent beads in the nanopost device. The error bars represent standard deviation from 3 trials.....	89
<b>Figure 4.1</b>	Schematics showing the fabrication process of half-ring micropatterns with solid or porous structures. (A) Deposition of binary suspension in a micro-patterned PDMS mold. (B) Transferring the micropatterned half-ring array to a flat substrate. The micropatterns are either (C) solid without silica bead removal or (D) containing interconnected spherical pores after silica bead removal. (E) Capping the array with a roof to form a microfluidic device. (F) Photograph of an assembled microfluidic device containing an array of half-ring micropatterns used for viral separation .....	105
<b>Figure 4.2</b>	Maps of fluid velocity magnitudes inside (A) circle, (B) half-circle, and (C) half-ring patterns. Flow is from the left to the right .....	110
<b>Figure 4.3</b>	Computational results showing the effect of (A) Gap distance $D$ , (B) outer radius $R$ , and (C) width $W_{hr}$ of half ring on the fluid volume fraction permeating into different porous designs .....	113
<b>Figure 4.4</b>	SEM images showing (A) a half-ring micropatterned array ( $D = 100 \mu\text{m}$ , $R = 150 \mu\text{m}$ , and $W_{hr} = 50 \mu\text{m}$ ). (B) A zoomed-in image showing a side wall of a solid post where silica beads are surrounded by a PS matrix. (C) A side wall of a patterned porous post showing pore openings on the surface after silica bead	

	removal. The side-wall openings were measured to be $695.38 \pm 55.95$ nm. All SEM images were taken at $\sim 50^\circ$ to $55^\circ$ tilted. Scale bars are $500 \mu\text{m}$ in (A) and $10 \mu\text{m}$ in (B) and (C) .....	115
<b>Figure 4.5</b>	Fluorescence images showing distribution of temporarily trapped $10\text{-}\mu\text{m}$ (green) and $100\text{-nm}$ (red) particles in a micropatterned porous device treated with 1% BSA/PBS. (A) While most of the beads flow through the device, a small number of microbeads accumulate in front of the microposts whereas some $100\text{-nm}$ beads penetrate inside the porous posts. The images were taken after 60 min. (B) While most of the $10\text{-}\mu\text{m}$ beads can be rinsed off, more $100\text{-nm}$ beads remain physically trapped inside the porous array after rinse .....	117
<b>Figure 4.6</b>	HIV capture efficiency in the solid and porous post devices under different flow rates from (A) blood plasma and (B) whole blood. The devices were functionalized by 1% BSA/PBS or NeutrAvidin. The error bars represent standard deviation from 4 samples. Statistical analysis was performed using a two-tailed Student's t-test at a 95% confidence interval .....	119
<b>Figure 5.1</b>	SEM images of (A) a micropatterned AAO array and (B) a zoom-in area of the dashed box in (A) showing PMMA nanoposts inside the AAO channels. Scale bars are $200 \mu\text{m}$ in (A) and $1 \mu\text{m}$ in (B) .....	133
<b>Figure 5.2</b>	SEM images of micropatterned AAO. (A) A non-uniform growth where the edge of the oxide film is thinner than in the center. The growth of AAO pores are tilted near the boundary between AAO and silica layer as shown in cross-sectioned views by (B) polishing and (C) cracking the AAO film. Scale bars are $10 \mu\text{m}$ .....	134



# Abstract

Separation and concentration of nanoscale species play an important role in various fields such as biotechnology, nanotechnology and environmental science. Inevitably, the separation efficiency strongly affects the quality of downstream detections or productions. For biotechnology and diagnostic applications, conventional separation techniques such as centrifugation, chromatography, filtration, and electrophoresis have been well established and the related instruments and reagents are readily available commercially. However, other factors such as cost, processing time, bulky instruments, infrastructure, and well trained technicians limit their applications in resource-limited settings. Consequently, innovations in materials science that can separate bionanoparticles efficiently and do not require complex setups, reagents or external fields are highly demanded.

This work focuses on developing new materials for the affinity separation of bionanoparticles such as viruses or macromolecules from a complex mixture, such as whole blood. To enhance the interaction between target nanoparticles and the capture bed, methods to produce porous matrices with a uniform pore size matching the dimension of targets are studied. Furthermore, regarding viral separation from whole blood, macroporous materials are further patterned into microarrays to allow multiscale separation. Considering the needs in resource-limited settings, these materials are integrated with microfluidic technologies to reduce the volume of samples and reagents, simplify operating processes, and enable the use of inexpensive and portable components.

Beyond the application of viral separation as demonstrated in the work, the fundamental study of macroporous material formation and transport in these materials also shed light to the separation of many other nanospecies in multiscale materials.

Specifically, two macroporous materials, based on template synthesis, are created in this work. The first type employs porous anodic aluminum oxide (AAO) films as the template to create hexagonal arrays of nanoposts. However, pore sizes and interpore distances (cell size) of ordered porous AAO films are limited by the conventional fabrication process. Moreover, the process usually yields defective pore morphologies and large pore and cell size distributions. To overcome these limitations, a patterning method using nanobead indentation on aluminum substrate prior to anodization is evaluated to control the growth of AAO. Together with controlled anodizing voltages and electrolytic concentrations, AAO pore and cell sizes are shown to be tunable and controllable with narrow size distributions within submicron range. A high degree of order of AAO pore arrangement is also demonstrated. In addition, overall anodization becomes more time-efficient and stable at high anodizing voltages.

Secondly, a three-dimensional (3D) assembly of microbeads is used as a template to fabricate a spherical pore network with small interconnected openings. After depositing and drying a suspension containing both micro- and nanobeads, the microbeads assemble into a 3D close-packed structure while the nanobeads fill the interstitial space. When the nanobeads are melted and microbeads are removed, a spherical pore matrix then form with small interconnected openings. Such the opening size is in submicron range can be adjusted depending on the size of microbead.

The advantages of the two macroporous materials are not only controllable and tunable pore size, but also high surface-to-volume ratio due to the nanoscale features. With a ratio on the order of  $\sim 1 \mu\text{m}^{-1}$ , the porous materials provide a significantly large binding surface. Computational and experimental results reveal that porous materials with a pore size matching the nanoparticle size are suitable for their capture. Separation of human immunodeficiency virus (HIV) is used as a model and capture yields of  $\sim 99\%$  and  $\sim 80\%$  are achieved in the nanopost structure and spherical pore network, respectively, after treated with a functional chemistry. Hence, the properties of these two macroporous materials are suitable as a size-exclusion and affinity separation for viral particles.

To further explore multiscale separation, i.e. capturing viruses from whole blood, micropatterned arrays of macroporous materials have been designed. In this design, a microscale gap allows the passage of microparticles such as blood cells, and the nanoscale pores promote permeation for affinity capture of bionanoparticles. Consequently, particles with a size difference of 3-4 orders of magnitude can be separated in a simple flow-through process. Computational analyses are employed to study the effect of micropattern shape and layout. A half-ring pattern is shown to reduce flow resistance and promote fluid permeation compared to a circular pattern. In the experiment, the micropatterned porous arrays yield around 4 times higher viral capture from whole blood compared with a micropatterned solid array. The micropatterned porous devices are capable of handling a large volume of fluid sample without clogging by cells. Therefore they can be used for nanoparticle concentration. Our study also

indicates that the layout of micropatterns can be adjusted to improve the capture yield. For example, an increase in pattern radius, or a decrease in gap distance between each post and in width of half ring will enhance fluid permeation in the porous structure. When combined with downstream detection, these materials integrated into microfluidic platforms can be created as point-of-care diagnostics, as well as other applications for particle separation and analysis.

# Chapter 1

## Introduction

This thesis aims to develop a microfluidic platform for viral separation and concentration as part of a diagnostic device. Alternative to conventional viral separation methods, microfluidic systems are widely introduced due to many advantages over the past decade. The scope of this thesis covers the study of macroporous materials and fabrications, transport behavior of bio-nanoparticles in microchannels, and the design of micro- and nanostructure for viral separation using microfluidic technology. This work has introduced macroporous materials which can be incorporated with a microfluidic device suitable for viral separation and concentration. The separation of human immunodeficiency virus (HIV) from human blood was demonstrated as a model in the study as part of the global health concern. This work has provided fundamental approaches using multiscale features for bioparticle separation and relying on physical and chemical interaction.

## **1.1: Background and motivation**

Human immunodeficiency virus (HIV) has caused 39 million human deaths and still infects more than 35 million people worldwide [1]. Due to limited resources, a large number of individuals are not aware of their HIV infection. Consequently, proper treatments are delayed while the viruses can be further spread without precaution. In addition, clinical tests for viral load measurement require a blood sample to be analyzed in a laboratory which could take weeks to receive the diagnostic results before a proper treatment can be provided. Also ones knowing individual's HIV status can prevent spreading HIV to other people. To improve accessibility of diagnostic technologies, the need of inexpensive and easy-to-use, and point-of-care devices has emerged for diagnostics and monitoring, especially to those in resource-limited regions.

Blood is a complex biological mixture which contains red blood cells, white blood cells, platelets, and around 55% plasma with more than thousands of soluble macromolecules and proteins [2]. In biopharmaceutical production, viral separations are essential to avoid viral contaminations in plasma-derived products [3-5]. In diagnostics, protein or viral separation from blood is strongly important for accurate and reliable diagnoses. Currently, HIV diagnostics is performed in clinical laboratory by enzyme immunoassay which detects immunoglobulin G (IgG) antibody detection in blood serum or oral fluid. Any inclusions in human plasma or hemoglobin in human blood cells may significantly reduce the amplification capacity of polymerase chain reaction (PCR) analysis [6-8]. Likewise, inclusions from blood may interfere with sensitivity of enzyme immunoassay (EIA) and result in inaccurate analysis [9]. Such hindered or interfered

interactions may lead to an inaccurate diagnosis and result in improper treatments. As far as it is concerned, efficient separation techniques are needed as an important step to successfully and accurately diagnose whether a person becomes infected or determine at what stage of infection a patient is.

Herein, we aim to develop a microfluidic device for blood processing that is low-cost and processed in a simple flow-through fashion to avoid complex setup and instruments. We focus on combining a micro pattern with nanoporous structures integrated in microfluidic devices for HIV separation and concentration. This approach relies on the high surface-to-volume ratio and the geometry of nanostructures to enhance viral capture efficiency; and also on a design of micropatterned porous array which allows more fluid permeation in a porous capture bed while exclude large particles off the device. This method shall provide an alternative POC device that can improve accessibility of diagnostic and monitoring health care.

## **1.2: Separations and concentrations for bioparticles**

Separations and concentrations of target species are a crucial step in various fields such as diagnostics [10-12], pharmaceutical production [13] as well as environmental safety [14, 15]. The need of particle separation can be for analytics, sample concentration or decontamination. Containing less interfering factors, properties of target particles can be characterized, analyzed, controlled, and quantified more accurately. In principle, separation methods rely on a difference in physical, chemical, electrical, optical or magnetic properties of particles. With that in mind, this thesis mainly focuses on separations of bio-nanoparticles for examples, viruses or other comparable sized particles and their proteins, from fluids.

Conventionally, separation methods can be broadly categorized, based on separation mechanisms, as centrifugation, chromatography, filtration, and electrophoresis. Nonetheless they can be combined to improve separation efficiency. Conventional methods for bioseparation have been widely explored in industrial and research scales. Many techniques are well established while the involved reagents and instruments are already available in the market. Target particles can be separated by individual property such as size, density, surface charge, polarizability, hydrophobicity, dissolubility, bioaffinity, or a combination of those properties. In one way or another, some methods offer advantages over the others such as processing time and reagent consumption, efficiency, and cost. Examples of conventional separation methods reviewed are summarized in Table 1.1.



With advanced technologies, more recent methods such as magnetic [16] and dielectrophoretic [17] separations have been developed with a high efficiency while some magnetic separators already become available commercially [16]. At the same time, the conventional methods have also been improved, combined, and modified specifically in various fields. Because of their sizes and densities, the cellular components can be appreciably separated by centrifugation, which usually involves in most of sample preparations. Yet, a separation of nanoparticles such as viruses or macromolecules may require a high speed centrifuge from 20,000 to 60,000 rpm which the instrument is not generally available in resource-limited area [16, 18]. The chromatographic and electrophoretic methods and have been widely used in diagnostics, biopharmaceutical industries, and research due to its high resolution of purification of proteins or viruses. Nonetheless, they may require multiple-step purification and a combination of reagents, complex setup, and very high power supplies [19]. Particularly for diagnostics, the expensive laboratory equipment, reagents, skilled technicians, and infrastructure are the factors that limit an access to diagnosis and treatment. To address these issues, there is a need for an inexpensive, simple-to-use, point-of-care, diagnostic device. Therefore, alternative separations are sought to further expand the access to diagnosis of infectious diseases such as HIV, hepatitis, or influenza viruses.

Table 1.1: Conventional methods for viral separations

<i>Separation methods</i>	<i>Target species</i>	<i>Sizes</i>	<i>Processing</i>	<i>Ref.</i>
<b>Centrifugation</b>				
Ultracentrifugation	Exosomes	50-100 nm	Centrifuge at 100,000×g at 4 °C for 1 hr	[16]
Gradient centrifugation	HIV-env gp160	~160 kD	Centrifuge in 5-20 % w/v sucrose gradients at 42,000 rpm at 4 °C for 14 hrs	[20]
<b>Chromatographic separation</b>				
Size-exclusion chromatography	Coronavirus	50-150 nm	Process in a 2.5 by 95 cm Sephacryl S-1000 column at 0.5 mL/min	[21]
Pseudoaffinity chromatography	Influenza virus	na	Use a high-performance monolithic disk affinity chromatography to separate the virus	
Hydrophobic interaction chromatography	Virus-like particles (VLP)	~22 nm	Involve in pre-filter steps and then separate VLPs from a buffer using a monolithic matrix	[22]
<b>Filtration</b>				
Ultra and microfiltration	MS2 virus	na	Separate MS2 from autoclaved water using ultra and micro filter membranes operated at constant pressure of 0.6-0.9 bar	[15]
<b>Electrophoresis</b>				
Gel electrophoresis	HIV virions and core particles	na	Separate virus or core particle using polyacrylamide gel electrophoresis for protein composition analysis	[23]
Capillary electrophoresis	Vaccinia virus	360×270×250 nm <sup>3</sup>	Apply a voltage of 10 kV across a bare fused-silica capillary of 30 cm	[10]

na = not available

### **1.3: Microfluidic technologies for bioparticle separation**

Microfluidic technology was developed from microelectromechanical systems (MEMS). In general, this technology shares common advantages of using a small volume of sample loads and chemical reagents, being inexpensive, and precisely controlling processes and interaction. Consequently, microfluidic devices has been explored in many applications. Microfluidic technology for particle separation has been widely demonstrated for different sizes and types of particles. Ones can achieve similar separation efficiency as those performed by conventional methods while instruments and reagents involved are miniaturized. For examples, Haeberle *et al.* utilized a centrifugal disk spinning at 40 Hz to perform a 2  $\mu\text{L}$  plasma separation with less than 0.1% of residual cell concentration extracted from a 5  $\mu\text{L}$  whole blood [24]. This method is a powerful and timely processing, but a high-speed rotator is required. Another technique using a hand-held egg beater, attached with a tubing loaded with blood, as a centrifuge was demonstrated by Wong *et al* [25]. Nevertheless, it induced hemolysis and resulted in intracellular contaminated in plasma. Cheng *et al.* [26] utilized microfluidic devices for CD4 T cell capture from whole blood while Nagrath *et al.* [27] further integrated a micropost array in a device to promote particle-surface interaction for circulating tumor cell separation. Their microfluidic systems worked well for the cellular size but may not serve for nanoparticles.

More specific approaches toward separation and concentration of targeted bio-nanoparticles, that are directly purified, have also been performed. An order of magnitude lower than cellular components, the HIV particle has an average size of 110-164 nm [28].

Hence the difference in particle sizes makes them feasible to be separated by using filter membranes. The pore size should be uniform and effective to allow smaller particles to pass through while larger particles to remain upfront. Wang and coworkers utilized polycarbonate track-etched membranes to separate HIV particle from blood cells [29]. However, the rapid clogging of filters is still the major drawback. Magnetic separation was also introduced in microfluidic systems. Kim *et al.* demonstrated the use carboxylated magnetic microbeads and fluorescence polystyrene nanobeads to perform HIV separation under a magnetic field [30]. The performance on bio-particle separation and concentration is also based on a surface affinity which is further related to a capture surface area. Consequently, nanoscale features play an important role as they provide a high surface-to-volume ratio. For example, Chen *et al.* performed an HIV separation using superparamagnetic nanoparticles which have overall higher surface area [31]. Nevertheless, the particle capture relies on chaotic mixing between two mobile species which is a random process and difficult to predict. Examples of microfluidic device for particle separation are summarized in Table 1.2. Putting all together, a separation method that requires less reagents and external fields, and provides a controllable and predictable process is still in need.

Beside the separation modules, a great amount of efforts on developing detection modules using microfluidic technologies have been demonstrated by research groups. Detection methods in microfluidic devices have relied on various approaches such as optical, electrical, biochemical, or magnetic detections. Although each technique may have an advantage one way or another over other techniques, they share common benefits

where the cost, time, and reagents are minimized. More of detection methods using microfluidic platforms can be found in the literature [32-36]. Eventually, combining two modules, sample preparation and detection, in a single device enable a new way of low-cost and relatively fast diagnostics and treatment monitoring.

Table 1.2: Separation techniques in microfluidic technology

<i>Separation methods</i>	<i>Target species</i>	<i>Sizes</i>	<i>Processing</i>	<i>Ref.</i>
<b>On-chip centrifugation</b>				
	Plasma separation	na	Extract 2 $\mu$ L plasma from 5 $\mu$ L blood using a disk rotation at 40 Hz	[24]
	Plasma separation	na	Attach the device to a hand-held egg beater and centrifuge	[25]
<b>Chromatographic separation</b>				
Size-exclusion chromatography	<i>Bacillus subtilis</i> spores	na	Separate the spores with microliter volumes at low pressure tested on different materials with pore size 5-100 nm and compare an optimum condition	[37]
Affinity + micropost array	Circulating tumor cells from blood	$\sim 10 \mu\text{m}$	Separate tumor cells from whole blood using a functionalized device integrated with a micropost array to enhance particle-surface interaction	[27]
Affinity + micropatterned porous array	CD4+ T cells, <i>E. coli</i> bacteria, Avidin coated beads, Bovine serum albumin	$\sim 10 \mu\text{m}$ $\sim 1 \mu\text{m}$ 40 nm $\sim 10 \text{nm}$	Utilize a micropattern of highly nanoporous CNT elements to separate particles within 3 orders of magnitude difference. The large particles can travel around while the small particles can be captured in front or inside the porous elements	[38]
<b>Electrophoresis</b>				
Capillary gel electrophoresis	Six amino acids in buffer	na	Separate amino acids in 28 cm long oxidized PDMS channel by applying 5 kV	[39]
<b>Membrane-based separation</b>				
Track-etched membranes	HIV in blood	na	Filter HIV from whole blood through the membranes of different pore sizes from 0.4 to 3 $\mu\text{m}$	[29]
<b>Magnetic separation</b>				
Magnetic beads	HIV in plasma	na	Mix superparamagnetic beads coated with anti-CD44 and HIV virions by a passive mixer, and separate HIV-captured beads by a magnetic separator	[31]

na = not available

#### **1.4: Integration of multiscale separation in microfluidic devices**

Using the state-of-the-art technology, microfluidic devices can be fabricated from various materials including silicon [40, 41], polymers [29, 42, 43] or glass [44]. However, devices made of polymers are cost-effective compared with other materials. Moreover, they are made disposable to avoid contamination between samples. Beside the ease of fabrication, the surface of polymer devices can be modified chemically or biologically inside the channel to enhance the performance and specificity of the devices [27, 35, 38, 43, 45].

As mentioned before that microfluidic devices have been developed for separation applications, most of the devices contain only a single feature either micro or nanoscale for a specific separation. Those devices renders the need of pre-purify processes to before final target can be separated from a mixture. In contrast, ones that can separate target species within one or two steps are highly desired and suitable for POC device. Such the device platform may contain multiscale features in order to manipulate different particle sizes within a single module. Up to date, only a few work demonstrated the use of multiscale elements for particle separation [38, 46]. Fachin *et al.* [46] introduced a concept of micropattern of nanoporous elements made of vertically aligned carbon nanotubes (CNTs) while Chen *et al.* [38] further utilized the micropatterned porous CNT device for separating particles in three orders of magnitude difference in size. Interestingly, with the design and integration of multiscale porous elements, different sized particles can be either retained or excluded within a simple flow-through process.

Nevertheless, the spacing of CNTs was controllable upto 80 nm which still limit an entrance of larger nanoparticles such as HIV.

In order to deal with the limited pore or spacing size, different materials possessing controllable pore sizes in submicron range are sought. Two different materials with interconnected open pores were reported in literature. First, nanoporous anodic aluminum oxide (AAO) films containing hexagonally self-ordered array of straight-through pores have been reported in literature (Figure 1.1(A)-(B)) [47-50]. The ordered straight nanopore array with pore sizes in range of a few tens to hundreds of nanometers makes AAO films interesting in various fields. Yanagishita *et al.* demonstrated that AAO films could be used as a template to fabricate an ordered array of nanoposts (Figure 1.1(C)) and further for an ordered porous polymer membrane [50]. Moreover, Chen *et al.* utilized AAO as a template to fabricate an ordered array of PMMA nanopost with an aspect ratio (height to width) of more than 300 [51]. Such the high aspect ratio was a result of lyophilization that prevented nanoposts from collapsing due to surface tension from solvent evaporation. The spacing between each nanopost can be used for size-exclusion, especially for nanoparticles.

Another ordered porous material is a 3D network of spherical pores. Such the structure can be obtained by constructing a 3D packing of microbeads and introducing a second material filling in the space between the microbead structure. Then the microbeads can be selective etched leaving a porous structure with small interconnected openings between the spherical pores [52]. Gates *et al.* performed a 3D packing of monodispersed either silica or polystyrene (PS) microbeads in a “packing cell” (Figure



1.2(A)-(B)) [53]. A UV-curable or thermally cross-linkable prepolymer was introduced in between the structure. An interconnected opening size of 250 nm porous polyurethane was obtained after removing 1  $\mu\text{m}$  PS beads (Figure 1.2(C)). Weldon *et al.* also fabricated thin PS spherical porous films through a binary suspension of silica-PS micro/nanobeads [54]. By melting the PS nanobeads and etching the silica beads away, spherical pore network with interconnected openings was revealed.

These two porous materials show an ordered structure with uniform pore size. Moreover pore size or spacing between each post can be adjusted in submicron range and also comparable to HIV particle size. Thus it is of interest to utilize the two materials and incorporate with a micropattern array for viral separation.

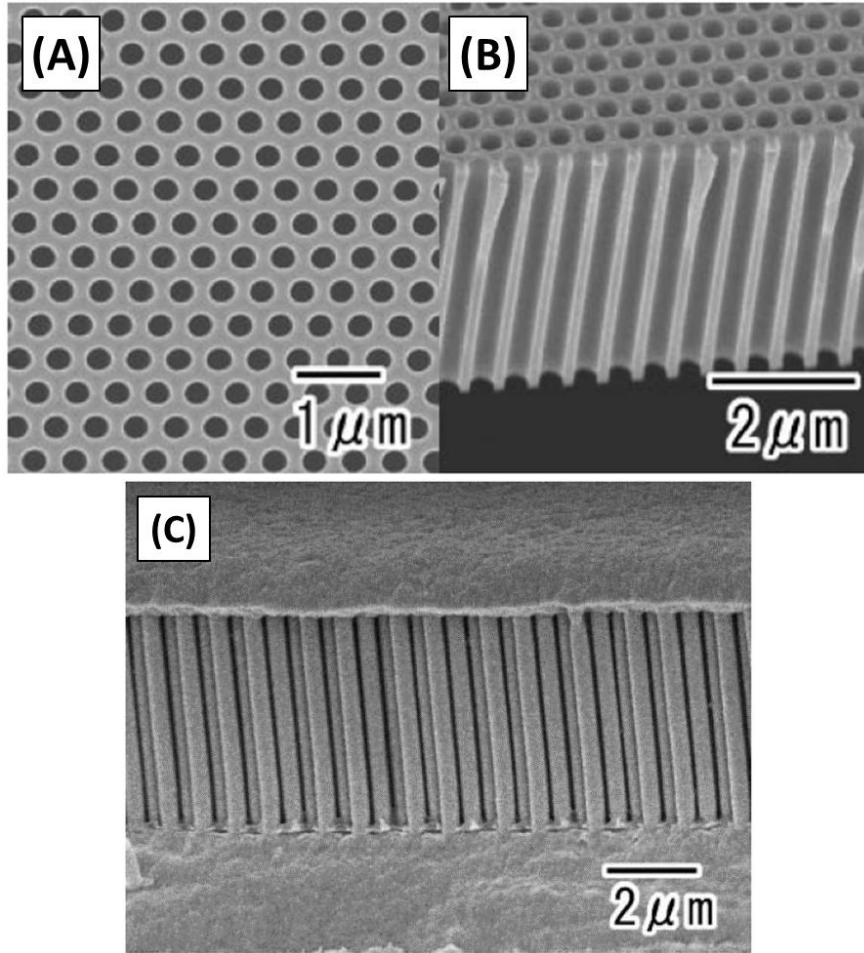


Figure 1.1: SEM images of highly ordered porous AAO template viewed from (A) top surface and (B) cross-section. (C) SEM image of a nickel nanopost array molded from the AAO template. (Reprinted from Yanagishita *et al.*, *Japanese Journal of Applied Physics* 2006) [50]

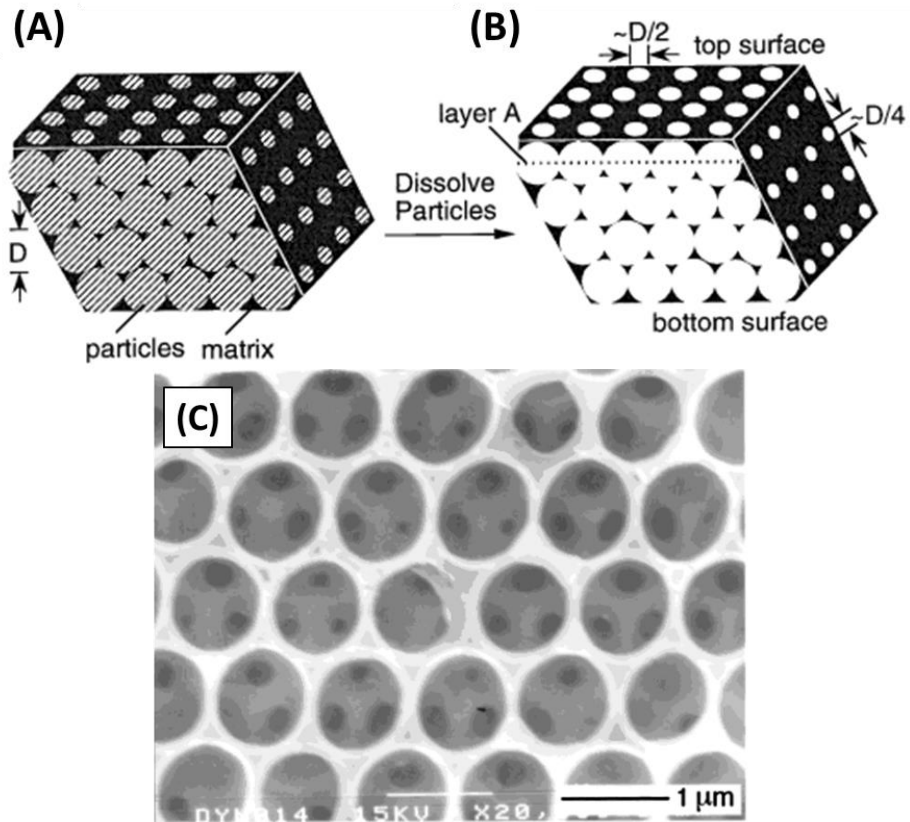


Figure 1.2: Schematic of (A) three dimensional assembly of microparticles surrounded by a continuous matrix and (B) spherical pores revealed after removal of microparticles. (C) SEM image of spherical pore network with small interconnected openings. (Reprinted from Gates *et al.*, *Chemistry of Materials* 1999) [53]

## **1.5: References**

1. *Global Health Observatory (GHO) - HIV/AIDS*. Available from: <http://www.who.int/gho/hiv/en/index.html>.
2. Kuo, J.-N. and Y.-H. Zhan, *Microfluidic chip for rapid and automatic extraction of plasma from whole human blood*. Microsystem Technologies, 2013: p. 1-7.
3. Burnouf, T. and M. Radosevich, *Nanofiltration of plasma-derived biopharmaceutical products*. Haemophilia, 2003. **9**(1): p. 24-37.
4. *Guidelines on viral inactivation and removal procedures intended to assure the viral safety of human blood plasma products*, in *WHO Technical Report, Series No. 924*. 2004, World Health Organization.
5. Dichtelmüller, H.O., et al., *Effective virus inactivation and removal by steps of Biotest Pharmaceuticals IGIV production process*. Results in Immunology, 2012. **2**(0): p. 19-24.
6. Abu Al-Soud, W., L.J. Jonsson, and P. Radstrom, *Identification and characterization of immunoglobulin G in blood as a major inhibitor of diagnostic PCR*. Journal of Clinical Microbiology, 2000. **38**(1): p. 345-350.
7. Abu al-Soud, W. and P. Radstrom, *Purification and characterization of PCR-inhibitory components in blood cells*. Journal of Clinical Microbiology, 2001. **39**(2): p. 485-493.
8. Wiedbrauk, D.L., J.C. Werner, and A.M. Drevon, *Inhibition of PCR by aqueous and vitreous fluids*. Journal of Clinical Microbiology, 1995. **33**(10): p. 2643-2646.
9. Raivio, T., et al., *Comparison of a Novel Whole Blood Transglutaminase-based ELISA With a Whole Blood Rapid Antibody Test and Established Conventional Serological Celiac Disease Assays*. Journal of Pediatric Gastroenterology and Nutrition, 2008. **47**(5): p. 562-567.
10. Mironov, G.G., et al., *Viral quantitative capillary electrophoresis for counting intact viruses*. Analytical Chemistry, 2011. **83**(13): p. 5431-5435.
11. Stevens, S.J.C., I. Pronk, and J.M. Middeldorp, *Toward standardization of Epstein-Barr virus DNA load monitoring: Unfractionated whole blood as preferred clinical specimen*. Journal of Clinical Microbiology, 2001. **39**(4): p. 1211-1216.

12. Towner, J.S., et al., *Rapid diagnosis of Ebola hemorrhagic fever by reverse transcription-PCR in an outbreak setting and assessment of patient viral load as a predictor of outcome*. Journal of Virology, 2004. **78**(8): p. 4330-4341.
13. Morenweiser, R., *Downstream processing of viral vectors and vaccines*. Gene Therapy, 2005. **12**: p. S103-S110.
14. Lopez-Sabater, E.I., M.Y. Deng, and D.O. Cliver, *Magnetic immunoseparation PCR assay (MIPA) for detection of hepatitis A virus (HAV) in American oyster (Crassostrea virginica)*. Letters in Applied Microbiology, 1997. **24**(2): p. 101-104.
15. Fiksdal, L. and T. Leiknes, *The effect of coagulation with MF/UF membrane filtration for the removal of virus in drinking water*. Journal of Membrane Science, 2006. **279**(1-2): p. 364-371.
16. Taylor, D.D., W. Zacharias, and C. Gercel-Taylor, *Exosome isolation for proteomic analyses and RNA profiling*. Methods Mol. Biol., 2011. **728**: p. 235-246.
17. Gascoyne, P.R.C. and J. Vykoukal, *Particle separation by dielectrophoresis*. Electrophoresis, 2002. **23**(13): p. 1973-1983.
18. Hou, H.W., et al., *Microfluidic Devices for Blood Fractionation*. Micromachines, 2011. **2**(3): p. 319-343.
19. Liu, H.F., et al., *Recovery and purification process development for monoclonal antibody production*. MAbs, 2010. **2**(5): p. 480-99.
20. Earl, P.L., R.W. Doms, and B. Moss, *Oligomeric structure of the human immunodeficiency virus type-1 envelope glycoprotein*. Proceedings of the National Academy of Sciences of the United States of America, 1990. **87**(2): p. 648-652.
21. Loa, C.C., et al., *Purification of turkey coronavirus by Sephacryl size-exclusion chromatography*. Journal of Virological Methods, 2002. **104**(2): p. 187-194.
22. Burden, C.S., et al., *A monolith purification process for virus-like particles from yeast homogenate*. Journal of Chromatography B-Analytical Technologies in the Biomedical and Life Sciences, 2012. **880**: p. 82-89.
23. Welker, R., et al., *Biochemical and structural analysis of isolated mature cores of human immunodeficiency virus type 1*. Journal of Virology, 2000. **74**(3): p. 1168-1177.
24. Haeberle, S., et al., *Centrifugal extraction of plasma from whole blood on a rotating disk*. Lab on a Chip, 2006. **6**(6): p. 776-781.

25. Wong, A.P., et al., *Egg beater as centrifuge: isolating human blood plasma from whole blood in resource-poor settings*. Lab on a Chip, 2008. **8**(12): p. 2032-2037.
26. Cheng, X., et al., *A microfluidic device for practical label-free CD4+T cell counting of HIV-infected subjects*. Lab on a Chip, 2007. **7**(2): p. 170-178.
27. Nagrath, S., et al., *Isolation of rare circulating tumour cells in cancer patients by microchip technology*. Nature, 2007. **450**(7173): p. 1235-1239.
28. Gentile, M., et al., *Determination of the size of HIV using adenovirus type-2 as an internal length marker*. Journal of Virological Methods, 1994. **48**(1): p. 43-52.
29. Wang, S.Q., et al., *Simple filter microchip for rapid separation of plasma and viruses from whole blood*. International Journal of Nanomedicine, 2012. **7**: p. 5019-5028.
30. Kim, B.C., et al., *Quantitative detection of HIV-1 particles using HIV-1 neutralizing antibody-conjugated beads*. Anal Chem, 2009. **81**(6): p. 2388-2393.
31. Chen, G.D., et al., *Concentration and purification of human immunodeficiency virus type 1 virions by microfluidic separation of superparamagnetic nanoparticles*. Analytical Chemistry, 2010. **82**(2): p. 723-728.
32. Oita, I., et al., *Microfluidics in macro-biomolecules analysis: macro inside in a nano world*. Analytical and Bioanalytical Chemistry, 2010. **398**(1): p. 239-264.
33. Clerc, O. and G. Greub, *Routine use of point-of-care tests: usefulness and application in clinical microbiology*. Clinical Microbiology and Infection, 2010. **16**(8): p. 1054-1061.
34. McCalla, S.E. and A. Tripathi, *Microfluidic Reactors for Diagnostics Applications*, in *Annual Review of Biomedical Engineering, Vol 13*, M.L. Yarmush, J.S. Duncan, and M.L. Gray, Editors. 2011, Annual Reviews: Palo Alto. p. 321-343.
35. Cheng, X.H., G. Chen, and W.R. Rodriguez, *Micro- and nanotechnology for viral detection*. Analytical and Bioanalytical Chemistry, 2009. **393**(2): p. 487-501.
36. Julian, T.R. and K.J. Schwab, *Challenges in environmental detection of human viral pathogens*. Current Opinion in Virology, 2012. **2**(1): p. 78-83.
37. Chirica, G., J. Lachmann, and J. Chan, *Size exclusion chromatography of microliter volumes for on-line use in low-pressure microfluidic systems*. Analytical Chemistry, 2006. **78**(15): p. 5362-5368.

38. Chen, G.D., et al., *Nanoporous elements in microfluidics for multiscale manipulation of bioparticles*. *Small*, 2011. **7**(8): p. 1061-1067.
39. Duffy, D.C., et al., *Rapid prototyping of microfluidic systems in poly(dimethylsiloxane)*. *Analytical Chemistry*, 1998. **70**(23): p. 4974-4984.
40. Crowley, T.A. and V. Pizziconi, *Isolation of plasma from whole blood using planar microfilters for lab-on-a-chip applications*. *Lab on a Chip*, 2005. **5**(9): p. 922-929.
41. Grayson, A.C.R., et al., *A BioMEMS review: MEMS technology for physiologically integrated devices*. *Proceedings of the Ieee*, 2004. **92**(1): p. 6-21.
42. Yager, P., et al., *Microfluidic diagnostic technologies for global public health*. *Nature*, 2006. **442**(7101): p. 412-418.
43. Sia, S.K. and G.M. Whitesides, *Microfluidic devices fabricated in poly(dimethylsiloxane) for biological studies*. *Electrophoresis*, 2003. **24**(21): p. 3563-3576.
44. Gao, Y.K., et al., *Plasmonic Mach-Zehnder Interferometer for Ultrasensitive On-Chip Biosensing*. *Acs Nano*, 2011. **5**(12): p. 9836-9844.
45. Malmstadt, N., et al., *A smart microfluidic affinity chromatography matrix composed of poly(N-isopropylacrylamide)-coated beads*. *Analytical Chemistry*, 2003. **75**(13): p. 2943-2949.
46. Fachin, F., et al., *Integration of bulk nanoporous elements in microfluidic devices with application to biomedical diagnostics*. *Journal of Microelectromechanical Systems*, 2011. **20**(6): p. 1428-1438.
47. Masuda, H., K. Yada, and A. Osaka, *Self-Ordering of Cell Configuration of Anodic Porous Alumina with Large-Size Pores in Phosphoric Acid Solution*. *Japanese Journal of Applied Physics Part 2-Letters*, 1998. **37**(11A): p. L1340-L1342.
48. Masuda, H., F. Hasegawa, and S. Ono, *Self-Ordering of Cell Arrangement of Anodic Porous Alumina Formed in Sulfuric Acid Solution*. *Journal of the Electrochemical Society*, 1997. **144**(5): p. L127-L130.
49. Masuda, H. and K. Fukuda, *Ordered Metal Nanohole Arrays Made by a 2-Step Replication of Honeycomb Structures of Anodic Alumina*. *Science*, 1995. **268**(5216): p. 1466-1468.
50. Yanagishita, T., K. Nishio, and H. Masuda, *Polymer through-hole membranes with high aspect ratios from anodic porous alumina templates*. *Japanese Journal of*

Applied Physics Part 2-Letters & Express Letters, 2006. **45**(42-45): p. L1133-L1135.

51. Chen, G., S.A. Soper, and R.L. McCarley, *Free-standing, erect ultrahigh-aspect-ratio polymer nanopillar and nanotube ensembles*. Langmuir, 2007. **23**(23): p. 11777-11781.
52. Yang, P.D., et al., *Patterning porous oxides within microchannel networks*. Advanced Materials, 2001. **13**(6): p. 427-431.
53. Gates, B., Y.D. Yin, and Y.N. Xia, *Fabrication and characterization of porous membranes with highly ordered three-dimensional periodic structures*. Chemistry of Materials, 1999. **11**(10): p. 2827-2836.
54. Weldon, A.L., et al., *Fabrication of macroporous polymeric membranes through binary convective deposition*. ACS Applied Materials & Interfaces, 2012. **4**(9): p. 4532-4540.



## Chapter 2

# Nanoporous anodic aluminum oxide with a long-range order and tunable cell sizes by phosphoric acid anodization on pre-patterned substrates

### **2.1: Abstract**

Nanoporous anodic aluminum oxide (AAO) has been explored for various applications due to its regular cell arrangement and relatively easy fabrication processes. However, conventional two-step anodization based on self-organization only allows the fabrication of a few discrete cell sizes and formation of small domains of hexagonally packed pores. Recent efforts to pre-pattern aluminum followed with anodization significantly improve the regularity and available pore geometries in AAO, while systematic study of the anodization condition, especially the impact of acid composition on pore formation guided by nanoindentation is still lacking. In this work, we pre-patterned aluminum thin films using ordered monolayers of silica beads and formed

porous AAO in a single-step anodization in phosphoric acid. Controllable cell sizes ranging from 280 nm to 760 nm were obtained, matching the diameters of the silica nanobead molds used. This range of cell size is significantly greater than what has been reported for AAO formed in phosphoric acid in the literature. In addition, the relationships between the acid concentration, cell size, pore size, anodization voltage and film growth rate were studied quantitatively. The results are consistent with the theory of oxide formation through an electrochemical reaction. Not only does this study provide useful operational conditions of nanoindentation induced anodization in phosphoric acid, it also generates significant information for fundamental understanding of AAO formation.

## **2.2: Introduction**

Owing to its self-ordered pore arrangement, straight through-pore geometries and ready availability out of a clean room environment, nanoporous anodic aluminum oxide (AAO) is attractive to numerous applications such as electrical and optical sensing, separating molecules and particles, as well as templating various nanostructures [1-10]. Conventionally, AAO films with self-ordered nanoporous structures are fabricated following a two-step anodization process developed by Masuda *et al* [10-12]. Although various anodization parameters have been studied in great detail, only a few discrete cell sizes are available using the self-ordering method. These are determined mainly by the applied voltage and type of acids used: for example, sulfuric acid at 25 V, oxalic acid at 40 V and phosphoric acid at 195 V give 63 nm, 100 nm and 500 nm pore intervals, respectively [13]. When an anodization of aluminum is carried out outside of these narrow process windows, the degree of spatial organization decreases considerably. Another shortcoming of the self-ordering method is the need of long anodization time and a relatively thick aluminum layer. Thus, the method does not apply easily to aluminum thin films deposited on a substrate [14]. Furthermore, the domain size with hexagonal packed pores is limited to several micrometers; it is difficult to obtain long range order through the self-organization process.

As an alternative to the self-ordered anodization, pre-patterning techniques to modify an aluminum surface prior to anodization have been introduced to improve a long-range order of AAO cell array, promote tunable cell sizes, reduce the anodization time and enable straight pores in thin aluminum films on different substrates. The

indented topographic features produce a high local electric field, which enhances dissolution of the oxide film and serve as pore nucleation sites [15]. Shallow indentations have been created from various molds. For example, Masuda *et al.* used a SiC mold containing hexagonal array of convexes created by e-beam lithography to produce highly ordered AAO films [16]. Mikulskas *et al.* used an optical diffraction grating as an imprinting mold to pattern an aluminum surface [17]. However, the small dimension and high cost of the fabricated molds limit their wide applications. Alternatively, focused ion beam drilling has been used to indent aluminum directly [18, 19], while the patterned area is limited to the 10-100  $\mu\text{m}$  order due to the slow and serial indentation process. Various approaches to pattern a large area of aluminum for ordered AAO have been reported. Ordered arrays of nickel bumps or pyramids have been created by interference lithography and used as a stamping mold for wafer-scale anodization [20]. Holographic lithography has also been employed to create photoresist grating patterns on a thin film aluminum and form highly ordered AAO [21]. Recently, a combination of imprinting lithography and wet etching has been carried out to grow highly ordered AAO on a 4-in silicon wafer [22]. However, these nano-lithographic patterning techniques require sophisticated clean room facilities and are not easily accessible. On the other hand, several groups have utilized nanobeads of 13-500 nm in diameter to imprint an aluminum surface and guide highly ordered pores in AAO [23, 24]. The nanobead molds offer an advantage over other imprinting methods in that no clean room access is required and continuously tunable bead sizes are easily available [23-25]. Moreover, nanobeads can be

patterned into long range hexagonally ordered domains in scalable processes [26], enabling large area AAO formation through pre-patterning.

Despite numerous reports on pre-patterning guided anodization, prior work has focused on pattern transfer from the mold to the oxide film; there is little knowledge about how the electrolyte composition affects the oxide formation. Additionally, cell size of ordered AAO is limited to below 500nm, even with the nanoindentation approach. To address these limitations, we report here an investigation of oxide film growth rate as a function of acid concentration for cell sizes in a wide range through pre-patterned aluminum anodization in phosphoric acid. We use monolayers of hexagonally packed silica nanobeads as the imprinting mold to control the cell size between 280 to 760 nm. In addition to the acid concentration, the relationships between cell size, intrinsic pore size, anodization voltage and oxide film growth rate are also studied quantitatively.

## **2.3: Experimental details**

### **2.3.1 Materials**

Tetraethyl orthosilicate (TEOS) was obtained from Sigma-Aldrich (St. Louis, MO). Ethanol (EtOH) – 200 proof was obtained from Pharmco-AAPER (Brookfield, CT). Ammonium hydroxide (NH<sub>4</sub>OH) and premium plain glass microscope slides were purchased from Fisher Scientific (Pittsburgh, PA). Phosphoric acid (H<sub>3</sub>PO<sub>4</sub>) was purchased from Alfa Aesar (Ward Hill, MA).

### **2.3.2 Overview of the strategy to form tunable AAO pores through nanoimprinting**

The schematic in Figure 2.1 demonstrates the process to fabricate highly ordered nanoporous AAO thin films by nanobead imprinting. The process starts from depositing silica nanoparticles into a large, continuous and close-packing monolayer on glass slides by the convective deposition [27] (Figure 2.1(A)-(B)). Polystyrene nanobeads are mixed into the suspension at a concentration of 4 vol%, co-deposited and melted afterwards to stabilize the silica monolayer. The silica monolayer is then used as a template mold to imprint an aluminum thin film (Figure 2.1(C)-(D)). The resulting nanodimple arrays on the aluminum surface (Figure 2.1(E)-(F)) serve as pore nucleation sites in subsequent anodization and guide the formation of straight pores of the desired pore size in phosphoric acid under a constant voltage (Figure 2.1(G)-(H)).

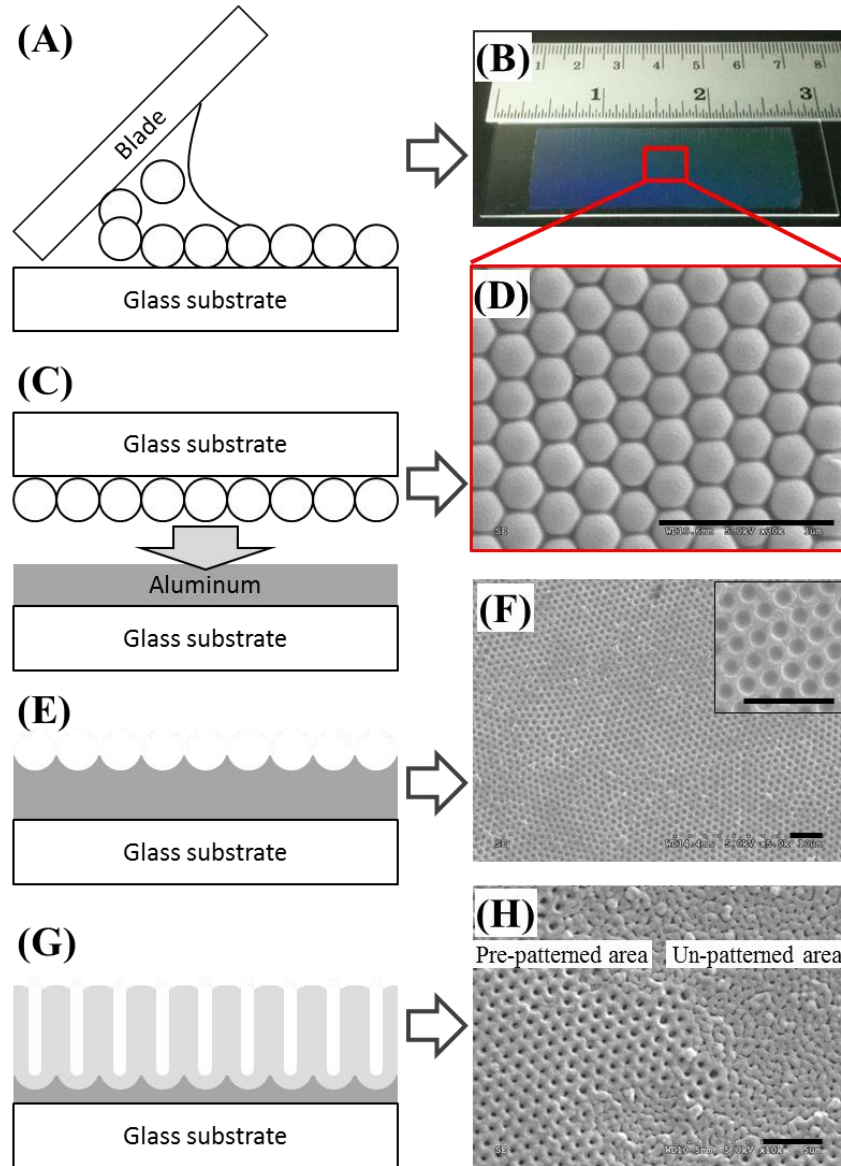


Figure 2.1: Schematic showing the process to fabricate highly ordered nanoporous AAO thin films by nanobead imprinting. (A) The deposition of monolayer of tightly packed silica as the imprinting mold. (B) A continuous monolayer of nanobeads covering a 3" × 1" glass slide. (C) Imprinting of nanobead mold onto an aluminum substrate. (D) An SEM image of hexagonally packed nanobead array used in (C). (E) The resulting nanodimples on aluminum surface serving as pore nucleation sites in the anodization process. (F) An SEM image of the ordered array of nanodimples matching patterns on the imprinting mold. The inset is a high magnification image showing the arrangement of the indents. (G) An AAO film with a pore arrangement comparable to the imprint mold. (H) A comparison of cell arrangement between patterned and un-patterned areas on the same AAO film. Scale bars are 2 μm.

### 2.3.3 Creation of the nanoimprinting mold

Monodispersed silica nanobeads were synthesized by hydrolysis of TEOS following a recipe modified from the literature [25]. Deionized (DI) water, ethanol,  $\text{NH}_4\text{OH}$  and TEOS were mixed at different ratios (Table 2.1) and left to react at room temperature for 24 hours under continuous stirring. The synthesized silica nanobeads were in the range of 280 nm to 760 nm with a narrow size distribution (Table 2.1). After multiple washes by DI water and concentration by centrifugation, suspensions of the nanobeads were diluted to 16 vol% in DI water. Close-packed silica-nanobead monolayers were prepared through convective deposition on plain glass slides following the method reported by Kumnorkaew [27]. The deposition blade, a parafilm treated glass slide, was positioned at  $45^\circ$  above the substrate and 10  $\mu\text{l}$  of silica bead suspension was pipetted between the substrate and blade. The substrate was then linearly translated at 500-550  $\mu\text{m}/\text{min}$  to deposit a monolayer of silica beads (Table 2.2). To promote a long-range order in the monolayer of Si nanoparticles, 100-nm polystyrene nanobeads was also mixed into the silica bead suspension at a final concentration of 4 vol% except for the 280-nm silica bead samples where polystyrene nanoparticles were not added due to an interference to silica hexagonal packing. After deposition on a whole glass slide of 3"  $\times$  1", the slide was cut and the deposition area was manually patterned into a 10 mm  $\times$  20 mm region for nanoimprinting. Beads outside the region were removed by a blade and wiped. This step is necessary to reach the desirable indentation pressure under the maximal available force on the universal testing instrument (Instron 5500 R). Subsequently, the slides were heated to 240  $^\circ\text{C}$  for 5 min to melt the polystyrene



nanobeads, which strengthen the integrity of the silica monolayer and allow for multiple use of each deposition.

Table 2.1: Recipes for silica nanobead synthesis

<b>Solution 1</b>				<b>Solution 2</b>		<b>Average diameter (nm)</b>
<b>EtOH (g)</b>	<b>DI (g)</b>	<b>NH<sub>4</sub>OH (g)</b>	<b>20 vol% 500-nm silica nanobeads*</b>	<b>TEOS (g)</b>	<b>EtOH (g)</b>	
13.635	24.969	7.010	-	0.9731	31.900	278.87±14.00
13.633	24.970	7.010	-	3.8412	31.991	408.06±24.17
13.631	24.900	7.034	690 uL	0.972	35.650	497.67±11.66 *
13.639	24.953	7.035	690 uL	2.146	35.710	646.63±27.01
						759.57±17.04

\*The 500-nm silica nanobeads were obtained from Fusco Chemical Co., Ltd., Japan

Table 2.2: Suspension compositions and deposition rates of each nanobead sample

<i>Nanobead samples</i>	<i>Suspension composition</i>	<i>Deposition rate (<math>\mu\text{m}/\text{min}</math>)</i>
SiO <sub>2</sub> -280*	16% SiO <sub>2</sub>	510
SiO <sub>2</sub> -410*	16% SiO <sub>2</sub> / 4% PS**	500
SiO <sub>2</sub> -500*	16% SiO <sub>2</sub> / 4% PS**	500
SiO <sub>2</sub> -645*	16% SiO <sub>2</sub> / 4% PS**	500
SiO <sub>2</sub> -760*	16% SiO <sub>2</sub> / 4% PS**	550

\*The numbers refer to the diameter of the silica beads.

\*\* Polystyrene beads are 100 nm in all cases.

### **2.3.4 Nanoimprinting of aluminum thin films**

An aluminum film of five micrometers thick was evaporated onto clean glass slides using an electron-beam evaporator (Indel Systems-2602). The e-beam gun was a Telemark 4 pocket gun assembly with the Telemark TT-6 power supply, and controlled with a Sycon Systems STC-200/SQ Deposition Rate Controller. The aluminium source was 99.99% pure. Glass slides were cleaned by piranha solution and evaporation was carried out at a starting vacuum level of  $1.1 \times 10^{-7}$  torr. The deposition rate was 2-5 angstrom per second.

The silica monolayer was then pressed onto the aluminum surface at a pressure of  $30 \text{ kN/cm}^2$  for 30 seconds using the Instron instrument to create a pattern of nanodimple arrays. This imprinting pressure was optimized to create dimples without cracking the glass substrates. As mentioned above, the silica nanoparticles were patterned onto an area of  $10 \text{ mm} \times 20 \text{ mm}$  to satisfy this pressure given the force specifications on the Instron instrument. The patterned aluminum was then ultrasonicated in ethanol for 10 minutes, rinsed with DI water, and dried by nitrogen gun before anodization.

### **2.3.5 Anodization of nanoimprinted aluminum substrates**

Aluminum was anodized in phosphoric acid under vigorous stirring. The concentrations of phosphoric acid were varied from 0.6 M to 3 M for 280-nm samples, from 0.2 to 0.6 M for 410-nm samples, from 0.04 to 0.2 M for 500-nm samples, from 4 to 15 mM for 645-nm samples, and from 1 to 5 mM for 760-nm samples (Table 2.3). To prevent sample burning, the electrolyte stock solution was diluted to the desirable final concentrations using a mixture of DI water and ethanol at a volume ratio of 4:1. The

electrolytic temperature was maintained at  $-7\text{ }^{\circ}\text{C}$  by situating in a Styrofoam box containing a mixture of isopropanol and tightly packed ice/dry ice. All samples were anodized for 1 hour using a DC power supply (Electronic Measurement Inc., TCR300T16). The anodization voltages ( $V_a$ ) were initially chosen corresponding to the relationship of cell size ( $D_c$  in nm) =  $V_a \times 2.5\text{ nm/V}$  [28], i.e. 112 and 164, 195, 255, and 296 V to form AAO films with indentation periods of 280, 410, 500, 645, and 760 nm respectively. However, for indentation periods of 500, 645, and 760 nm, anodization current surged when the calculated  $V_a$  of 200, 258 and 304 V were applied. Instead, voltages were lowered slightly to 195, 255 and 296 V respectively to maintain an anodization current density in the low milli-ampere/  $\text{cm}^2$  range.

Table 2.3: Anodization conditions

<i>Target AAO cell size (nm)</i>	<i>Applied voltage (volt)</i>	<i>H<sub>3</sub>PO<sub>4</sub> concentration (mol/dm<sup>3</sup>)</i>
280	112	0.6
		0.8
		1.0
		1.3
		1.7
		2.0
		2.5
		3.0*
410	164	0.20
		0.30
		0.40
		0.50
		0.60
		0.65*
500	195	0.04
		0.06
		0.08
		0.10
		0.13
		0.17
		0.20
		0.24*
645	255	0.004
		0.006
		0.008
		0.010
		0.012
		0.014
		0.015
		0.016*
760	294	0.001
		0.002
		0.003
		0.004
		0.005
		0.006*

\* indicates the critical concentrations corresponding to each applied voltage. Electrolyte temperature is maintained at -7 °C in all cases.

### **2.3.6 Sample Characterization**

Nanofeatures obtained in this work were characterized using a field-emission scanning electron microscope (FE-SEM – Hitachi 4300) and an atomic force microscope (AFM – Veeco di Dimension, D3100 V). The nanobeads, cell and pore sizes, and AAO film thickness were analyzed by ImageJ [29].

## **2.4: Results and Discussion**

### **2.4.1 Nanoimprinting of aluminum thin films**

The silica nanoparticles were synthesized in a range of 280 to 760 nm (Table 2.1). Using the convective deposition procedure developed by Gilchrist group [27], monolayers of silica nanoparticles deposited on glass substrates were obtained and are shown in Figure 2.2(A1)-(A5). Within the monolayer, the nanobeads take a hexagonal close-packed arrangement over a long range. Moreover a large area of deposition on the order of square centimeters can be created in ~15 minutes (Figure 2.1(B)). Such a process is scalable to accommodate flat substrates of any size and the mold is re-usable (Figure 2.3). These deposited nanoparticles serve as imprinting molds to indent aluminum deposited glass substrates. After imprinting on aluminum substrate, homogeneous nanodimples are formed on entire imprinted area while narrow bands of silica nanobead occasionally came off from the mold edge (Figure 2.4). The resulting nanodimples have a period matching the nanobead diameters (Figure 2.2(B1)-(B5)). Indentation depths are calculated from the diameters of the nanodimple opening in SEM images by trigonometry. The averages of dimple depth are  $73.45 \pm 5.08$  nm,  $68.80 \pm 5.56$  nm,  $56.78 \pm 3.52$  nm,  $42.97 \pm 6.42$  nm, and  $26.30 \pm 3.16$  nm for the 760-nm down to 280-nm samples, respectively. The depths of 760-nm and 500-nm samples are confirmed by AFM measurements (Figure 2.5), which are  $69.26 \pm 3.75$  nm and  $53.53 \pm 5.23$  nm respectively, comparable to the calculated values.



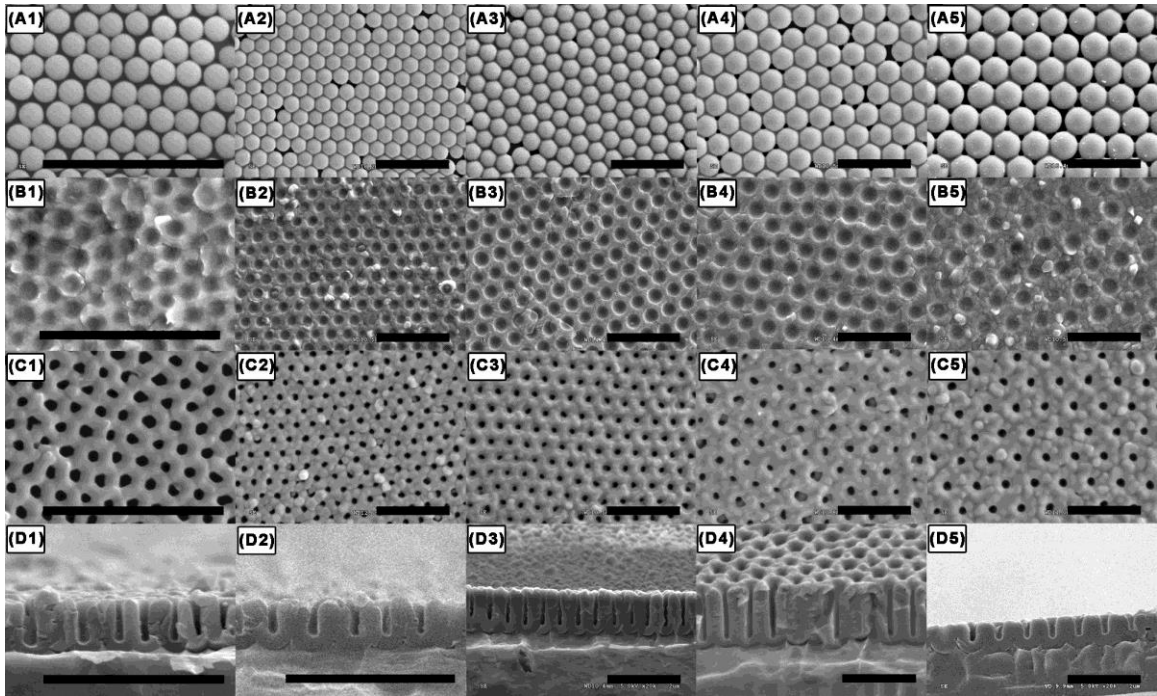


Figure 2.2: SEM images showing the nanoparticle monolayers used as the imprinting molds (row (A)), the indented aluminum thin films (row (B)), surfaces of the anodized oxide films (row (C)) and cross-section views of anodized oxide films (row (D)). The features were created using monolayers of 280 nm (column 1), 410 nm (column 2), 500 nm (column 3), 645 nm (column 4) and 760 nm (column 5) silica nanoparticles, respectively. The images show a translation of the nanofeature arrangements from the molds to the AAO films. All scale bars are 2  $\mu\text{m}$ .

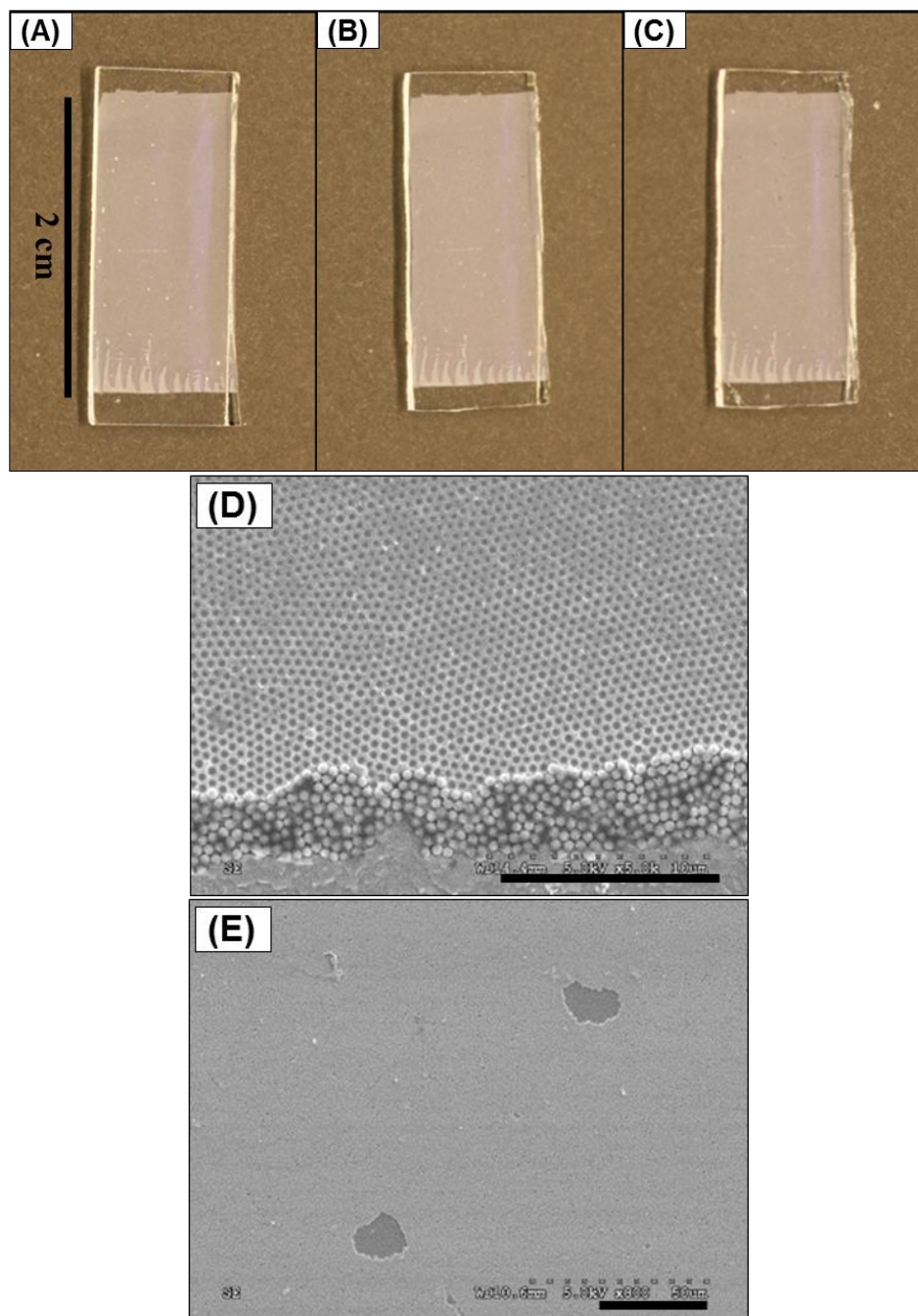


Figure 2.3: A 500-nm nanobead mold after being used (A) 0, (B) 5, and (C) 10 times. The mold is mostly intact after reuse except for thin stripes ( $< 10 \mu\text{m}$ ) silica beads lost from the mold edge. (D) An indented aluminum surface with nanobeads transferred from the mold edge. (E) Occasionally, small islands of nanobeads are lost inside the deposited monolayer after imprinting for 10 times. Scale bars are 2 cm in (A)-(C), 10  $\mu\text{m}$  in (D), and 30  $\mu\text{m}$  in (E).

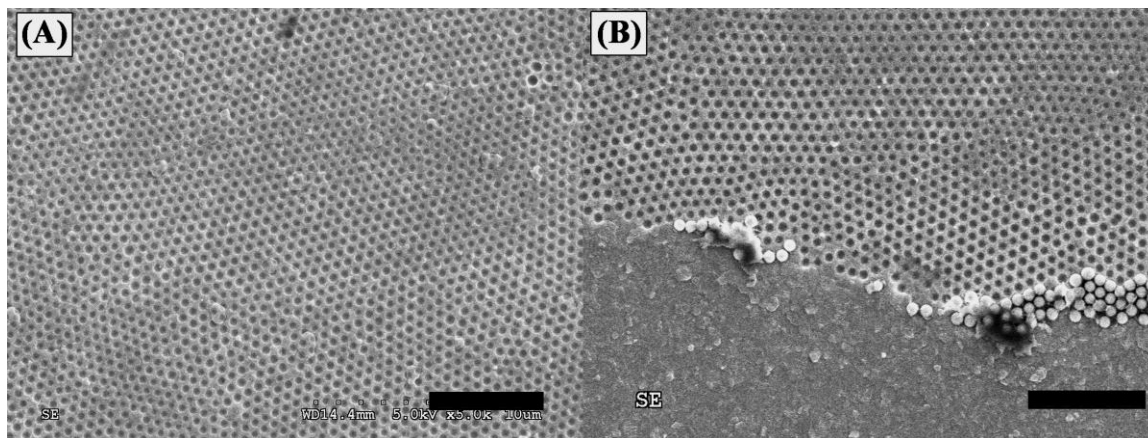


Figure 2.4: (A) An SEM image showing a large area of aluminum indented by 500-nm nanobead mold. (B) An SEM image showing an area of indentation boundary. The aluminum substrate can be indented over the whole surface to the mold boundary. Sometimes, a narrow band of silica beads is transferred from the mold edge to the aluminum surface after imprinting. All scale bars are 5  $\mu\text{m}$ .

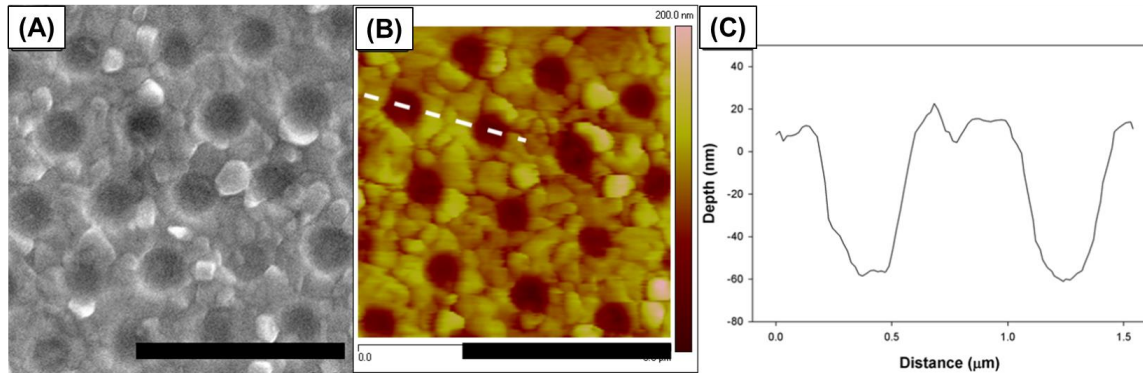


Figure 2.5: Topography of aluminum substrate indented by 760-nm beads measured by (A) SEM and (B) AFM. (C) The depth profile extracted from the dash line in (B). The indentation creates nanodimples with a depth of  $69.26 \pm 3.75$  nm by AFM measurement. Using bead size of 760 nm and nanodimple opening of  $448.69 \pm 13.93$  nm from SEM images, the depth of  $73.45 \pm 5.08$  nm can be calculated by trigonometry, which matches the results from AFM measurement. All scale bars are 2  $\mu\text{m}$ .

### **2.4.2 Anodization of nanoimprinted aluminum substrates**

Following the anodization process, the AAO porous structure forms a hexagonally packed cell array with the periods and arrangements consistent with those of the imprinting molds (Figure 2.2(C1)-(C5)). In contrast to the few discrete cell sizes available using non-patterned flat substrate [13], this pre-patterning procedure allows tunable cell sizes through selection of imprinting molds of different particle diameters.

The regular ordered cell arrangement is not limited to the top surface, but maintained through the film thickness (Figure 2.2(D1)-(D5)) as observed from the cross-sectional images. The varying film thickness in Figure 2.2(D) is a result of differences in electrolyte concentrations, which are discussed later in this paper. It should be noted here that although electrolyte concentration plays an important role in the film growth rate, it does not seem to impact the cell and pore geometry, which is different from pH-dependent cell arrangement in the self-ordering process [30].

Distinct from the self-organization process that takes hours of anodization to obtain hexagonally arranged pores, nanoindentation predefines the pore location and allows immediate formation of ordered pores [23, 24]. A comparison between anodization on patterned and un-patterned areas of the same sample is shown in Figure 2.1(H). It is clearly observed that ordered pores form only in the pre-indented region. Thus, the patterning technique is effective in greatly reducing the reaction time and aluminum thickness to produce straight pores. This is especially beneficial for the anodization of deposited thin aluminum films.

### 2.4.3 Effect of anodization voltage on cell size, pore size and porosity

When the cell sizes are inspected more carefully, it is found that the cell sizes range from 280 to 760 nm, matching the nanobead molds. The cell size increases linearly with the anodization voltage, governed through the relationship  $D_c \approx V_a \times 2.6 \text{ nm/V}$  (Figure 2.6). The proportionality is slightly off from previously reported value of 2.5 [28], due to the need to reduce voltage and avoid current surge when pre-patterned substrates with periods greater than 500 nm are used. The pore size ( $D_p$ ) of 88 to 211 nm also increases linearly with the voltage and the relationship is  $D_p \approx V_a \times 0.6 \text{ nm/volt}$ . As the voltage increases, the porosity is found to vary between 6% and 9% approximately. This value is slightly lower than what has been reported for the self-ordering regime of 10% porosity, dictated by an optimal stress induced from the volume expansion. Disordered pores often do not follow the 10% porosity rule [30]. We demonstrate here that regular, ordered pores guided by pre-indented patterns also deviate from the 10% rule. This is likely a result of residual stress in the aluminum layer from the imprinting process. Since the pores can be widened in a post-anodization process, the lower-than-10% porosity after anodization should not limit AAO in practical applications where high porosity is desired.

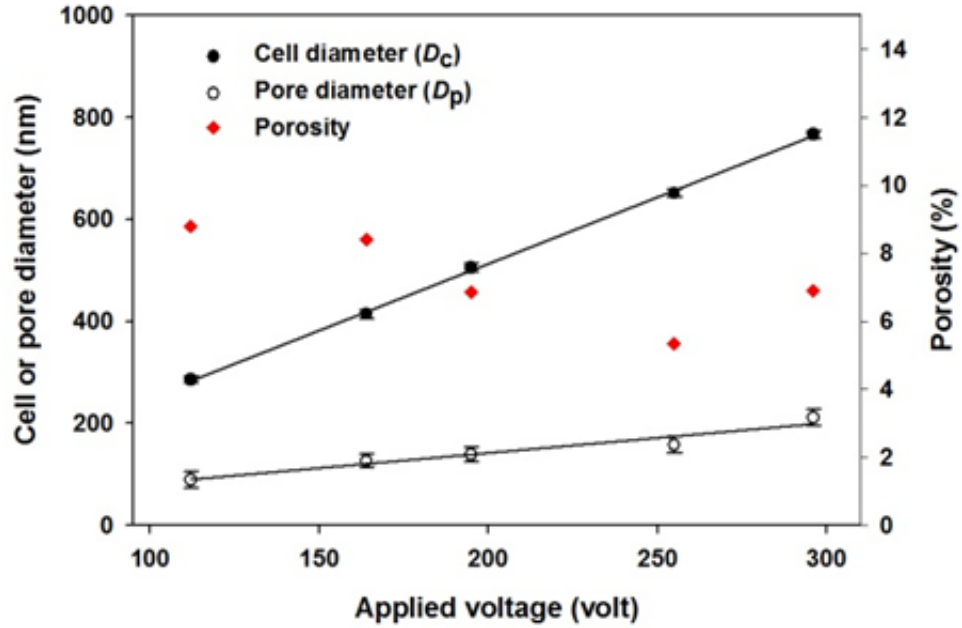


Figure 2.6: Relationship between the applied voltage ( $V_a$ , volt) and the resulting cell diameter ( $D_c$ , nm), pore diameters ( $D_p$ , nm), and porosity. The linear fit of the cell diameter versus voltage yields  $D_c = 2.6038 \times V_a - 8.3497$ . The pore diameter also increases linearly with the anodization voltage by  $D_p = 0.5997 \times V_a + 21.91$ . The porosity ( $P$ ) was calculated as  $P = (\pi/2\sqrt{3})(D_p/D_c)^2$ , which varies between 6% and 9% in the cell size range fabricated.

#### **2.4.4 Effect of H<sub>3</sub>PO<sub>4</sub> concentration on growth rate of AAO films**

Capability to continuously tune the cell size allows us to study the influence of electrolyte composition on the AAO formation at different voltages. To facilitate a comparison of electrolyte composition, we used phosphoric acid in all anodizations and varied only its concentration. While the cell and pore sizes are found to be independent of the acid concentration, the film growth rate varies greatly with acidity (Figure 2.7). The overall film thicknesses were measured directly from SEM images and the average AAO growth rates were calculated. With all the patterned AAO films, the film growth rate increases exponentially with the acid concentration until a critical value is reached, at which the anodization current density surges within 60 seconds and the film growth becomes non-uniform or breaks down. This critical concentration of phosphoric acid is found to rely on the anodization voltage. For anodization voltage of 164, 195, 255, and 296 V, the critical concentrations are 0.65, 0.24, 0.016, and 0.006 M, respectively (dash lines in Figure 2.7). When anodizing a pre-patterned substrate with a period of 280 nm at 112 V, the reaction is stable for an hour even when the phosphoric acid concentration is 3 M. Thus, no critical concentration is identified in this case. The maximum growth rate is found to be around 1-2  $\mu\text{m/hr}$  in all cases, slightly lower than that reported of self-ordered mild anodization around 2-6  $\mu\text{m/hr}$  [20]. The overall lower growth rate is likely a result of low anodizing temperature [31] of  $-7\text{ }^\circ\text{C}$  used to maintain a current density in the low  $\text{mA/cm}^2$  range.



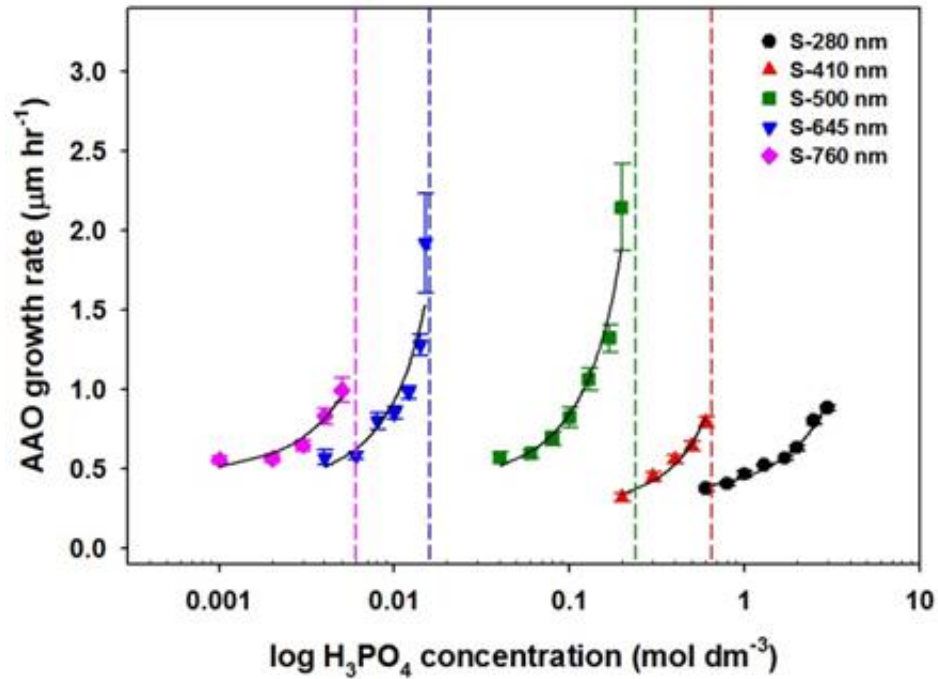


Figure 2.7: Relationship between the electrolytic concentration and film growth rate for different nanoindentation periods. For all the cell sizes, the film growth rate ( $GR$ , nm/hr) increases with the acid concentration ( $C$ , mol dm<sup>-3</sup>). The best fittings for each series show an exponential growth rate:  $GR = 311.3 \exp(0.3594 \cdot C)$  for inter pore distance of 280 nm;  $GR = 219.34 \exp(2.187 \cdot C)$  for inter pore distance of 410 nm;  $GR = 374.18 \exp(8.1051 \cdot C)$  for inter pore distance of 500 nm;  $GR = 341.38 \exp(100.11 \cdot C)$  for inter pore distance of 645 nm; and  $GR = 438.12 \exp(155.53 \cdot C)$  for inter pore distance of 760 nm. The dash lines indicate the critical concentrations leading to fast current surge within 60 seconds for each indentation period. Anodization of the 280 nm sample is stable even in the high concentration of phosphoric acid of 3 M.

The AAO growth involves movements of ionic species between electrolyte/ oxide and oxide/ metal interfaces under an electric field. The ion flux can be monitored by the current density in the anodization process (Figure 2.8(A)). Inspecting the current density as a function of time, it is observed that at the beginning of the anodization, there is a high current density, suggesting fast initial growth of AAO. The current density and growth rate then decrease over time until a steady state is reached due to the formation of AAO barrier at the bottom of the pores, which decreases the ion mobility. The steady state current density is found to be heavily dependent on the acid concentration under a fixed voltage. Taking 410 nm pre-indentation pattern anodized at 164 V as an example, the steady state current densities are 6.1, 8.3 and 11.2 mA/cm<sup>2</sup> for H<sub>3</sub>PO<sub>4</sub> concentrations of 0.2, 0.4, and 0.6 M, respectively. The corresponding average AAO film growth rates are 318, 556, and 792 nm (Figure 2.8(B)). The dependence of anodization current on the acid concentration thus offers a means to control the AAO growth rate.

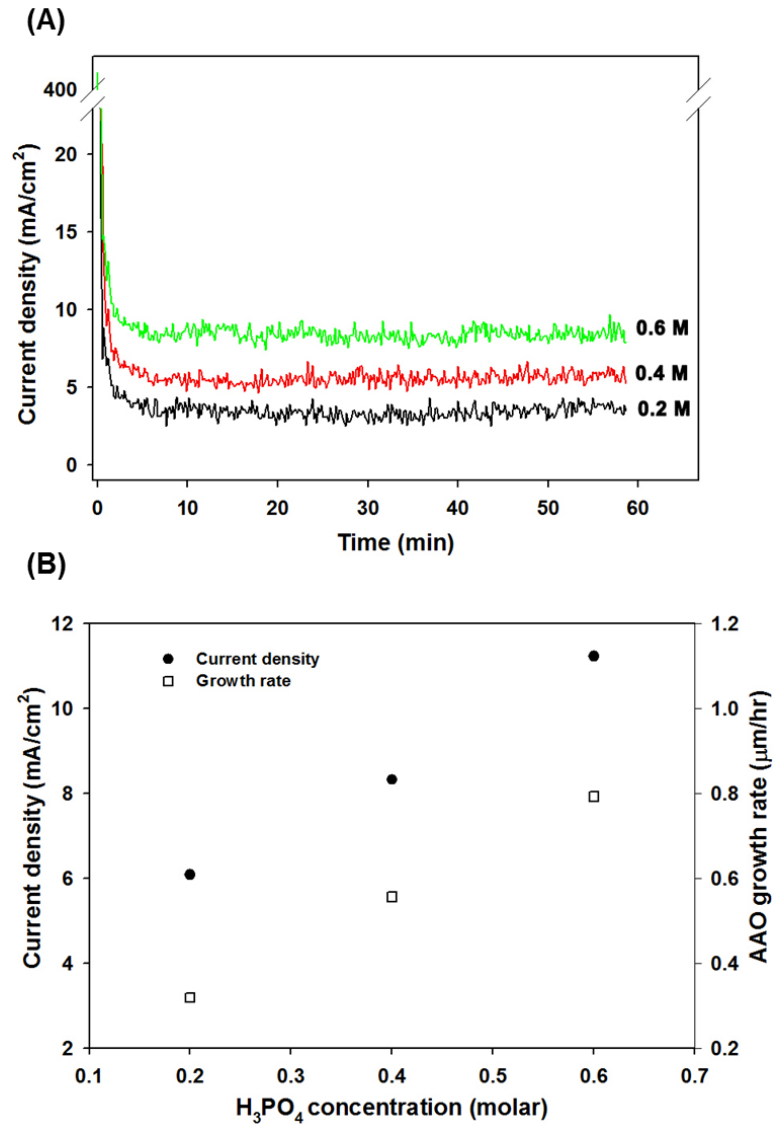


Figure 2.8: The profiles of current density of AAO film formed at 164 V in H<sub>3</sub>PO<sub>4</sub> concentrations of 0.2M, 0.4M, and 0.6M (A) Current profile as a function of time for 60 min. (B) Current density and AAO growth rate as a function of the H<sub>3</sub>PO<sub>4</sub> concentration.

The anodization current is related to the electrolyte concentration, electric field, and temperature according to the following equation:

$$i = 2anv \exp\left(-\left(\frac{W-qaE}{kT}\right)\right) \quad (\text{Eq. 2.1})$$

where  $n$  is the ion concentration,  $v$  is the jump frequency,  $a$  is the activation distance,  $W$  is the energy barrier and  $E$  is the interfacial electric field [32]. Although the applied voltage and temperature are critical parameters for an oxide formation, they are fixed for each AAO cell size. Thus, the only parameter that contributes significantly to the current density for a fixed cell size is the acid concentration. From a first inspection, it appears that the anodization current should scale linearly with the acid concentration. However, an increase of the acid concentration reduces the Debye length at the electrode surface and increases the local electrical field [33]. The exponential dependence of anodization current on the electrical field in Eq. 2.1 dictates the observed exponential relationship between the film growth rate and the acid concentration as seen in Figure 2.7.

When anodization is compared among different indentation patterns or applied voltages, it is observed that the acid concentration decreases exponentially with the increase of the anodization voltage for a fixed growth rate (Figure 2.9). This observation is consistent with Eq. 2.1: in the case that the current density (or growth rate) and temperature are constant, the ion concentration  $n$  is exponentially proportional to the electrical field, which linearly scales with the anodization voltage.

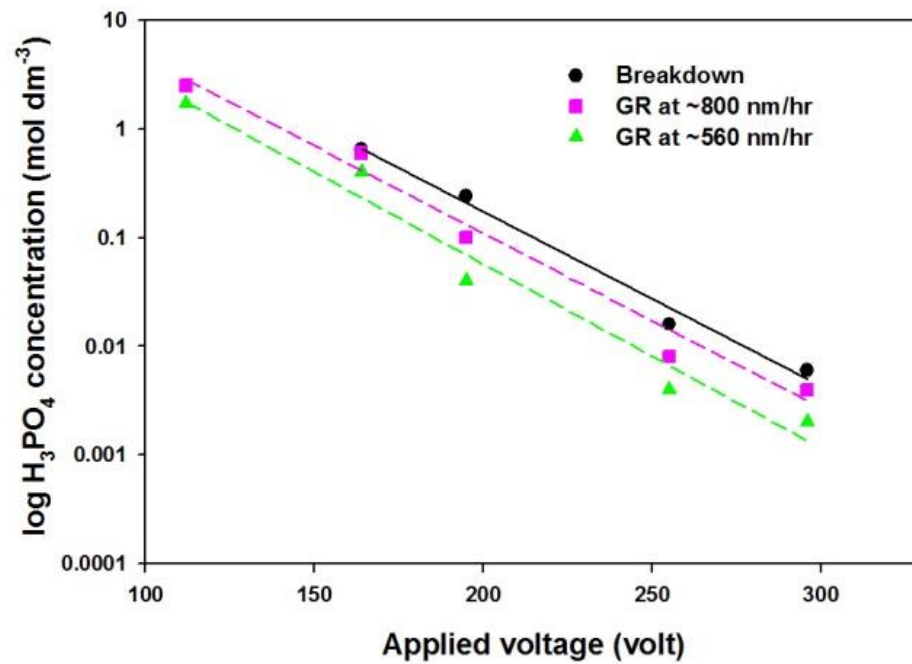


Figure 2.9:  $\text{H}_3\text{PO}_4$  concentration as a function of the applied voltage for different growth rates. The black solid line predicts the critical concentrations which yield a breakdown.

Although the AAO growth rate can be improved by increasing the acid concentration, it is still limited by a breakdown mechanism, where the current density surges rapidly and the oxide film grows non-uniformly (Figure 2.10). Such breakdown is caused by an avalanche electron multiplication process by impact ionization [34]. Albella *et al.* proposed a model that the breakdown voltage of anodic Ta<sub>2</sub>O<sub>5</sub> film is dependent on the logarithm of electrolyte concentration. The relationship is a result of increased avalanche size with electrolyte concentration. Figure 2.9 shows a similar dependence of electrolyte concentration and breakdown voltage for AAO formation and supports the model.

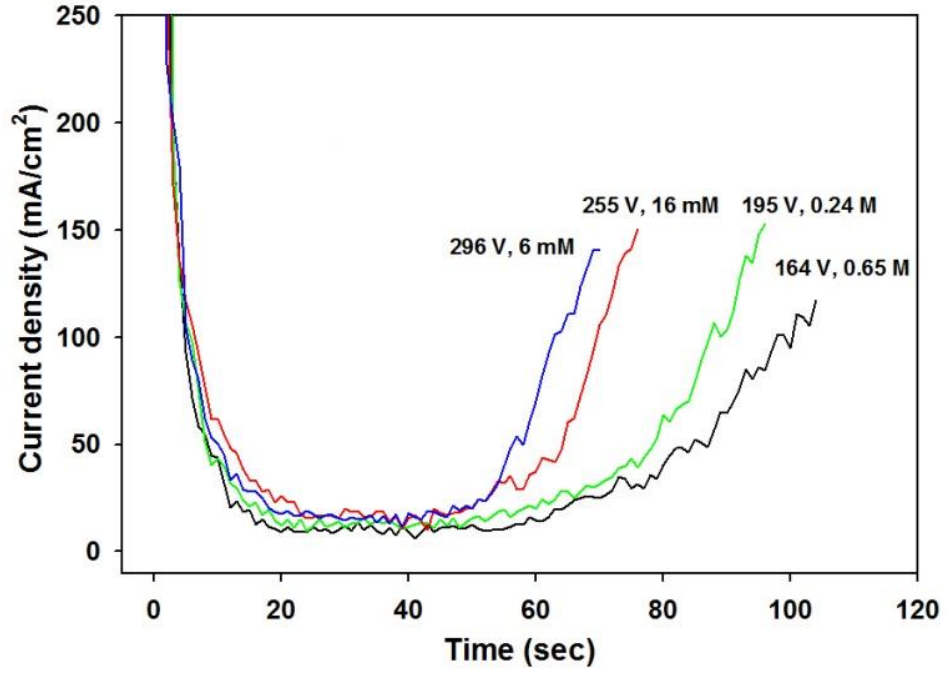


Figure 2.10: The profiles of breakdown current density at critical concentrations in different applied voltages.

As the cell size scales with the voltage, fabricating a nanoporous AAO film with a cell size larger than 500 nm has been found challenging due to breakdown. Although multiple techniques have been investigated to suppress burning, such as the usage of a powerful heat sink and conditioning the electrolyte with alcohol or polyethylene glycol [20, 35, 36], only a few studies reported successful fabrication of nanoporous AAO with cell size above 500 nm. Ono *et al.* [37] obtained AAO with cell sizes in the range of 300 to 600 nm using various acids, but the size of the ordered domains were small, only extending a few microns. Chu *et al.* fabricated AAO cell sizes as large as 950 and 980 nm by anodizing in malic acid at 450 V and in citric acid at 370 V, respectively, but the pore arrangement was not well ordered [38]. Fournier-Bidoz *et al.* [24] anodized pre-patterned aluminum in 0.3 M H<sub>3</sub>PO<sub>4</sub> to control the cell size in the range of 150-500 nm, but claimed anodization above 200 V to be unstable. Jagminas *et al.* [39] varied the phosphoric concentration from 0.005 to 0.3 M and tested the breakdown voltage using aluminum of different acid purities and found a convergence point of a breakdown voltage at 260 V corresponding to a cell size of approximately 650 nm, which was suggested as the cell size limit for anodization in phosphoric acid. Distinct from the prior work, we demonstrate here long-range ordered nanoporous AAO with cell sizes as large as 760 nm is possible by anodization in phosphoric acid. This is achieved by the combination of nanoimprinting and careful consideration of the anodization condition, including the voltage, acid concentration and temperature. The largest cell size of 760 nm obtained here is not the physical limit of the process but determined by the maximum output voltage in our power source.



## **2.5: Conclusions**

Imprinting an aluminum surface with silica nanobeads, along with carefully selecting anodization conditions such as voltages and concentrations of phosphoric acid, enables the fabrication of highly ordered nanoporous AAO film with a wide range of cell sizes using only a single step of anodization. In the procedure, the cell size is continuously tunable from 280 to 760 nm based on the imprinting molds and the anodization voltages. The film growth kinetics and reaction stability are controlled by the electrolyte concentration. More concentrated electrolyte solution yields a higher growth rate, although the acid concentration has to be kept below a critical level to avoid the breakdown phenomena. As the mold fabrication and imprinting process are easily controllable and scalable, large areas of AAO with a long range order and flexible cell size can be produced in a cost-effective fashion to enable the broader applications of AAO films.

## **2.6: References**

1. Hwang, S.K., et al., *Fabrication of Carbon Nanotube Emitters in an Anodic Aluminium Oxide Nanotemplate on a Si Wafer by Multi-Step Anodization*. *Nanotechnology*, 2005. 16(6): p. 850-858.
2. de la Escosura-Muniz, A. and A. Merkoci, *A nanochannel/nanoparticle-based filtering and sensing platform for direct detection of a cancer biomarker in blood*. *Small*, 2011. 7(5): p. 675-682.
3. Losic, D. and S. Simovic, *Self-Ordered Nanopore and Nanotube Platforms for Drug Delivery Applications*. *Expert Opinion on Drug Delivery*, 2009. 6(12): p. 1363-1381.
4. Shankar, K.S. and A.K. Raychaudhuri, *Growth of an Ordered Array of Oriented Manganite Nanowires in Alumina Templates*. *Nanotechnology*, 2004. 15(9): p. 1312-1316.
5. Mei, S.L., X.D. Feng, and Z.X. Jin, *Fabrication of Polymer Nanospheres Based on Rayleigh Instability in Capillary Channels*. *Macromolecules*, 2011. 44(6): p. 1615-1620.
6. Dan, Y.P., et al., *Dielectrophoretically Assembled Polymer Nanowires for Gas Sensing*. *Sensors and Actuators B-Chemical*, 2007. 125(1): p. 55-59.
7. Chen, G.F., et al., *Functional Template-Derived Poly(Methyl Methacrylate) Nanopillars for Solid-Phase Biological Reactions*. *Chemistry of Materials*, 2007. 19(16): p. 3855-3857.
8. Fan, Z.Y., et al., *Three-Dimensional Nanopillar-Array Photovoltaics on Low-Cost and Flexible Substrates*. *Nature Materials*, 2009. 8(8): p. 648-653.
9. Goh, C., K.M. Coakley, and M.D. McGehee, *Nanostructuring Titania by Embossing with Polymer Molds Made from Anodic Alumina Templates*. *Nano Letters*, 2005. 5(8): p. 1545-1549.
10. Masuda, H. and K. Fukuda, *Ordered Metal Nanohole Arrays Made by a 2-Step Replication of Honeycomb Structures of Anodic Alumina*. *Science*, 1995. 268(5216): p. 1466-1468.
11. Masuda, H., F. Hasegawa, and S. Ono, *Self-Ordering of Cell Arrangement of Anodic Porous Alumina Formed in Sulfuric Acid Solution*. *Journal of the Electrochemical Society*, 1997. 144(5): p. L127-L130.

12. Masuda, H., K. Yada, and A. Osaka, *Self-Ordering of Cell Configuration of Anodic Porous Alumina with Large-Size Pores in Phosphoric Acid Solution*. Japanese Journal of Applied Physics Part 2-Letters, 1998. 37(11A): p. L1340-L1342.
13. Lee, W., et al., *Fast Fabrication of Long-Range Ordered Porous Alumina Membranes by Hard Anodization*. Nature Materials, 2006. 5(9): p. 741-747.
14. Hill, J.J., K. Haller, and K.J. Ziegler, *Direct Fabrication of High-Aspect Ratio Anodic Aluminum Oxide with Continuous Pores on Conductive Glass*. Journal of the Electrochemical Society, 2011. 158(1): p. E1-E7.
15. O'Sullivan, J.P. and G.C. Wood, *The Morphology and Mechanism of Formation of Porous Anodic Films on Aluminium*. Proceedings of the Royal Society of London. Series A, Mathematical and Physical Sciences, 1970. 317(1531): p. 511-543.
16. Masuda, H., et al., *Highly Ordered Nanochannel-Array Architecture in Anodic Alumina*. Applied Physics Letters, 1997. 71(19): p. 2770-2772.
17. Mikulskas, I., et al., *Aluminum Oxide Photonic Crystals Grown by a New Hybrid Method*. Advanced Materials, 2001. 13(20): p. 1574-1577.
18. Liu, C.Y., A. Datta, and Y.L. Wang, *Ordered Anodic Alumina Nanochannels on Focused-Ion-Beam-Prepatterned Aluminum Surfaces*. Applied Physics Letters, 2001. 78(1): p. 120-122.
19. Chen, B., K. Lu, and Z.P. Tian, *Gradient and alternating diameter nanopore templates by focused ion beam guided anodization*. Electrochimica Acta, 2010. 56(1): p. 435-440.
20. Li, Y.B., et al., *Fabrication of Highly Ordered Nanoporous Alumina Films by Stable High-Field Anodization*. Nanotechnology, 2006. 17(20): p. 5101-5105.
21. Sun, Z.J. and H.K. Kim, *Growth of Ordered, Single-Domain, Alumina Nanopore Arrays with Holographically Patterned Aluminum Films*. Applied Physics Letters, 2002. 81(18): p. 3458-3460.
22. Kustandi, T.S., et al., *Wafer-Scale Near-Perfect Ordered Porous Alumina on Substrates by Step and Flash Imprint Lithography*. ACS Nano, 2010. 4(5): p. 2561-2568.
23. Matsui, Y., K. Nishio, and H. Masuda, *Highly ordered anodic porous alumina with 13-nm hole intervals using a 2D array of monodisperse nanoparticles as a template*. Small, 2006. 2(4): p. 522-525.

24. Fournier-Bidoz, S., et al., *Highly Ordered Nanosphere Imprinted Nanochannel Alumina (NINA)*. *Advanced Materials*, 2004. 16(23-24): p. 2193-2196.
25. Wang, W., et al., *Fabrication of Two- and Three-Dimensional Silica Nanocolloidal Particle Arrays*. *Journal of Physical Chemistry B*, 2003. 107(15): p. 3400-3404.
26. Jeong, S., et al., *Fast and Scalable Printing of Large Area Monolayer Nanoparticles for Nanotexturing Applications*. *Nano Letters*, 2010. 10(8): p. 2989-2994.
27. Kumnorkaew, P. and J.F. Gilchrist, *Effect of Nanoparticle Concentration on the Convective Deposition of Binary Suspensions*. *Langmuir*, 2009. 25(11): p. 6070-6075.
28. Keller, F., M.S. Hunter, and D.L. Robinson, *Structural Features of Oxide Coatings on Aluminum*. *Journal of the Electrochemical Society*, 1953. 100(9): p. 411-419.
29. *ImageJ*. Available from: <http://rsbweb.nih.gov/ij/index.html>.
30. Nielsch, K., et al., *Self-Ordering Regimes of Porous Alumina: The 10% Porosity Rule*. *Nano Letters*, 2002. 2(7): p. 677-680.
31. Li, F.Y., L. Zhang, and R.M. Metzger, *On the Growth of Highly Ordered Pores in Anodized Aluminum Oxide*. *Chemistry of Materials*, 1998. 10(9): p. 2470-2480.
32. Young, L., *Anodic Oxide Films*. 1961: Academic Press. 377.
33. Millet, P., *Electric Potential Distribution in an Electrochemical Cell*. *Journal of Chemical Education*, 1996. 73(10): p. 956-958.
34. Albella, J.M., I. Montero, and J.M. Martinezduart, *A Theory of Avalanche Breakdown during Anodic Oxidation*. *Electrochimica Acta*, 1987. 32(2): p. 255-258.
35. Zaraska, L., G.D. Sulka, and M. Jaskula, *The Effect of n-Alcohols on Porous Anodic Alumina Formed by Self-Organized Two-Step Anodizing of Aluminum in Phosphoric Acid*. *Surface & Coatings Technology*, 2010. 204(11): p. 1729-1737.
36. Chen, W., J.S. Wu, and X.H. Xia, *Porous Anodic Alumina with Continuously Manipulated Pore/Cell Size*. *ACS Nano*, 2008. 2(5): p. 959-965.
37. Ono, S., M. Saito, and H. Asoh, *Self-Ordering of Anodic Porous Alumina Formed in Organic Acid Electrolytes*. *Electrochimica Acta*, 2005. 51(5): p. 827-833.

38. Chu, S.Z., et al., *Large-scale fabrication of ordered nanoporous alumina films with arbitrary pore intervals by critical-potential anodization*. Journal of the Electrochemical Society, 2006. 153(9): p. B384-B391.
39. Jagminas, A., et al., *Growth Peculiarities of Aluminum Anodic Oxide at High Voltages in Diluted Phosphoric Acid*. Journal of Crystal Growth, 2001. 233(3): p. 591-598.

## Chapter 3

# Microfluidic Devices with Regular Macroporous Structures for HIV Viral Capture

### 3.1: Abstract

There is a need to develop inexpensive, portable and easy-to-use devices for viral sample processing for resource-limited settings. Here we offer a solution to efficient virus capture by incorporating macroporous materials with regular structures into microfluidic devices for affinity chromatography. Two-dimensional simulations were first conducted to investigate the effects of two structures, a nanopost array and a spherical pore network, on nanoparticle capture. Then, the two structures were created in polymers by templating anodic aluminum oxide films and 3D close-packed silica particles, respectively. When the microdevices containing functionalized porous materials were tested for human immunodeficiency virus (HIV) isolation, capture efficiencies of 80-99% were achieved under a continuous flow. Comparatively, functionalized flatbed microchannels captured around 10% of HIV particles. As the characteristic dimensions of the nanostructures are tunable, such devices can be adapted for the capture of different submicron bioparticles.

The high capture efficiency and easy-to-operate nature suit the need of resource-limited settings and may find applications for point-of-care diagnostics.

### **3.2: Introduction**

Effective separation and concentration of viruses or their biomarkers are essential steps in performing accurate and reliable viral load measurements for clinical diagnostics. However, current techniques such as ultracentrifugation [1], electrophoresis [2-4], chromatography [5-8], or magnetic beads based separation [9] require sophisticated equipment, skilled technicians and/or expensive reagents. These requirements inevitably limit accessibility of viral diagnostics in resource-limited regions.

To address the problem, lab-on-a-chip devices have been developed to process biofluids containing viruses or other nanoparticles. These devices can be integrated with micro-detectors for rapid and cost-effective analysis of biological samples at the point of need [10-12]. Employing an ultrafiltration process, several types of porous membranes have been encapsulated into microfluidic devices to physically capture whole particle viruses [13-15]. However, these approaches cannot distinguish target particles from non-target species of comparable sizes, which may interfere with downstream detection. On the other hand, affinity separation offers more biochemical specificity [16-18]. Chen *et al.* designed micro-mixers to promote the capture of human immunodeficiency virus (HIV) by antibody-functionalized magnetic beads in microchannels [19]. The capture efficiency is limited to 60%, likely due to the difficulty of predicting and optimizing the collision between target species and magnetic beads. Alternatively, porous matrices with regular structures and pore sizes comparable to the targets offer the opportunity to control the interaction between analyte and affinity groups [20]. Conventional chromatography matrices for viral and microvesicle separation [8, 21] such as agarose gels or packed



beads, have a broad pore size distribution [8, 21]. Nanostructured materials possessing characteristic dimension comparable to bionanoparticles, narrow pore size distribution and a regular pore structure are desirable for highly efficient viral isolation.

As a scalable and clean-room free approach, templating synthesis has been used to create various ordered nanostructures [22, 23]. In the form of macroporous matrices with interconnected pores on the submicron scale, two types of templated geometries have been reported. Yanigishita *et al.* utilized anodic aluminum oxide (AAO) porous membranes as a template to form ordered polymer nanopost arrays [24]. Chen *et al.* further embedded high aspect ratio nanopost arrays from AAO replication into microfluidic devices that function as bioreactors [25]. Gates *et al.* and Weldon *et al.* fabricated monolithic matrices with interconnected spherical pores by templating close-packed microbeads [26, 27]. In these porous materials, the pore geometries are regular and pore sizes are tunable within a wide range by selecting appropriate templates [26, 28]. These nanotemplated matrices have not yet been tested for viral separation.

Herein, we investigated two macroporous structures, a nanopost array and a spherical pore network, for viral capture in a microfluidic format. We first performed computational fluid dynamics simulations to understand how pore geometry influences the interaction between nanoparticles and porous matrices. Next, we created materials with regular macropores and integrated them into microfluidic devices. We then studied the capture efficiencies of HIV particles in the functionalized nanomaterials and compared them to capture efficiencies in flatbed devices.

### **3.3: Experimental details**

#### **3.3.1 Computational fluid dynamics simulation**

Creeping Flow Module and Particle Tracing for Fluid Flow Module were coupled in COMSOL Multiphysics to study the nanoparticle capture efficiency. The characteristic repeating units were used as the capture bed: a hexagonal array of circle islands was used to represent a 2D section of a nanopost array, and an array of interconnected circular voids represented a 2D section of a spherical pore structure. The shortest separation distance ( $D$ ) between the circular islands or of the pore neck was varied in the sub-micron range from 200 to 600 nm (targeting average HIV particle size of 110-164 nm) [29]. The hexagon diagonal and void diameter ( $W$ ) were varied accordingly to maintain a constant  $D/W$  ratio of 0.2. The particle density was  $1.05 \text{ g/cm}^3$  and the diffusion coefficient was set at  $5 \text{ }\mu\text{m}^2/\text{s}$ , corresponding to the values of HIV virions in plasma. An average inflow velocity of  $400 \text{ }\mu\text{m/s}$  was introduced along with 1000 particles per micron uniformly distributed at the inlet. Particle-particle interaction was neglected. Drag force and Brownian force were introduced using the COMSOL built-in formulation and centroids of the particles were tracked. The inlet was set  $1.5 \text{ }\mu\text{m}$  away from the capture zone to allow the particle convection to fully develop. The density and viscosity of fluid were  $1.00 \text{ g/cm}^3$  and  $1 \text{ mPa}\cdot\text{s}$ . For comparison, capture in a flat channel with a wall-to-wall separation of  $30 \text{ }\mu\text{m}$  and length of  $10 \text{ }\mu\text{m}$  was also simulated. All capture surfaces were specified to be 100% binding probability after particle-surface collision.

### **3.3.2 Materials**

SU-8 photoresist was purchased from MicroChem (Newton, MA). Sylgard 184 silicone elastomer kit was purchased from Dow Corning (Midland, MI). 99.997% aluminum foil, 85% aq. soln. phosphoric acid and 98% anhydrous copper (II) chloride were purchased from Alfa Aesar (Ward Hill, MA). Polymethyl methacrylate (PMMA) and polystyrene (PS) sheets were obtained from Plaskolite (Columbus, OH). A binary suspension containing 20 vol% of 1- $\mu\text{m}$  silica beads and 8 vol% of 100-nm PS beads in water was kindly provided by Professor Gilchrist at Lehigh University (Bethlehem, PA). Methyl methacrylate (MMA) monomer, EDC (N-(3-Dimethylaminopropyl)-N'-ethylcarbodiimide), NHS (N-hydroxysuccinimide sodium salt), and lyophilized bovine serum albumin (BSA) were purchased from Sigma Aldrich (St. Louis, MO). PMMA fine granules (M.W. 97000, M.N. 44700, Acros Organics) were purchased from Fisher Scientific (Pittsburgh, PA). Benzoin methyl ether was obtained from Electron Microscopy Sciences (Hatfield, PA). Phosphate buffered saline (PBS) was obtained from Mediatech (Herndon, VA). NeutrAvidin biotin-binding protein was purchased from Thermo Scientific (Rockford, IL). An HIV-1 p24 enzyme-linked immunosorbent assay (ELISA) kit was obtained from Perkin-Elmer (Waltham, MA). Polystyrene nanobeads 100 nm in diameter (internally dyed with Firefli<sup>TM</sup> Fluorescent Red (Ex 542/ Em 612 nm)) was obtained from Thermo Scientific (Fremont, CA).

### **3.3.3 Device fabrication**

Three types of microfluidic devices were fabricated: flatbed channels, porous channels with hexagonal post arrays and with spherical porous networks.

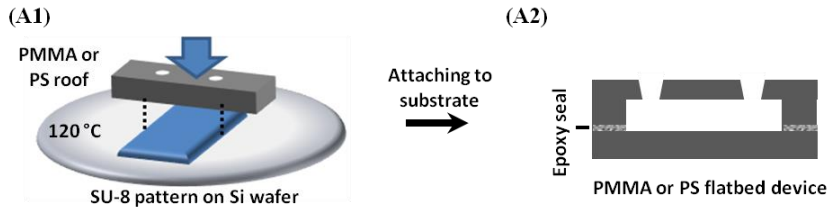
*Flatbed devices:* PMMA and PS flatbed devices were fabricated by an embossing process. First, SU-8 patterns of  $50 \text{ mm} \times 25 \text{ mm} \times 30 \text{ }\mu\text{m}$  were created on a silicon wafer by standard photolithography. Polymer sheets were cut into  $40 \times 8 \text{ mm}^2$  pieces and holes were drilled as the inlet and outlet. The polymer pieces were then manually pressed onto the SU-8 pattern at  $120 \text{ }^\circ\text{C}$  to form a 25 mm long indentation along the length of polymer piece. Next, the indented surface was glued to a flat sheet of the same material with epoxy and the sides were sealed. Finally, tubing was inserted into the inlet and outlet and fixed by epoxy. The channel dimension was  $25 \text{ mm} \times 8 \text{ mm} \times 30 \text{ }\mu\text{m}$  (Figure 3.1(A1-A2)).

*Microchannels with nanopost arrays:* The PMMA nanopost devices were fabricated by templating AAO films. First, aluminum foil was anodized at 195 V in 0.1M phosphoric acid mixed with ethanol at  $-7 \text{ }^\circ\text{C}$  via a two-step anodization [28]. After pore widening in 0.1M phosphoric acid for 1 hr at room temperature, the AAO sample was cut into  $25 \text{ mm} \times 10 \text{ mm}$  pieces. A pre-polymerization solution containing MMA monomer, 1% w/v PMMA granules, and 1% w/v benzoin methyl ether was then introduced into the AAO nanopores under vacuum for 15 min [25]. After drying, the monomer-treated side was attached to a flat PMMA substrate dampened by the pre-polymerization solution, and the assembly was exposed to ultraviolet light for 30 min. Next, the back aluminum was removed by a  $\text{CuCl}_2$  solution and the AAO pore barrier was opened by immersing the sample in 1.5M phosphoric acid for 5.5 hr. The newly exposed backside was then attached to another piece of PMMA flat sheet that had inlet and outlet holes drilled into it. The pre-polymerization solution was pipetted onto the contact surface and UV-

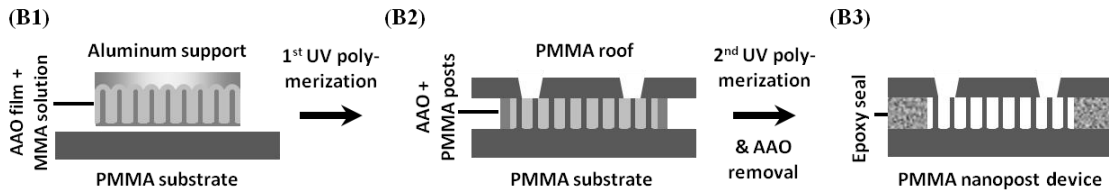
polymerized. Subsequently, the sides of the assembly were cut open to allow AAO film removal in 20 wt% NaOH for several days. After rinsed and immersed in de-ionized (DI) water overnight with gentle stirring, the device was lyophilized to ensure standing PMMA nanoposts [25]. Eventually the sides were sealed, and tubing was connected by epoxy glue. The footprint of the nanopost-covered region was  $25 \times 8 \text{ mm}^2$  and the nanoposts were  $\sim 25\text{-}30 \text{ }\mu\text{m}$  tall (Figure 3.1(B1-B3)).

*Microchannels with spherical pores:* The PS spherical pore devices were fabricated by templating close-packed silica beads. First, a polydimethyl siloxane (PDMS) open channel of  $25 \text{ mm} \times 8 \text{ mm} \times 30 \text{ }\mu\text{m}$  was fabricated using standard soft lithography. Then, 20  $\mu\text{L}$  of a binary suspension of  $1\text{-}\mu\text{m}$  silica and 100-nm PS in DI water was pipetted into the PDMS channel. The PDMS surface was pretreated by a plasma gun to promote spreading of the suspension throughout the open channel. After drying, the silica beads self-assembled into ordered structures with the PS beads filling the interstitial space. Next, the PS nanobeads were melted at  $240 \text{ }^\circ\text{C}$  for 10 min. The sample was glued to a PS flat sheet by epoxy glue and the PDMS mold was peeled off. Afterwards, silica beads were removed in 50% hydrofluoric acid and the device was rinsed in DI water. The porous matrix was attached to a flat piece of PS with drilled inlet and outlet by double-sided tape. Finally, the sides were sealed and the device was connected to tubing with epoxy glue. The porous region was  $25 \text{ mm} \times 8 \text{ mm} \times 30 \text{ }\mu\text{m}$  (Figure 3.1(C1-C3)).

### PMMA or PS flatbed device



### PMMA nanopost device



### PS spherical pore device

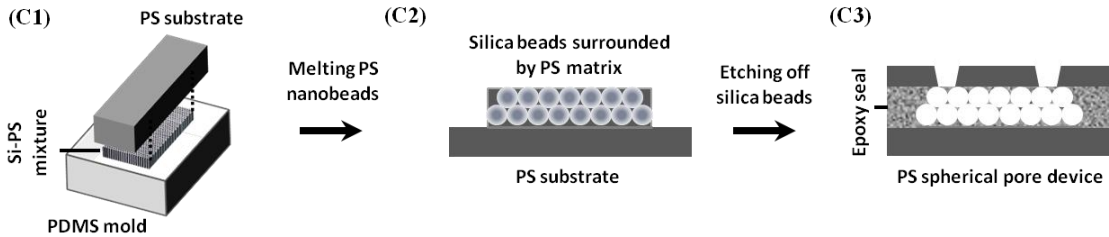


Figure 3.1: Schematics showing the fabrication processes of (A) PMMA and PS flatbed devices, (B) PMMA nanopost devices, and (C) PS spherical pore devices. (A1) A microchannel was formed on the substrate by manual embossing. (A2) The open channel was attached to a second flat sheet of the same material by epoxy glue, creating a flatbed microchannel. (B1) An array of PMMA nanoposts was fabricated through polymerizing MMA in an AAO template. (B2) The aluminum support was chemically removed and the newly opened top was attached to a PMMA roof by MMA and UV-polymerization. (B3) The PMMA nanopost device was created after chemically removing the AAO and sealing the sides. (C1) A binary suspension of silica and PS was deposited onto a PDMS mold. The PS beads were melted and glued to a PS substrate. (C2) The PDMS mold was detached and silica beads were etched away. (C3) A PS roof was attached to the PS porous structure and the sides were sealed, creating a PS spherical pore device.

### **3.3.4 Sample characterization**

The templates and macroporous structures were characterized by a field-emission scanning electron microscope (FE-SEM – Hitachi 4300) and the geometries were measured from the SEM images using ImageJ software.

### **3.3.5 Measurement of fluid permeability**

DI water was driven through the microfluidic devices at a constant pressure between 1 and 3 psi. The outflow was collected and weighed. The volume flow rate of water was then used to calculate the permeability of the devices.

### **3.3.6 Surface modification**

*PMMA devices:* All devices were washed with 70% isopropanol and DI water prior to surface functionalization. PMMA devices were hydrolyzed with 3 M sulfuric acid at 60 °C for 20 min and rinsed with DI water [30]. Then, the devices were exposed to the coupling reagents containing 1.6 mM EDC and 1 mM NHS in 50 mM MES buffer (pH 5.4) for 20 minutes at room temperature and rinsed with the MES buffer following the literature [31]. Afterwards, 20 µg/mL NeutrAvidin was injected into the devices and incubated for 2 hr before rinsing and viral capture.

*PS devices:* Polystyrene was functionalized by physisorption of NeutrAvidin for 2 hrs in PBS. To ensure comparable NeutrAvidin density on PS and PMMA substrates, PS flat substrates of 1×1 cm<sup>2</sup> were first physisorbed with NeutrAvidin at different concentrations of 0-20 µg/mL. To account for the difference in substrate materials, the concentration that yielded a comparable viral capture to that of PMMA was then selected to treat the porous PS devices. To evaluate binding specificity, 1% BSA/PBS was used in

the place of NeutrAvidin. After 2 hr incubation with NeutrAvidin or 1% BSA/PBS at room temperature, all devices were rinsed with 1% BSA/PBS before the viral capture test.

### **3.3.7 Viral production**

Pseudotyped HIV was cultured [32] and biotinylated [33] as previously reported. Briefly, HEK-293T cells were transfected with four plasmids of pGag-eGFP, pcRev, pR8ΔEnv, and pJR-FL in DMEM using MegaTran 1.0. After a 24-48 hr incubation period, the cells were washed with PBS and biotinylated with 1.67 mM Sulfo-NHS-LC-Biotin in PBS. The cells were incubated at room temperature for 30 min, then washed with PBS and 100 mM glycine to remove excess biotin, and re-incubated in HEK cell culture media. After incubation for another 24 hrs, the supernatant was filtered and centrifuged to concentrate the biotinylated HIV particles. The viral pellet was resuspended in the cell culture medium and stored at -80 °C.

### **3.3.8 Viral capture in microfluidic devices**

The biotinylated HIV at a concentration of  $\sim 10^6$  virions/mL was injected into the devices by a syringe pump at a constant flow rate of 5  $\mu\text{L}/\text{min}$  for a total volume of 320  $\mu\text{L}$ . Afterwards, all devices were washed with 90  $\mu\text{L}$  of PBS and 300  $\mu\text{L}$  of 0.5% Triton X-100, both at 5  $\mu\text{L}/\text{min}$ . The outflow during the viral injection, PBS wash, and Triton wash steps were collected separately. Then, a p24 ELISA kit was used to quantify the amount of p24 protein in the different outflow fractions. The input viral solutions were also analyzed to confirm mass balance between input and output solutions. Four devices were tested in each condition.



### **3.3.9 Capture of 100-nm fluorescent PS beads in microfluidic devices**

The suspension of 100-nm fluorescent PS beads (1 vol%) was utilized to visually observe non-specific binding in PMMA and PS porous devices. The devices were passivated with 1% BSA/PBS for 2 hr and the suspension containing 100-nm fluorescent nanobeads was then injected into the devices at 5  $\mu\text{L}/\text{min}$  for 1 hr, followed with 60  $\mu\text{L}$  PBS rinse at 5  $\mu\text{L}/\text{min}$ . Fluorescence images were taken afterwards along the flow direction in the center line at four different distances from the inlet. The fluorescence intensities were measured and the background intensity before injecting the particles was subtracted. Three devices of each geometry were tested. The images were processed by ImageJ software.

### **3.4: Results and Discussion**

#### **3.4.1 Computational analysis of nanoparticles captured in porous media**

We first investigated through COMSOL simulation how the capture bed geometry affects the probability of particle-matrix collision. Three types of geometries were evaluated: hexagonally arranged circular islands, interconnected circular voids, and two parallel plates, which represent the building blocks of the post array, spherical pore array, and flatbed channel. Two transport processes were considered, advection along the fluid streamlines and diffusion that crosses streamlines. The latter plays significant roles when the characteristic length of the capture bed is comparable to the nanoparticle dimension: the Péclet number ( $Pe$ ) is on the order of 1 when 100 nm particles are convected at 100  $\mu\text{m/s}$  in a matrix with a characteristic length of 100 nm. Figure 3.2(A)-(C) present distinct fluid streamlines in the three geometries. The nanostructures are seen to break the parallel input streamlines into branches and shorten the average diffusion distance for nanoparticles to interact with the affinity wall.

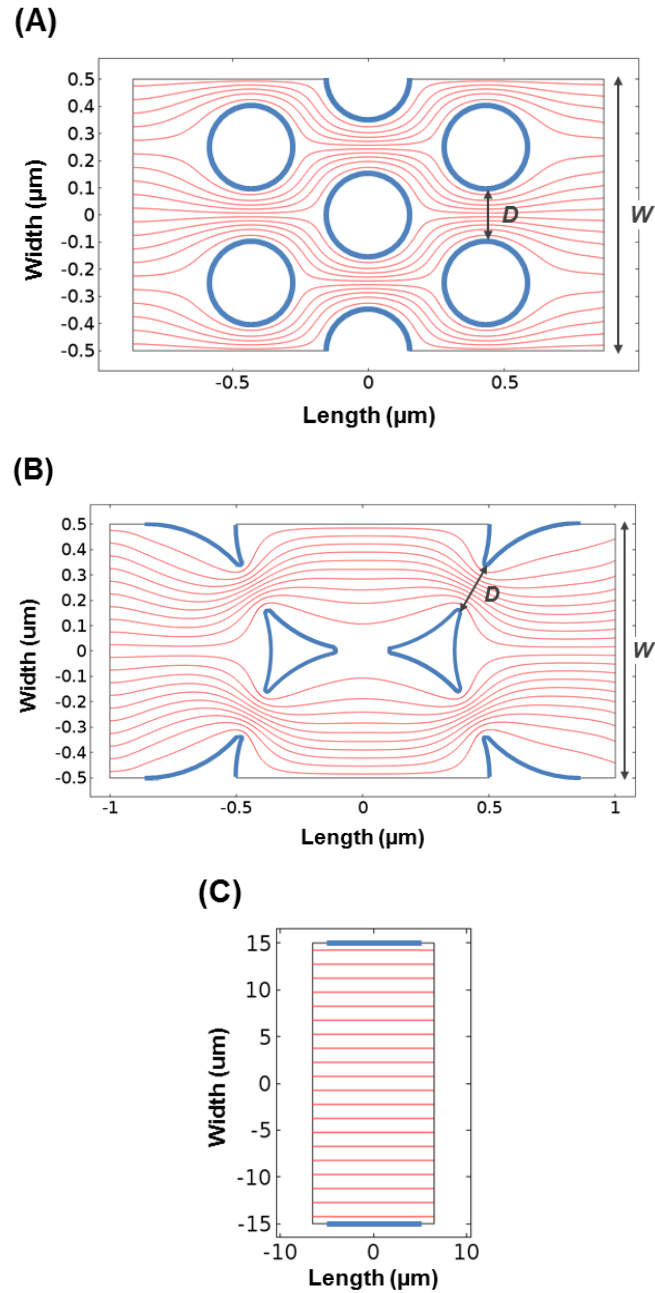


Figure 3.2: Simulation results of streamlines in (A) a hexagonal array of circle islands, (B) an interconnected void array and (C) two parallel plates. The bold boundaries represent the affinity capture surface.

By reducing the separation distance  $D$  of the circular islands or pore neck from 600 nm to 200 nm, the capture efficiency increases from 45.38% to 77.65% in the circular island array and 18.63% to 42.68% in the interconnected circular void array (Figure 3.3(A)). To account for a difference in the unit cell dimension, the capture efficiency is normalized to the footprint of the capture bed, and it increases from 4.32% per  $\mu\text{m}^2$  to 66.60% per  $\mu\text{m}^2$  in the circular island array and 1.19% per  $\mu\text{m}^2$  to 24.64% per  $\mu\text{m}^2$  in the interconnected circular void array (Figure 3.3(B)). This improvement of ~16-20 times with a 3 time reduction of gap distance is consistent with the analysis by Squires *et al.* that the footprint-normalized capture efficiency scales with  $D^{-8/3}$  for diffusion controlled reactions on a planar sensor under a constant convective feed [34].

When footprint-normalized capture efficiencies are compared between the two macroporous structures, the circular island array achieves ~2.7 to 3.6 times higher capture for each separation distance. This is partially contributed by a larger surface area in the circular island array per footprint. Given the same  $D$ , the capture area of the circular island array is ~2 times that of the interconnected void array per  $\mu\text{m}^2$ . Additional improvement beyond the surface area contribution (Figure 3.3(C)) is likely caused by the velocity and streamline profiles. The streamlines are more uniformly distributed in the circular island array, suggesting a relatively constant distance between each stream line and the capture surface. On the other hand, the distance between streamlines varies periodically in the circular void geometry, being closer at the pore neck and further apart at the circular void center. For a given separation distance,  $D$ , in the two geometries, the

average diffusion distance for nanoparticles to interact with the walls is longer in the circular void geometry, leading to lower capture efficiencies.

Although the streamlines in flatbed were seen to be uniform, the distance between particles and capture walls are rather far away. As a consequence, the capture efficiency of a flatbed channel was found to be 5.38% or 0.02% per  $\mu\text{m}^2$  footprint. The Péclet number in the flatbed device is on the order of 1000, so only particles close to the capture surface have the opportunity to collide. The computational analysis suggests that nanostructures promote affinity binding compared to a flatbed channel, due to an increase of the surface area and reduction of Péclet number. The performance of nanostructures improves with the size match between the matrix gap separation and the target species as well as uniformity of the streamline distribution.

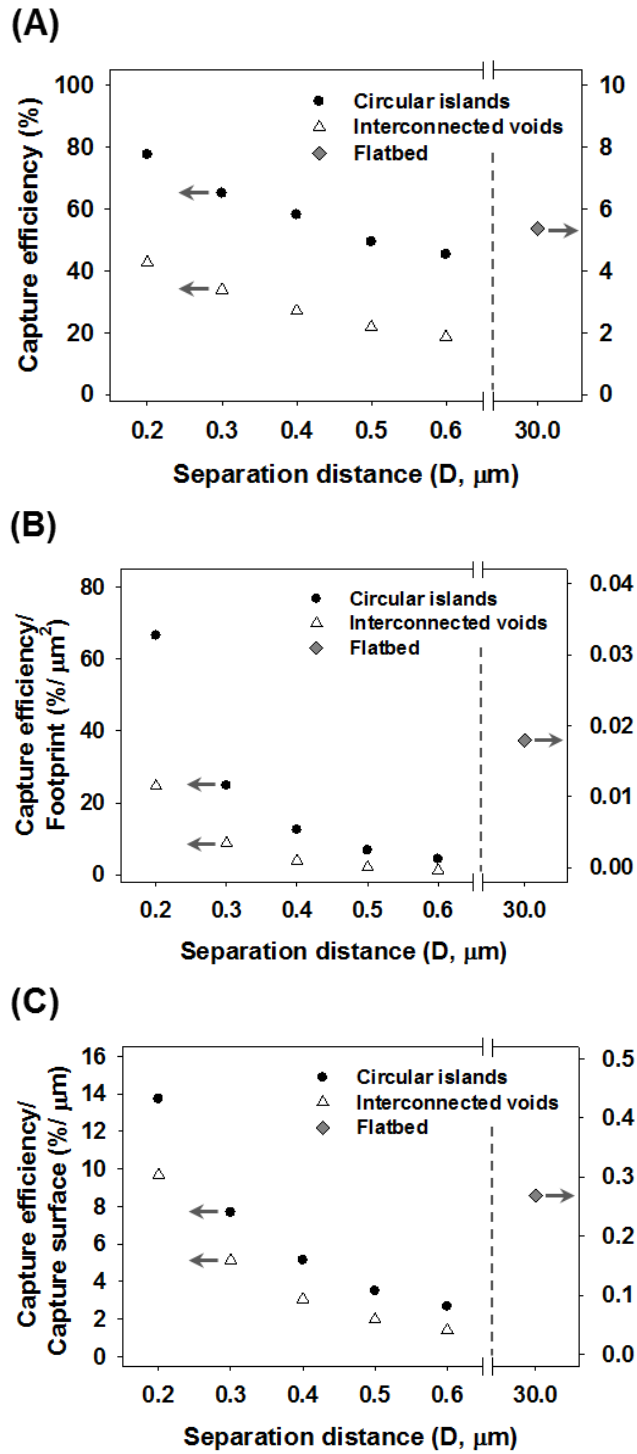


Figure 3.3: The effects of the separation distance,  $D$ , on the capture efficiency are shown in (A) total capture efficiency, (B) capture efficiency normalized to the capture bed footprint and (C) capture efficiency normalized to the capture surface area.

### 3.4.2 Fabrication of PMMA and PS macroporous devices

To test virus capture experimentally, two macroporous materials, a high aspect-ratio nanopost array and a spherical pore array, were fabricated by templating synthesis. Following the simulation predication to match the characteristic dimension of the matrices to the target species, the separation distance was selected to be ~200 nm, slightly larger than the HIV particles of 110 nm [32].

The PMMA nanopost arrays were fabricated by templating AAO films of straight pores. After two-step anodization in phosphoric acid, aluminum oxide self-orders into a hexagonally arranged pore array with a center-to-center distance of  $503.45 \pm 11.22$  nm (Figure 3.4(A)). By UV-polymerizing MMA in the AAO template and dissolving the aluminum substrate and oxide template, solid straight PMMA nanoposts with a high aspect ratio of ~80 were successfully fabricated as shown in Figure 3.4(B). The average space between the nanoposts is  $191.33 \pm 34.68$  nm. Assuming perfect replication of the AAO structure, the porosity of PMMA nanopost material is calculated to be 65.20% and the surface-to-volume ratio ( $R_{s/v}$ ) is  $4.46 \mu\text{m}^{-1}$  for a 30  $\mu\text{m}$  thick matrix, which is comparable to typical chromatographic media [35]. In contrast, a flatbed channel of the same height has the  $R_{s/v}$  of  $3.30 \times 10^{-4} \mu\text{m}^{-1}$ . Thus the  $R_{s/v}$  is enhanced by 4 orders of magnitude in the nanopost array.

The PS spherical pore matrix was fabricated by templating self-assembled, close-packed silica beads of  $990.50 \pm 12.58$  nm in diameter. The silica beads were co-deposited with 100-nm PS beads into a PDMS mold, and the PS was melted afterwards to form a matrix surrounding the silica beads (Figure 3.4(C)). After etching out the silica beads, a

network of PS spherical pores with small, interconnected openings was revealed (Figure 3.4(D)). The average size of the openings was  $232.55 \pm 21.73$  nm, similar to that reported by Gates *et al.* using 1  $\mu\text{m}$  microbeads as a template [26]. Assuming the silica beads form a close-packed structure and PS fills in the interstitial space perfectly, the theoretical  $R_{s/v}$  is  $3.73 \mu\text{m}^{-1}$  for a 30  $\mu\text{m}$  thick matrix. This  $R_{s/v}$  is slightly less than that of the PMMA nanopost array, but still  $\sim 4$  orders magnitude greater than a flatbed device of the same volume. The characteristics of the PMMA nanopost array and PS spherical pore network are summarized in Table 3.1.



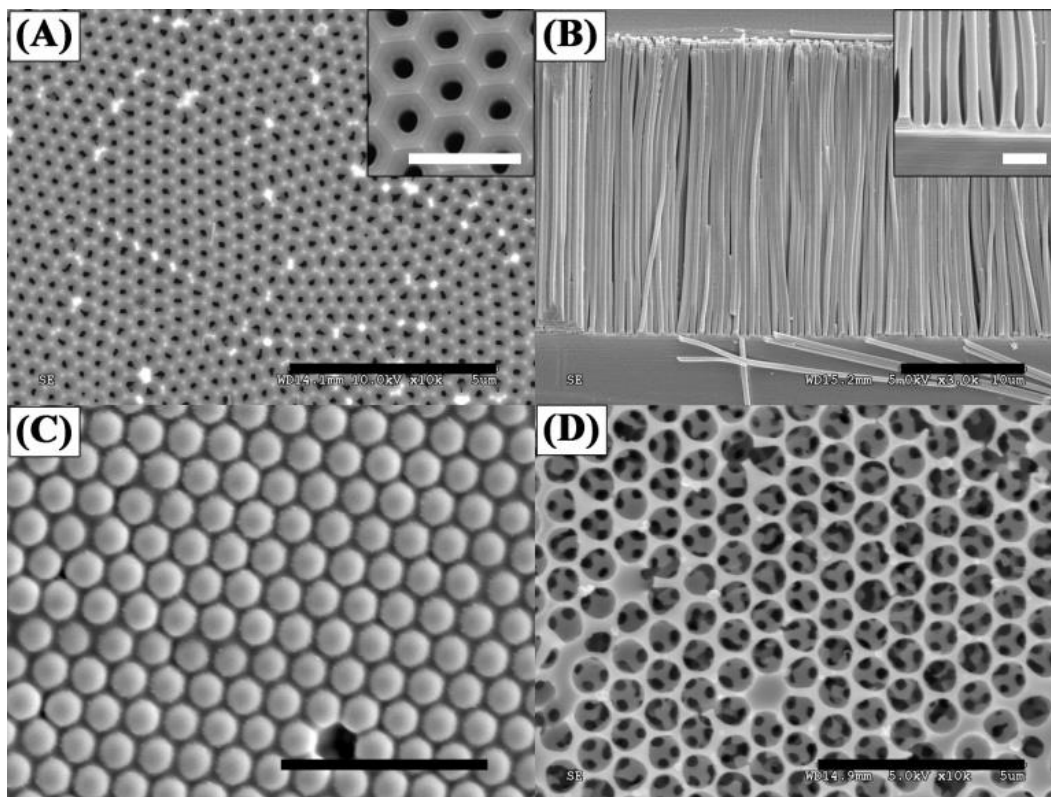


Figure 3.4: Representative SEM images of the templates and the replicated structures. (A) An AAO template with hexagonal arranged pores within each domain. The inset shows a zoom-in image of the AAO pore structure. (B) Standing PMMA nanoposts after templating AAO. The inset shows the separation of the nanoposts. (C) A template of 3D packed silica beads with PS filling the interstitial space. (D) A network of PS porous structure after silica bead removal. Scale bars in (A) - (D) are 5  $\mu\text{m}$  and scale bars in the insets are 1  $\mu\text{m}$ .

Table 3.1: Physical characteristics of the flatbed and macroporous channels fabricated in this work. All channels for the permeability tests have a dimension of 25 mm × 8 mm × 30 μm (Length × Width × Thickness).

<i>Device Structures</i>	<i>Separation Distance (nm)</i>	<i>Porosity*</i> (%)	<i>R<sub>s/v</sub>*</i> (μm <sup>-1</sup> )	<i>Permeability (m<sup>2</sup>)</i>
PMMA flat channel	30,000	100	3.30 × 10 <sup>-4</sup>	5.61×10 <sup>-11</sup> ± 2.87×10 <sup>-12</sup>
PS flat channel	30,000	100	3.30 × 10 <sup>-4</sup>	5.58×10 <sup>-11</sup> ± 2.05×10 <sup>-12</sup>
Hexagonal array of PMMA nanoposts	191.33 ± 34.68	65.14	4.46	1.97×10 <sup>-14</sup> ± 7.59×10 <sup>-16</sup>
Interconnected PS spherical pores	232.55 ± 21.73	74.17	3.73	1.43×10 <sup>-13</sup> ± 2.01×10 <sup>-14</sup>

\* indicates calculated values assuming a perfect replication of the template.

### 3.4.3 Permeability in microchannels with macroporous matrices

Water permeability in the macroporous matrices was measured according to Darcy's law of pressure driven flow:

$$Q = -\frac{\kappa A \Delta P}{\mu L} \quad (3.1)$$

where  $Q$  is the volume metric flow rate ( $\text{m}^3/\text{s}$ ),  $\kappa$  is the fluid permeability ( $\text{m}^2$ ),  $\mu$  is the dynamic viscosity of fluid ( $\text{Pa}\cdot\text{s}$ ),  $A$  ( $\text{m}^2$ ) and  $L$  (m) are the cross-sectional area and length of the channel, and  $\Delta P$  is the pressure drop across the channel (Pa).  $Q$  and  $\Delta P$  were measured experimentally to compute  $\kappa$ . PMMA and PS flatbed channels have comparable permeability of  $\sim 5.60 \times 10^{-11} \text{ m}^2$ , while the channel with PS spherical pores has a permeability of  $1.43 \times 10^{-13} \pm 2.01 \times 10^{-14} \text{ m}^2$ , which is an order magnitude higher than that of the PMMA nanopost channel of  $1.97 \times 10^{-14} \pm 7.59 \times 10^{-16} \text{ m}^2$  (Table 3.1). Various macroporous materials have been characterized in the literature for filtration applications, such as track-etched polycarbonate, polyethersulfone, and vertically aligned carbon nanotubes [11, 33, 36]. The permeabilities of these materials are in the range of  $10^{-15}$  to  $10^{-13} \text{ m}^2$ , into which our materials also fall. Although the spherical pore matrix has  $\sim 20\%$  less surface-to-volume ratio, the order-of-magnitude higher permeability may offer practical advantages considering low back pressure. In fact, a pressure of  $\sim 1 \text{ MPa}$  (145 psi) is required to drive water through the PMMA post array at  $\sim 10 \text{ }\mu\text{L}/\text{min}$ , and devices often leak at this pressure. Therefore, the viral capture experiments were carried out at a flow rate of  $5 \text{ }\mu\text{L}/\text{min}$ .

#### **3.4.4 Viral capture in microchannels with macroporous matrices**

After characterization of the physical properties, the two porous matrices were encapsulated into microfluidic devices and functionalized for viral capture. Since the two structures were fabricated with different materials, we first tested functionalization protocols to level the affinity chemistries on the two surfaces, so the contribution from the pore structures could be compared. PMMA flat substrates were immobilized with NeutrAvidin, while PS flat pieces of the same size were physisorbed with NeutrAvidin at concentrations of 0-20  $\mu\text{g/mL}$ . The functionalized substrates were used for viral capture under static incubation. As presented in Figure 3.5, the PS flat substrate exposed to 10  $\mu\text{g/mL}$  NeutrAvidin captures comparable amount of biotinylated HIV to that on the PMMA flat substrate. As a result, this concentration was used for surface modification of PS microchannels.

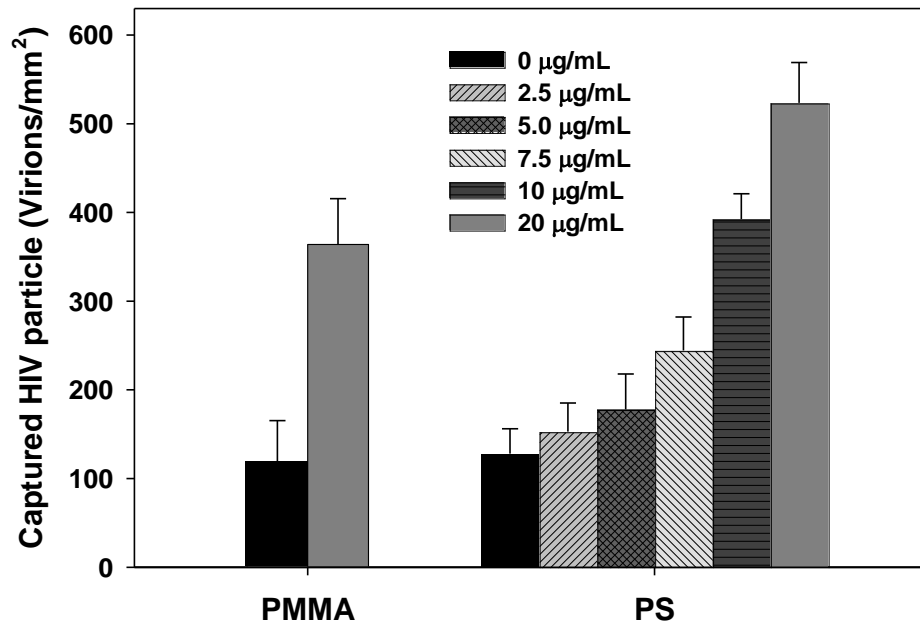


Figure 3.5: HIV virions captured on functionalized PMMA and PS flat substrates. The PMMA was functionalized with a fixed protocol but PS was exposed to different concentrations of NeutrAvidin from 0 to 20 µg/mL. PS treated with 10 µg/mL NeutrAvidin yielded a comparable amount of HIV viral capture to that on PMMA. The error bars represent standard deviation from 4 trials.

Capture of biotinylated HIV was performed in both the flatbed and porous microchannels under a constant flow of 5  $\mu\text{L}/\text{min}$ . The numbers of HIV particles in the flow-through, rinse, and lysis fractions were quantified and normalized to the total amount of viruses flowed into the device. Figure 3.6 shows the results of capture efficiency in each device. As predicted from the simulation, the flatbeds are not efficient in viral capture: the functionalized PMMA and PS flatbed channels each capture  $10.80 \pm 0.51\%$  and  $8.88 \pm 0.94\%$  virus from the input sample. In flatbed channels lacking NeutrAvidin, the capture efficiency dropped to  $1.62 \pm 0.23\%$  and  $1.08 \pm 0.25\%$  respectively, suggesting surface functionalization is effective.

The regular macroporous structures significantly improve the capture efficiency. NeutrAvidin treated PMMA nanopost and PS spherical pore arrays each captured  $99.46 \pm 0.51\%$  and  $80.10 \pm 0.92\%$  of virus from the input sample. A longer device containing PS spherical pore network is expected to capture more viral particles, while the flow resistance and back pressure will also increase proportionally. The current dimension is selected to balance the capture yield and back pressure in the nanopost devices, and the same dimension is used to create the spherical pore devices and facilitate comparison. Noticeably, non-specific binding in the nanopost array was found high: the PMMA nanopost devices without NeutrAvidin captured  $88.03 \pm 2.61\%$  HIV versus  $12.00 \pm 4.27\%$  in PS spherical pore matrices without NeutrAvidin (Figure 3.6). In contrast to a low nonspecific binding in flatbed devices, the macroporous devices demonstrate greater nonspecific capture yields, especially in PMMA nanopost devices.

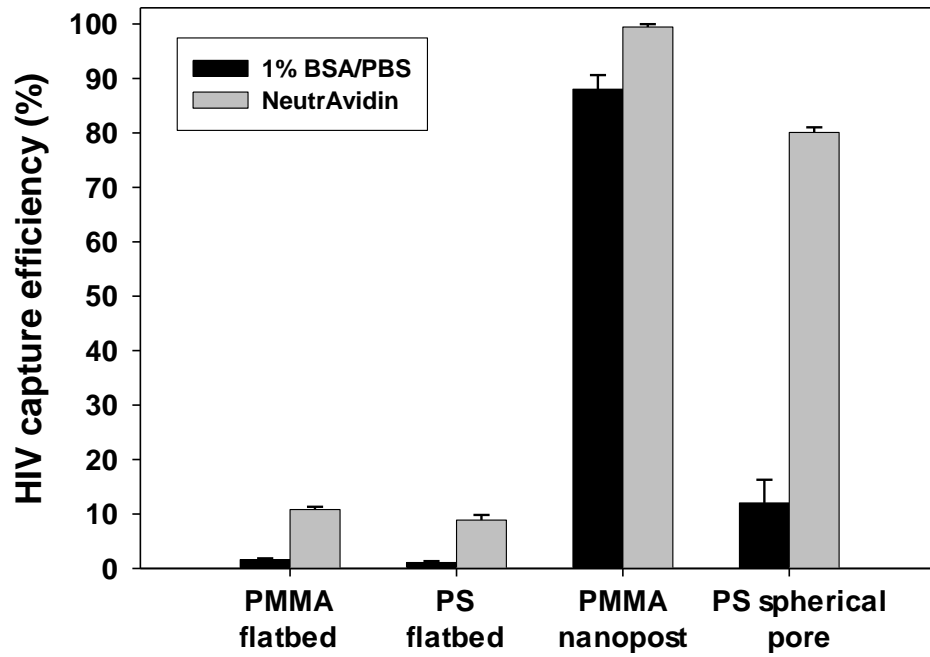


Figure 3.6. HIV capture efficiency in the flatbed and macroporous devices with surface treatment by 1% BSA/PBS or NeutrAvidin. The error bars represent standard deviation from 4 trials.

Significant non-specific binding in the nanopost array is likely a result of structural defects, which form narrower spacing than the diameter of HIV particles and physically trap them. Despite all the precautions to preserve standing nanoposts, such as lyophilization and attaching both ends of the nanoposts to solid supports, deformation and collapse of high aspect ratio nanoposts remain unavoidable. According to the theoretical calculation by Hui *et al.* [37], PMMA nanoposts would experience lateral collapse when the aspect ratio reaches  $\sim 12$  as a result of capillary and surface adhesive forces, while the high aspect ratio of 80 used in our work exceeds the critical value. To visualize physical trapping in the macroporous matrices, bare PS fluorescent nanobeads of 100 nm in diameter were flowed into the PMMA and PS porous devices. After rinsing, fluorescent images were acquired as shown in Figure 3.7(A)-(B). In the PMMA device, bright fluorescent domains were observed, suggesting formation of nanopost clusters that physically retain the beads. The average width of the clusters is  $53.54 \pm 11.70 \mu\text{m}$ , consistent with bundling of high aspect ratio nanoposts reported in the literature [25, 38]. When the fluorescence intensity was quantitatively analyzed along the flow direction (Figure 3.7(C)), non-specific binding was observed from the inlet to the outlet in the nanopost devices. The larger error bars are consistent with clustering of the fluorescence intensity. On the other hand, fluorescence intensities remain rather uniform and low in the PS spherical pore devices, suggesting minimal structural collapse and a low level of non-specific binding.



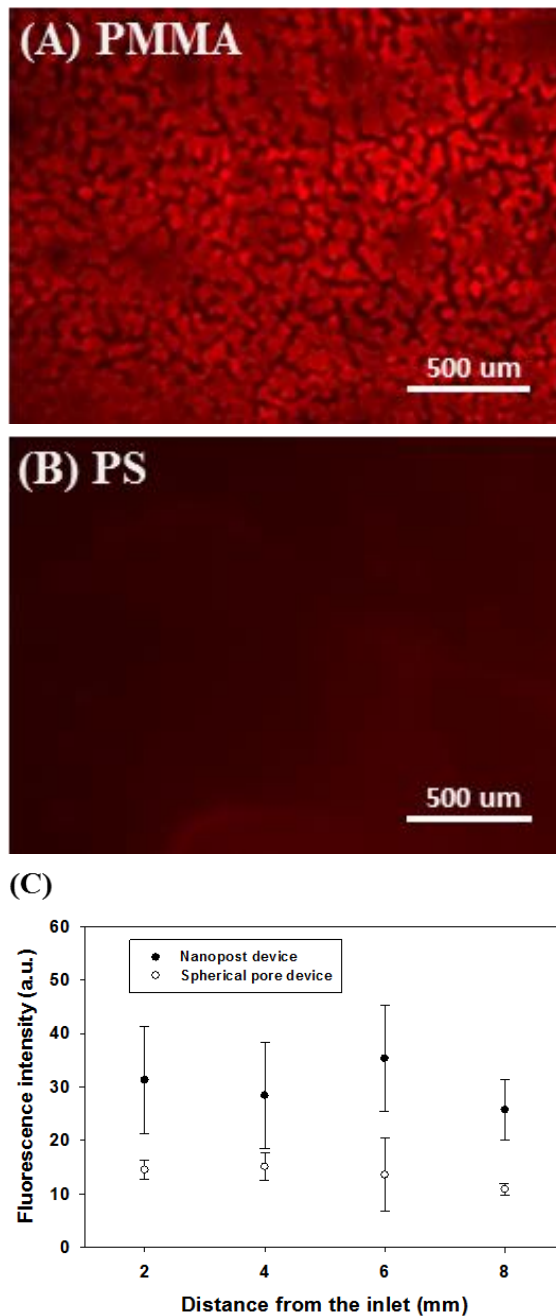


Figure 3.7: Physical retention of 100-nm fluorescent PS nanobeads in (A) a PMMA nanopost device and (B) a PS spherical pore device after rinsing. (C) Fluorescence intensity distribution along the channel length reveals greater non-specific binding of the fluorescent beads in the nanopost device. The error bars represent standard deviation from 3 trials.

Our work demonstrates that macroporous materials with regular structures can be incorporated into microfluidic devices for highly efficient viral separation. Despite a wide use of macroporous materials as size-exclusion media to decontaminate viruses from biopharmaceutical products [39], conventional matrices tend to have a broad size distribution, which makes it difficult to predict the target-matrix interactions. Our devices, which contain regular macroporous structures, facilitate theoretical understanding and practical optimization of the target-matrix collision. The affinity chemistry promotes specific capture of the target particles, especially in the spherical pore devices. Due to its small volume, the miniaturized device also concentrates target analyte by orders of magnitude. Furthermore, sample processing can be achieved in a simple flow-through process. Thus the device could be used for viral purification and enrichment in resource-limited settings. As a proof of principle, biotinylated HIV virus and NeutrAvidin are used in this work, while the surface can be modified by broad neutralizing antibodies [40], aptamers [41, 42], and other affinity molecules [17] for the isolation of wild type viruses. With recent biosensing applications in porous matrices [16, 18, 20], it is also plausible to incorporate electrical and optical sensors into our device to detect captured bio-nanoparticles.

Anticipating other applications may demand macroporous structures of dimensions different from those in this work, the fabrication strategies presented here offer great geometrical flexibility. In terms of AAO templating, the pore size, porosity and interpore distance of AAO mold can all be independently adjusted in submicron range [28]. Similarly, for the spherical pore structure, pore size and pore opening are

controllable by the composition of the colloid suspension [26, 27]. The tunable sizes of these macroporous structures make them versatile tools for processing nanoparticles and biomolecules of different sizes and shapes.

### **3.5: Conclusions**

Two different macroporous structures, a nanopost array and a spherical nanopore array, are studied in this work as affinity matrices for viral isolation. Computational analyses and experiments demonstrate significantly enhanced capture efficiency in the porous devices over flatbed channels, and the enhancement is attributed to large surface-to-volume ratios and short diffusion distance before interaction. While the nanopost arrays are shown to have higher capture efficiency than the spherical pore devices, structural defects associated with the high aspect ratio posts also generate higher non-specific binding. Since macroporous structures of different characteristic dimensions can be formed by adjusting the template geometry, the templating approach to incorporate nanomaterials into microfluidic devices is potentially applicable for separation and concentration of a broad spectrum of bio-nanoparticles and biomolecules.

### **3.6: References**

1. Ehrnst, A., et al., *Efficient isolation of HIV from plasma during different stages of HIV infection*. Journal of Medical Virology, 1988. **26**(1): p. 23-32.
2. Welker, R., et al., *Biochemical and structural analysis of isolated mature cores of human immunodeficiency virus type 1*. Journal of Virology, 2000. **74**(3): p. 1168-1177.
3. Mironov, G.G., et al., *Viral quantitative capillary electrophoresis for counting intact viruses*. Analytical Chemistry, 2011. **83**(13): p. 5431-5435.
4. Kremser, L., D. Blaas, and E. Kenndler, *Capillary electrophoresis of biological particles: Viruses, bacteria, and eukaryotic cells*. Electrophoresis, 2004. **25**(14): p. 2282-2291.
5. Richieri, S.P., et al., *Characterization of highly purified, inactivated HIV-1 particles isolated by anion exchange chromatography*. Vaccine, 1998. **16**(2-3): p. 119-129.
6. Ehrlich, L.S., B.E. Agresta, and C.A. Carter, *Assembly of recombinant human-immunodeficiency-virus type-1 capsid protein in vitro*. Journal of Virology, 1992. **66**(8): p. 4874-4883.
7. Burden, C.S., et al., *A monolith purification process for virus-like particles from yeast homogenate*. Journal of Chromatography B-Analytical Technologies in the Biomedical and Life Sciences, 2012. **880**: p. 82-89.
8. Kalbfuss, B., et al., *Purification of cell culture-derived human influenza a virus by size-exclusion and anion-exchange chromatography*. Biotechnology and Bioengineering, 2007. **96**(5): p. 932-944.
9. Lopez, C.A., et al., *Characterization of HIV-1 RNA forms in the plasma of patients undergoing successful HAART*. Archives of Virology, 2010. **155**(6): p. 895-903.
10. Sia, S.K., et al., *An integrated approach to a portable and low-cost immunoassay for resource-poor settings*. Angew. Chem. Int. Ed. Engl., 2004. **43**(4): p. 498-502.
11. Lee, W.G., et al., *Nano/Microfluidics for diagnosis of infectious diseases in developing countries*. Advanced Drug Delivery Reviews, 2010. **62**(4-5): p. 449-457.
12. Workman, S., et al., *Rapid detection of HIV-1 p24 antigen using magnetic immuno-chromatography (MICT)*. Journal of Virological Methods, 2009. **160**(1-2): p. 14-21.

13. Wang, S.Q., et al., *Simple filter microchip for rapid separation of plasma and viruses from whole blood*. International Journal of Nanomedicine, 2012. **7**: p. 5019-5028.
14. Liu, C.C., et al., *Membrane-based, sedimentation-assisted plasma separator for point-of-care applications*. Analytical Chemistry, 2013. **85**(21): p. 10463-10470.
15. Sia, S.K. and G.M. Whitesides, *Microfluidic devices fabricated in poly(dimethylsiloxane) for biological studies*. Electrophoresis, 2003. **24**(21): p. 3563-3576.
16. de la Escosura-Muniz, A. and A. Merkoci, *A nanochannel/nanoparticle-based filtering and sensing platform for direct detection of a cancer biomarker in blood*. Small, 2011. **7**(5): p. 675-682.
17. Wang, S.Q., et al., *Efficient on-chip isolation of HIV subtypes*. Lab on a Chip, 2012. **12**(8): p. 1508-1515.
18. Letant, S.E., et al., *Functionalized silicon membranes for selective bio-organism capture*. Nat. Mater., 2003. **2**(6): p. 391-396.
19. Chen, G.D., et al., *Concentration and purification of human immunodeficiency virus type 1 virions by microfluidic separation of superparamagnetic nanoparticles*. Analytical Chemistry, 2010. **82**(2): p. 723-728.
20. Chen, G.D., et al., *Nanoporous elements in microfluidics for multiscale manipulation of bioparticles*. Small, 2011. **7**(8): p. 1061-1067.
21. Taylor, D.D., W. Zacharias, and C. Gercel-Taylor, *Exosome isolation for proteomic analyses and RNA profiling*. Methods Mol. Biol., 2011. **728**: p. 235-246.
22. Jani, A.M.M., D. Losic, and N.H. Voelcker, *Nanoporous anodic aluminium oxide: Advances in surface engineering and emerging applications*. Progress in Materials Science, 2013. **58**(5): p. 636-704.
23. Velev, O.D. and A.M. Lenhoff, *Colloidal crystals as templates for porous materials*. Current Opinion in Colloid & Interface Science, 2000. **5**(1-2): p. 56-63.
24. Yanagishita, T., K. Nishio, and H. Masuda, *Fabrication of metal nanohole arrays with high aspect ratios using two-step replication of anodic porous alumina*. Adv. Mater., 2005. **17**(18): p. 2241-2243.

25. Chen, G., et al., *Integration of large-area polymer nanopillar arrays into microfluidic devices using in situ polymerization cast molding*. Lab on a Chip, 2007. **7**(11): p. 1424-1427.
26. Gates, B., Y.D. Yin, and Y.N. Xia, *Fabrication and characterization of porous membranes with highly ordered three-dimensional periodic structures*. Chemistry of Materials, 1999. **11**(10): p. 2827-2836.
27. Weldon, A.L., et al., *Fabrication of macroporous polymeric membranes through binary convective deposition*. ACS Appl. Mater. Interfaces, 2012. **4**(9): p. 4532-4540.
28. Surawathanawises, K. and X. Cheng, *Nanoporous anodic aluminum oxide with a long-range order and tunable cell sizes by phosphoric acid anodization on pre-patterned substrates*. Electrochim. Acta, 2014. **117**: p. 498-503.
29. Gentile, M., et al., *Determination of the size of HIV using adenovirus type-2 as an internal length marker*. Journal of Virological Methods, 1994. **48**(1): p. 43-52.
30. Brown, L., et al., *Fabrication and characterization of poly(methylmethacrylate) microfluidic devices bonded using surface modifications and solvents*. Lab on a Chip, 2006. **6**(1): p. 66-73.
31. Miao, J.J., et al., *Adsorption of doxorubicin on poly(methyl methacrylate)-chitosan-heparin-coated activated carbon beads*. Langmuir, 2012. **28**(9): p. 4396-4403.
32. Hu, Y., X.H. Cheng, and H.D. Ou-Yang, *Enumerating virus-like particles in an optically concentrated suspension by fluorescence correlation spectroscopy*. Biomedical Optics Express, 2013. **4**(9): p. 1646-1653.
33. Chan, L., et al., *Conjugation of lentivirus to paramagnetic particles via nonviral proteins allows efficient concentration and infection of primary acute myeloid leukemia cells*. Journal of Virology, 2005. **79**(20): p. 13190-13194.
34. Squires, T.M., R.J. Messinger, and S.R. Manalis, *Making it stick: convection, reaction and diffusion in surface-based biosensors*. Nature Biotechnology, 2008. **26**(4): p. 417-426.
35. Jungbauer, A., *Chromatographic media for bioseparation*. Journal of Chromatography A, 2005. **1065**(1): p. 3-12.
36. Fachin, F., et al., *Integration of bulk nanoporous elements in microfluidic devices with application to biomedical diagnostics*. Journal of Microelectromechanical Systems, 2011. **20**(6): p. 1428-1438.

37. Hui, C.Y., et al., *Constraints on microcontact printing imposed by stamp deformation*. Langmuir, 2002. **18**(4): p. 1394-1407.
38. Goh, C., K.M. Coakley, and M.D. McGehee, *Nanostructuring titania by embossing with polymer molds made from anodic alumina templates*. Nano Lett., 2005. **5**(8): p. 1545-1549.
39. Burnouf, T. and M. Radosevich, *Nanofiltration of plasma-derived biopharmaceutical products*. Haemophilia, 2003. **9**(1): p. 24-37.
40. Eroshkin, A.M., et al., *bNAber: database of broadly neutralizing HIV antibodies*. Nucleic Acids Research, 2014. **42**(D1): p. D1133-D1139.
41. Zhou, J., et al., *Novel dual inhibitory function aptamer-siRNA delivery system for HIV-1 therapy*. Molecular Therapy, 2008. **16**(8): p. 1481-1489.
42. Xu, Y.H., X.R. Yang, and E.K. Wang, *Review: Aptamers in microfluidic chips*. Analytica Chimica Acta, 2010. **683**(1): p. 12-20.



## Chapter 4

# Micropatterned Macroporous Structures in Microfluidic Devices for Viral Separation from Whole Blood

### 4.1: Abstract

Separation and enrichment of bionanoparticles from cells are critical steps in many chemical and biomedical practices. We demonstrate here the design and fabrication of a microfluidic immunochromatographic device incorporating regular and multiscale structures to capture viruses from blood. The device contains micropatterned arrays of macroporous materials to perform size-exclusion and affinity chromatography in a simple flow-through process. The microscale gap in the array allows the passage of cells while the macroporous matrices promote viral capture. Computational analyses reveal that fluid permeation into the porous matrices is controllable by the micropattern separation distance and dimensions. Experimental analyses using blood samples containing human immunodeficiency viruses (HIV) as a model system further prove significantly improved viral capture efficiency using devices incorporating multiscale structures than those containing solid micropatterns. At the same time, blood cells flowed around the

micropatterns without clogging the device. Such microfluidic devices containing regular and multiscale structures have a potential for the separation and concentration of a wide range of bioparticles as well as macromolecules from complex mixtures.

## **4.2: Introduction**

Separating and enriching bio-nanoparticles from a complex mixture of multiscale species are critical steps in many applications such as diagnosis of infectious agents [1-3], pharmaceutical productions of drug loaded vesicles [4, 5], and assessment of water and food safety [6, 7]. Conventionally, bionanoparticle samples are processed through centrifugation [2], filtration [5], electrophoresis [3, 8], magnetic separation [7, 9], and chromatography [10]. Although these techniques have been routinely performed, complex reagents and procedures, sophisticated lab equipment, and skilled operators are usually involved. With rising demands of bio-nanoparticle processing and detection at resource-limited settings, alternative approaches for their separation are needed.

Microfluidic devices hold a great potential for sample processing with little infrastructure requirement. Miniaturized devices employing centrifugal [11], magnetic [12, 13], filtration [14], chromatographic [15], and dielectrophoretic [16] principles have been created to separate viruses and vesicles from cells. However, these devices face various challenges such as limited g-force to concentrate viruses, clogging, and undesirable electrochemical reactions. Hydrodynamic fractionation based on inertial effect in microfluidic devices has been demonstrated to sort microparticles [17]. Yet, the inertia effect is weak and ineffective for nanospecies.

Recently, immunoaffinity microfluidic devices have been reported to capture cells and pathogens in a simple flow-through process [18, 19]. A high capture yield is warranted by matching the characteristic dimension of the capture bed with the target particles to promote their interactions. For example, solid micropost arrays have been

introduced in microfluidic devices to isolate extremely rare circulating tumor cells from whole blood [20, 21]. Materials with nanoscale pores have been shown to isolate molecules and bio-nanoparticles with high yields [22]. Considering a nanoparticle sample in a multiscale mixture, such as viruses in blood, it has been hypothesized that a capture bed containing multiscale characteristic dimensions will outperform that with solid micropatterns. To test this idea, Fachin *et al.* [23] fabricated an array of circular islands made of vertically aligned carbon nanotubes, which allowed fluid to partially permeate into the porous microposts. Chen *et al.* [24] further utilized the device for multiscale separation and found that capture yields of both micro- and nanoparticles were enhanced compared to devices with solid islands. The enhancement is a result of minimized boundary layer around the islands and nanoparticle penetration. Yet, spacing of the carbon nanotubes is limited to 80 nm, which prevents the entry of larger nanoparticles, such as HIV virions.

Built on our prior work of macroporous material fabrication in Chapter 3, we created micropatterned macroporous elements permeable to particles up to 200 nm for HIV viral separation from human blood. We first investigated how the micropattern geometry and separation distance influence fluid permeation into the pattern using a numerical method. Afterwards, we experimentally tested the capture of HIV particles from plasma and whole blood using one selected micropattern design. The results support the concept of enhancing particle separation and concentration by multiscale features in microdevices

### **4.3: Experimental details**

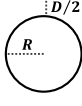
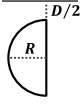
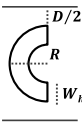
#### **4.3.1 Computational fluid dynamics simulation**

2D simulations were carried out by COMSOL Multiphysics to evaluate fluid permeation into micropatterned macroporous islands. 2D micropatterns studied here included a circle, a half circle, and a half ring (Table 1). The patterns had porosity and permeability of 0.7 and  $1 \times 10^{-13} \text{ m}^2$ , respectively, corresponding to materials used in the experiments in Chapter 3. Each pattern was centered between two parallel plates. The gap distance from the pattern edge to one plate wall was  $D/2$ . The Creeping Flow and Brinkman Equations modules were coupled in the simulation. The plates were set as periodic boundaries. An average inflow velocity of 1 mm/s was set at the inlet. The density and viscosity of the fluid were  $1000 \text{ kg/m}^3$  and  $0.001 \text{ Pa}\cdot\text{s}$ , respectively. Volume fraction of fluid permeating into the porous element was calculated from the equation (4.1),

$$\text{Volume fraction} = \frac{\int_S (\mathbf{u} + \mathbf{v}) \cdot d\mathbf{s}}{\int_d (\mathbf{u} + \mathbf{v}) \cdot d\mathbf{s}} \times 100\% \quad (4.1)$$

where  $\int_S (\mathbf{u} + \mathbf{v}) \cdot d\mathbf{s}$  and  $\int_d (\mathbf{u} + \mathbf{v}) \cdot d\mathbf{s}$  are fluxes into the porous elements and from the inlet, respectively. Dimensional variables in this study were radius of the patterns ( $R$ ), gap distance between the pattern edge and the wall ( $D/2$ ), and ring width ( $W_{hr}$ , for the half-ring pattern only) (Table 4.1).

Table 4.1: Design variables of micropattern geometry and layout for testing permeation volume fraction.

<i>Micro patterns</i>		<i>Gap distance</i> ( $D$ , nm)	<i>Radius</i> ( $R$ , nm)	<i>Width of the half ring</i> ( $W_{hr}$ , nm)
Circle		50, 100, 200	150, 300, 600	-
Half circle		50, 100, 200	150, 300, 600	-
Half ring		50, 100, 200	150, 300, 600	25, 50, 100

### 4.3.2 Materials

SU-8 photoresist was obtained from MicroChem (Newton, MA). Sylgard 184 silicone elastomer kit was purchased from Dow Corning (Midland, MI). Polystyrene (PS) sheets were obtained from Plaskolite (Columbus, OH). A binary suspension containing 20 vol% of 1- $\mu\text{m}$  silica beads and 8 vol% of 100-nm PS beads was kindly provided by Gilchrist lab at Lehigh University (Bethlehem, PA). Lyophilized bovine serum albumin (BSA) was purchased from Sigma Aldrich (St. Louis, MO). Phosphate buffered saline (PBS) was obtained from Mediatech (Herndon, VA). NeutrAvidin biotin-binding protein was from Thermo Scientific (Rockford, IL). Green fluorescent 10- $\mu\text{m}$  PS beads and red fluorescent 100-nm PS beads were purchased from Thermo Scientific (Fremont, CA). An HIV-1 p24 enzyme-linked immunosorbent assay (ELISA) kit was obtained from Perkin-Elmer (Waltham, MA). Human blood from healthy donors was kindly provided by Network Office of Research and Innovation at Lehigh Valley Health Network (Allentown, PA).

### 4.3.3 Device fabrication

An array of half-ring pattern was incorporated into microfluidic channels for HIV separation. The half-ring pattern had a height of 30  $\mu\text{m}$ , outer radius ( $R$ ) of 150  $\mu\text{m}$ , gap distance ( $D$ ) of 100  $\mu\text{m}$  and ring width ( $W_{hr}$ ) of 50  $\mu\text{m}$ . They were hexagonally arranged within an area of 25 mm  $\times$  10 mm (length  $\times$  width). To fabricate the half-ring array, polydimethyl siloxane (PDMS) molds with a negative feature were created first using standard soft-lithography techniques. The PDMS mold was treated by corona discharge to promote hydrophilicity. Next, a 10  $\mu\text{L}$  suspension containing 20 vol% of 1- $\mu\text{m}$  silica

and 8 vol% of 100-nm PS was pipetted and spread on the PDMS mold. The binary suspension was allowed to dry at room temperature, and the silica beads self-assembled into a close packed structure with the PS nanoparticles filling the interstitial space. Then the PS nanobeads were melt at 240 °C for 10 min to form a continuous matrix surrounding silica beads. The sample was glued to a PS flat piece by epoxy and the PDMS mold was peeled off after epoxy was cured. At this point, solid half-ring patterns were revealed. To create porous half rings, silica beads were removed by 50% hydrofluoric acid and the sample was rinsed by de-ionized (DI) water, leaving a PS network of interconnected spherical pores. To cap the device, a 25 mm × 8 mm PS roof drilled with an inlet and outlet was attached on the pattern array using a double-sided tape. The device was finally connected with tubing and sealed with epoxy glue (Figure 4.1(A)-4.1(E)). The final footprint of the micropatterned region was 25 mm × 8 mm as shown in Figure 4.1(F).



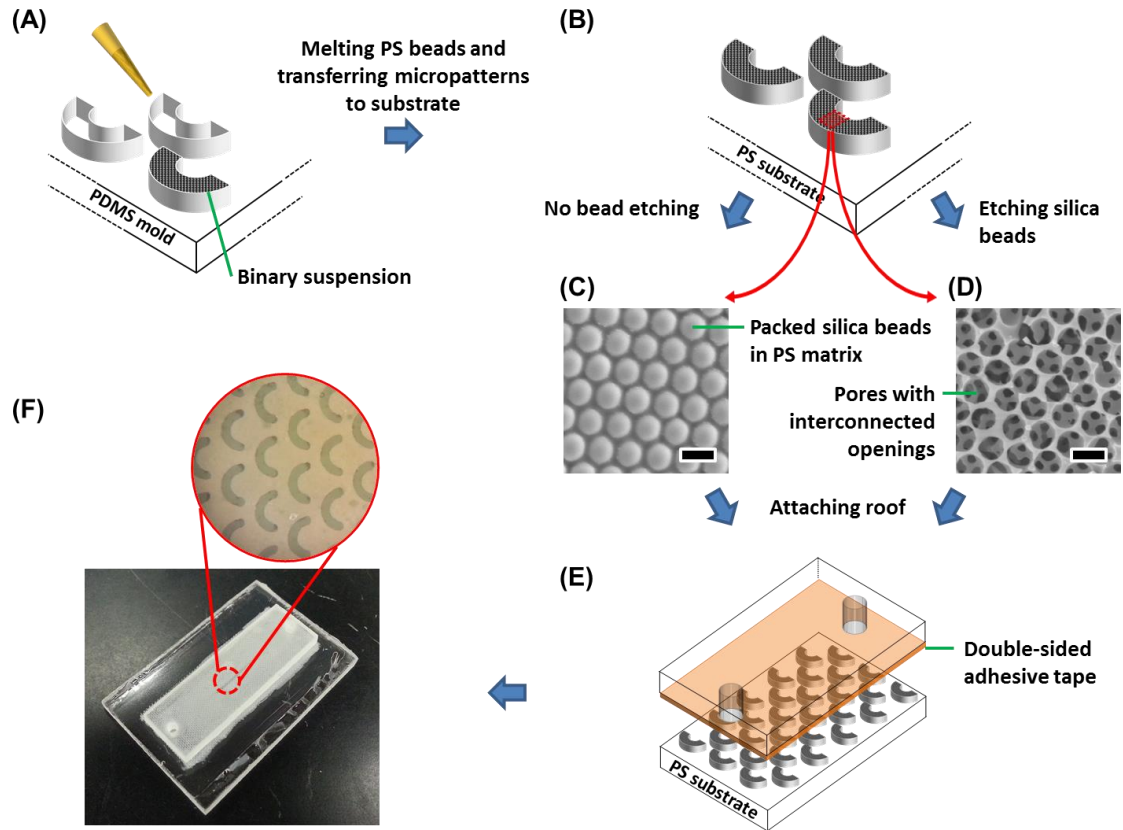


Figure 4.1: Schematics showing the fabrication process of half-ring micropatterns with solid or porous structures. (A) Deposition of binary suspension in a micro-patterned PDMS mold. (B) Transferring the micropatterned half-ring array to a flat substrate. The micropatterns are either (C) solid without silica bead removal or (D) containing interconnected spherical pores after silica bead removal. (E) Capping the array with a roof to form a microfluidic device. (F) Photograph of an assembled microfluidic device containing an array of half-ring micropatterns used for viral separation.

#### **4.3.4 Sample characterization**

The micropatterned macroporous structures were characterized by a field-emission scanning electron microscope (FE-SEM – Hitachi 4300) and the geometries were measured from SEM images using ImageJ software.

#### **4.3.5 Surface modification**

Microfluidic devices were functionalized with NeutrAvidin for specific capture of biotinylated HIV viruses. Firstly, all devices were washed with 70% isopropanol and DI water. Afterwards, the microchannels were incubated with 10 µg/mL NeutrAvidin for 2 hrs at room temperature to allow physisorption. Finally, the devices were rinsed with 1% BSA/PBS and used for viral capture immediately. To test nonspecific binding, devices were prepared by physisorption with 1 % BSA/PBS, instead of NeutrAvidin, for 2 hrs at room temperature.

#### **4.3.6 Viral production**

Pseudotyped HIV particles were cultured [25] and biotinylated [26] following procedures in the literature. Briefly, HEK-293T cells were transfected with four plasmids of pGag-eGFP, pcRev, pR8ΔEnv, and pJR-FL in DMEM using MegaTran 1.0. After a 24-48 hrs incubation period, the cells were washed with PBS and incubated with 1.67 mM Sulfo-NHS-LC-Biotin in PBS at room temperature for 30 min. The cells were then washed with PBS and 100 mM glycine to remove excess biotin, and re-cultured in the HEK culture medium for another 24 hrs. Subsequently, the supernatant was filtered and centrifuged to concentrate the biotinylated HIV particles. The viral pellet was resuspended in the HEK culture medium and stored at -80 °C.

#### **4.3.7 Transport of fluorescent micro- and nanobeads in the microfluidic devices**

To visualize particle transport in the micropatterned porous array, fluorescent micro- and nanobeads were used. A device was rinsed with 70% isopropanol and DI water, followed by incubation with 1% BSA/PBS for 2 hrs. Green fluorescent 10- $\mu\text{m}$  PS beads and red fluorescent 100-nm PS beads were mixed together at equal volume and 0.5 vol% each. The suspension was injected into the device at 5  $\mu\text{l}/\text{min}$  for 60 min and then imaged. Afterward, the device was rinsed with PBS buffer at 20  $\mu\text{l}/\text{min}$  for 3 min and imaged for non-specific binding.

#### **4.3.8 Viral capture in the microfluidic devices**

Biotinylated HIV was spiked into whole blood or plasma at a concentration of  $\sim 10^6$  virions/mL. Then, the spiked blood or plasma was injected into the devices by a syringe pump at constant flow rates of 5, 20, and 100  $\mu\text{L}/\text{min}$  for a total volume of 300  $\mu\text{L}$ . An iron ball was placed in the syringe of blood to manually stir blood periodically during the injection.<sup>28</sup> Afterwards, all devices were rinsed with PBS, and captured HIV was lysed on chip using 0.5% Triton X-100. The outflow from the viral injection, PBS wash, and Triton lysis steps were collected separately and analyzed for the amount of HIV virions. Volume of the PBS wash was tested ahead of time to ensure all free viruses were rinsed out before lysis. Flow-through samples containing blood were centrifuged to separate blood cells before HIV quantification. Amount of HIV was measured using a p24 ELISA kit. The input viral solution was also tested for HIV concentration to confirm

mass balance between input and output. The capture results from 4 samples of each condition were statistically analyzed by a two-tailed Student's t-test.

#### **4.4: Results and Discussion**

Considering the application of bio-nanoparticle separation from cells, we hypothesize that an affinity capture bed containing hierarchical features, both on the micron and submicron scales, will outperform that with microfeatures alone. To select an appropriate design to test this hypothesis, we first performed 2D COMSOL simulation to understand how geometry of porous micropatterns controls fluid permeation. We fixed the structure of the macropores, and varied the shape and spacing of the micropatterns. Using an average inlet velocity of 1 mm/s, dimensional analysis indicates that nanoparticle transport in the microscale gap of 50-200  $\mu\text{m}$  is dominated by convection. On the other hand, nanoparticle transport in the porous islands is diffusion dominated. Additionally, Chen *et al.* [24], reported fluorescent molecules permeating gradually from the front to the back of a porous cylindrical post. These phenomena suggest that the back of the micropatterns has low probability to interact with the target for affinity separation, while removing them could significantly reduce flow resistance of the porous posts. We first simulated fluid permeation in three different micropatterns, a full circle, a half-circle and half-ring to represent microposts of the corresponding x-y cross-sectional shapes. The pattern with the highest permeability and compatible with the fabrication process was then fabricated to test HIV capture from whole blood experimentally.

#### 4.4.1 Computational analysis

We first used COMSOL Multiphysics software to simulate water permeation into macroporous patterns of three different geometries, a circle, a half circle, and a half ring, considering plausible short mean-free path of nanoparticles in the porous matrix. 2D geometries were placed between two parallel plates (Table 4.1). Three parameters were varied in the simulation: radius of the pattern ( $R$ ), gap distance between the wall and the pattern edge ( $D/2$ ), and ring width ( $W_{hr}$ , for the half-ring pattern only). Figure 4.2 shows the maps of fluid velocity profile inside three porous patterns with  $R = 150 \mu\text{m}$ ,  $D = 100 \mu\text{m}$ , and  $W = 50 \mu\text{m}$ , and plotted on comparable scales. As predicted, the average velocity increases from the circle to half circle and further to the half ring patterns of the same radius, due to reduced flow resistance. The first two patterns demonstrate an order of magnitude higher velocity at the two poles than other regions. The half-ring pattern on the other hand, has even higher velocity and more uniform velocity distribution, thus providing a more consistent environment for nanoparticle capture.

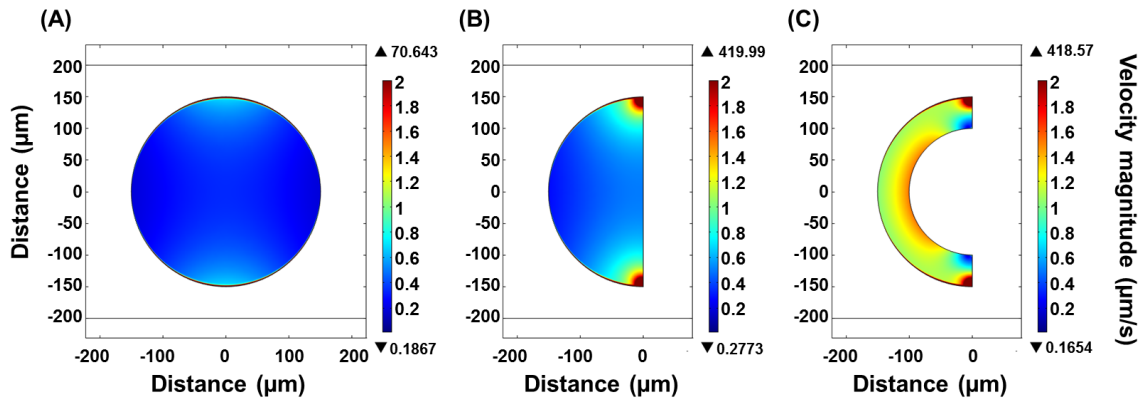


Figure 4.2: Maps of fluid velocity magnitudes inside (A) circle, (B) half-circle, and (C) half-ring patterns. Flow is from the left to the right.

Fraction of water permeating into each porous structure was then computed using Equation (4.1). We first investigated the effect of gap distance  $D$  varied from 50 to 200  $\mu\text{m}$  with fixed  $R = 150 \mu\text{m}$  and  $W_{hr} = 100 \mu\text{m}$  (Figure 4.3(A)). Permeation is less than 1% in all simulated geometries, since the flow resistance of the macroporous patterns is much higher than that of the separation gap ( $D$ ). At the same  $D$ , 3-7 times less water permeates into the circular pattern than the other two patterns, and the half ring has slightly higher permeation than the half circle. This is not surprising since resistance of a porous structure scales with its thickness, and the circular pattern is twice as thick as the half circle. The resistance is further reduced in the half ring at the same radius. Additionally, large resistance of the circular pattern also makes it more sensitive to  $D$ . Permeation in the circle, half circle, and half ring drops by 22.88, 10.36, and 10.63 times, respectively, when  $D$  is widened from 50  $\mu\text{m}$  to 200  $\mu\text{m}$ .

Next we evaluated the effect of radius  $R$  in the range of 150 to 600  $\mu\text{m}$  with fixed  $D = 100 \mu\text{m}$  and  $W_{hr} = 100 \mu\text{m}$  (Figure 4.3(B)). The permeable fraction increases by 1.75, 1.25, and 2.43 folds with an increase of  $R$  from 150 nm to 600 nm for the circle, half-circle and half-ring patterns, respectively. Furthermore, the effect of the width of the half-ring pattern was studied. With all other parameters held constant, the permeable fraction increases as the width is decreased (Figure 4.3(C)). Reducing the width from 100  $\mu\text{m}$  to 25  $\mu\text{m}$  leads to an improvement of permeation by 1.76 times. According to the simulation results, the gap distance is more effective than the other two parameters in regulating fluid permeation into porous micropatterns. Although analytical solutions of flow resistance in the gap and micropatterns are not available, the observed dependence

of fluid permeation on  $D$ ,  $R$  and  $W$  can be qualitatively understood from scale analysis. The resistance for laminar flow between infinite parallel plates scales with the separation distance ( $d$ ) to the third power. When an infinitely long tube is situated in the middle of the two plates and leaves a gap of  $D$  for fluid to go around, the average width of the flow path is between  $d$  and  $D$ , thus the flow resistance is expected to scale with  $D$  to a power between 1 and 3, consistent with our simulation results.  $R$  mainly controls the surface area orthogonal to the flow, and the flow resistance of a porous membrane scales linearly with the filtration area following Darcy's law. For the circular and semicircular patterns,  $R$  also contributes to the thickness of the porous pattern, with which the flow resistance scales linearly. The two opposite effects cause a weak dependence of permeation on  $R$ .

Porous cylindrical microposts have been reported to improve the capture yield of nanoparticles because fluid permeates into the structure and transports nanoparticles into the capture bed more efficiently [24]. Our simulation results suggest that microposts with a half-ring cross-section are more advantageous in promoting permeation, thus they are expected to yield better viral capture.



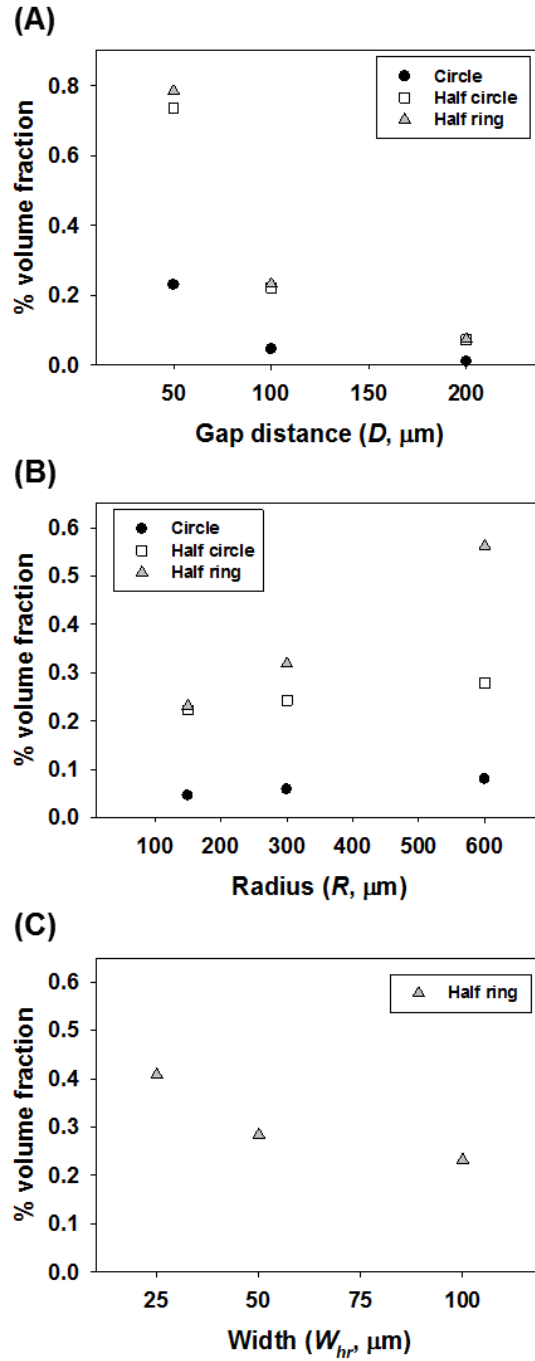


Figure 4.3: Computational results showing the effect of (A) Gap distance  $D$ , (B) outer radius  $R$ , and (C) width  $W_{hr}$  of half ring on the fluid volume fraction permeating into different porous designs.

#### 4.4.2 Fabrication of microfluidic channels with multiscale features

According to the simulation results, we fabricated microfluidic devices incorporating an array of hexagonally packed half-ring islands (Figure 4.4(A)). Both solid and porous arrays were created to compare the viral capture efficiency. The gap spacing, outer radius, and ring width are 100  $\mu\text{m}$ , 150  $\mu\text{m}$ , and 50  $\mu\text{m}$ , respectively. To form solid microposts, a mixture of silica microbeads and polystyrene nanospheres was deposited in a PDMS mold followed by melting the polystyrene nanospheres (Figure 4.4(B)). On the other hand, the porous microposts were created with the same pattern geometry while silica beads were etched off (Figure 4.4(C)). The porous structure presented an ordered spherical pore network with small interconnected openings. The size of interconnected opening is  $\sim 233$  nm and the openings on the side-wall surface have an average diameter of  $695 \pm 56$  nm. The pore density on the side wall is  $\sim 1 \times 10^8$  pores/ $\text{cm}^2$  and the bulk permeability of the macroporous matrix is  $\sim 1 \times 10^{-13}$   $\text{m}^2$ , as reported in Chapter 2. The highly porous material allows permeation of fluids and transport of nanoparticles to the large affinity area inside the microposts.

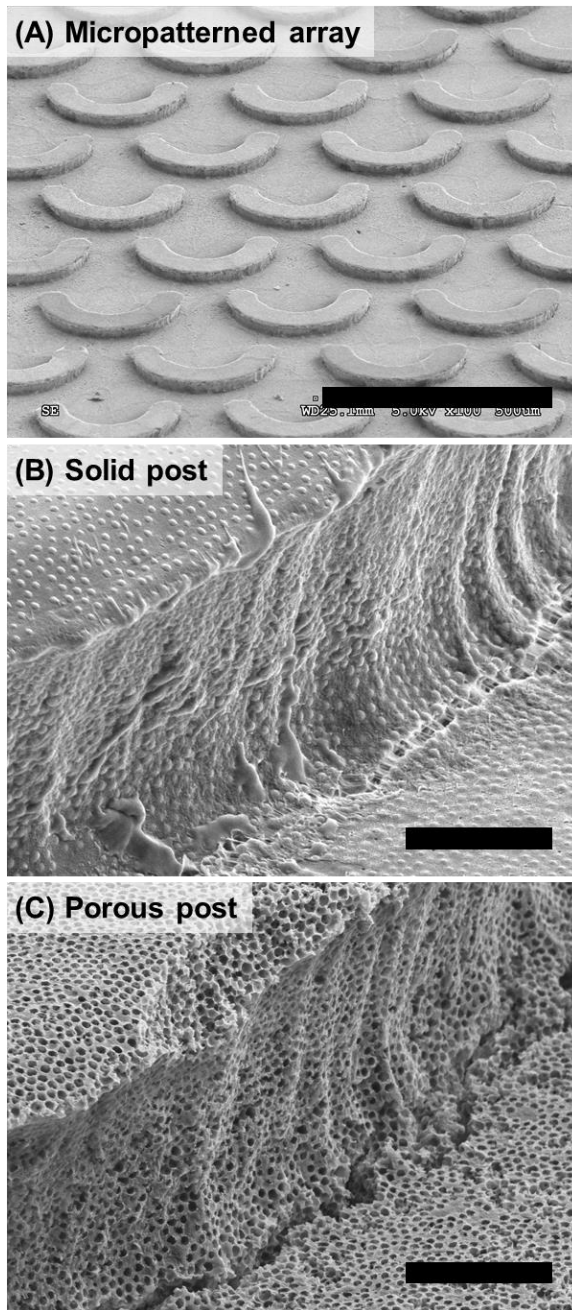


Figure 4.4: SEM images showing (A) a half-ring micropatterned array ( $D = 100 \mu\text{m}$ ,  $R = 150 \mu\text{m}$ , and  $W_{hr} = 50 \mu\text{m}$ ). (B) A zoomed-in image showing a side wall of a solid post where silica beads are surrounded by a PS matrix. (C) A side wall of a patterned porous post showing pore openings on the surface after silica bead removal. The side-wall openings were measured to be  $695 \pm 56 \text{ nm}$ . All SEM images were taken at  $\sim 50^\circ$  to  $55^\circ$  tilted. Scale bars are  $500 \mu\text{m}$  in (A) and  $10 \mu\text{m}$  in (B) and (C).

#### 4.4.3 Transport of fluorescent micro- and nanobeads in the device

To demonstrate size exclusion of the porous micropatterns, 10- $\mu\text{m}$  (green) and 100-nm (red) fluorescent beads were mixed together and flowed into a device with macroporous patterns. While most particles flow around the posts, a small number of 10- $\mu\text{m}$  particles (green) slowly accumulate in front of the posts, while some 100-nm beads (red) accumulate inside the porous posts (Figure 4.5(A)). The accumulation of microbeads is consistent with Chen's observation [24] that streamlines penetrate porous micropatterns and promote microparticle interaction with the islands. The nanobead distribution is relatively uniform inside the half-ring, suggesting penetration of fluid along the entire frontline. Nonspecifically trapped microparticles can be mostly rinsed out by increasing the flow rate from 5 to 20  $\mu\text{m}/\text{min}$ , while some nanoparticles remain inside the posts (Figure 4.5(B)). The observation of fluorescent micro- and nanobead distribution in the device confirms that the micropatterned porous device can separate the two sized particles.

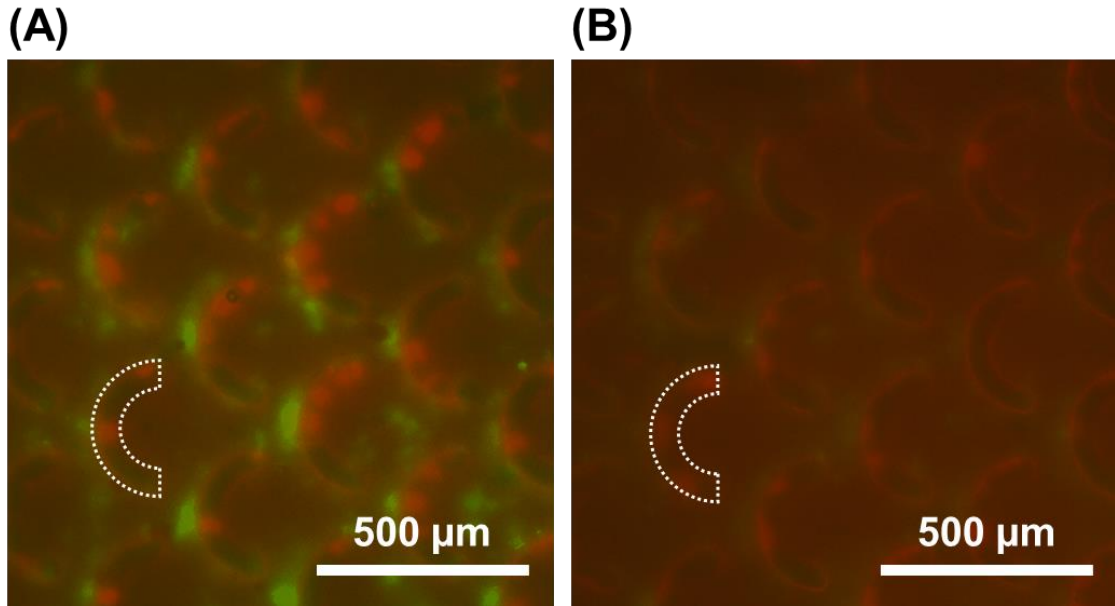
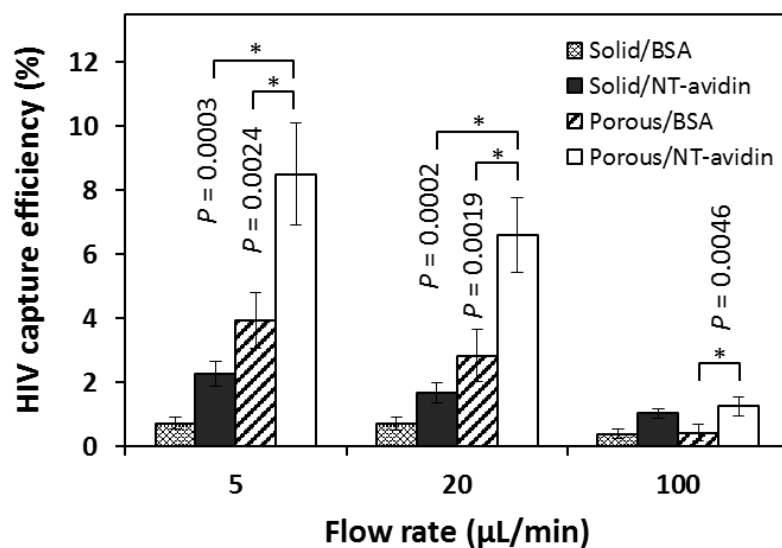


Figure 4.5: Fluorescence images showing distribution of physically trapped 10- $\mu\text{m}$  (green) and 100-nm (red) particles in a device with micropatterned macroporous islands. (A) While most of the beads flow around the posts, a small number of microbeads accumulate in front of the microposts whereas some 100-nm beads penetrate inside the porous posts. The images were taken after flowing the mixture for 60 min at 5  $\mu\text{m}/\text{min}$ . (B) While most of the 10- $\mu\text{m}$  beads can be rinsed off at 20  $\mu\text{m}/\text{min}$ , some 100-nm beads remain physically trapped inside the porous array after rinse.

#### 4.4.4 Viral capture in micropatterned devices

Viral capture was performed first using virus spiked plasma (Figure 4.6(A)). The same volume of samples was flowed into functionalized devices at various flow rates of 5, 20 and 100  $\mu\text{L}/\text{min}$ . For devices containing solid posts functionalized with NeutrAvidin, the capture yield increases slightly from  $1.04 \pm 0.14 \%$  to  $2.29 \pm 0.38 \%$  when the flow rate drops from 100 to 5  $\mu\text{L}/\text{min}$ . On the other hands, devices with the porous array and functionalized with NeutrAvidin yield significantly higher efficiency, ranging from  $1.26 \pm 0.29 \%$  to  $8.51 \pm 1.59 \%$  as the flow rate decreases from 100 to 5  $\mu\text{L}/\text{min}$ . Nonspecific binding in the solid array devices treated with 1 % BSA remains relatively constant at  $<1 \%$  regardless of the flow rate. In the BSA passivated porous devices, the nonspecific binding increases from  $0.48 \pm 0.22 \%$  at 100  $\mu\text{L}/\text{min}$  to  $2.68 \pm 0.77 \%$  at 5  $\mu\text{L}/\text{min}$ .

### (A) Plasma



### (B) Blood

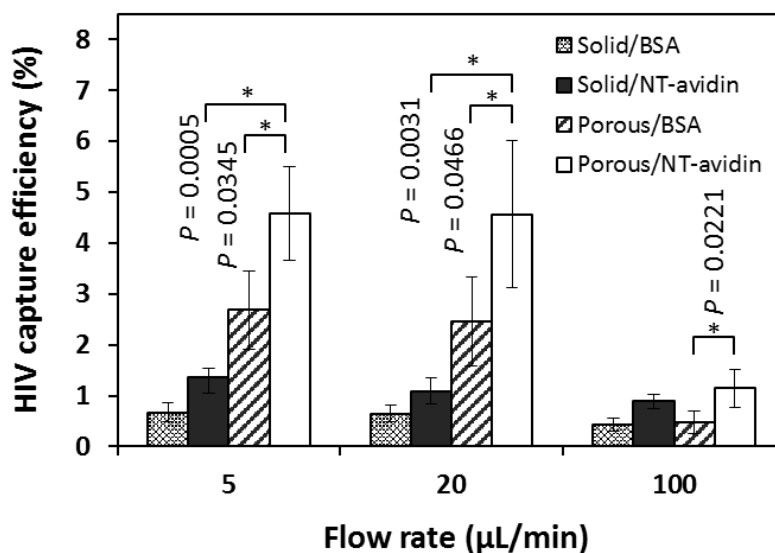


Figure 4.6: HIV capture efficiency in the solid and porous post devices under different flow rates from (A) blood plasma and (B) whole blood. The devices were functionalized by 1% BSA/PBS or NeutrAvidin. The error bars represent standard deviation from 4 samples. Statistical analysis was performed using a two-tailed Student's t-test at a 95% confidence interval.

Next viral capture was tested from whole blood using micropatterned devices. During blood injection, blood cells were found flowing around the patterned array and no clogging was observed. Similar to the capture results from plasma, higher capture yields are achieved at lower flow rates, while the yield is generally lower in blood than in plasma (Figure 4.6(B)). With NeutrAvidin-treated solid arrays,  $0.89 \pm 0.14$  %,  $1.09 \pm 0.25$  %, and  $1.36 \pm 0.30$  % of virus are captured at the flow rates of 100, 20 and 5  $\mu\text{L}/\text{min}$ , respectively. Functionalized porous arrays yield  $1.15 \pm 0.38$  %,  $4.57 \pm 1.44$  %, and  $4.58 \pm 0.92$  % virus at these flow rates. Nonspecific binding in BSA treated devices is lower than NeutrAvidin functionalized counterparts, while significantly more nonspecific binding is observed in the porous array than the solid one. The greater nonspecific binding is a result of low velocity inside the porous matrix, which leads to a weak wall shear force on the order of  $10^{-17}$  N that is insufficient to detach nonspecifically bound particles.

Compared to that in plasma, the capture yield in whole blood is reduced, suggesting insignificant margination of viruses in whole blood. Margination of white blood cells and platelets have been reported both in vivo and in artificial microchannels due to the concave shape and deformability of red blood cells.[28, 29] However, margination of bio-nanoparticles remains a subject of debate. Toy *et al.*[30] demonstrated that liposomes sized 60-130 nm can marginate to microchannel walls. In contrast, Charoenphol *et al.*[31] reported that particles sized below 500 nm do not marginate. Lee *et al.*[28] also showed that 10-nm to 200-nm polystyrene beads are homogeneously dispersed under a capillary flow both in vivo and by computational analyses. Our results



indirectly support the latter view. Another possibility to lower yield from blood is margined white blood cells and platelets impeding the penetration of HIV particles into the porous micropatterns, while teasing apart these possibilities will require additional investigation.

Overall, microfluidic channels containing multiscale materials enhance the capture yield of bio-nanoparticles from a complex fluid such as blood. The microscale gaps permit the passage of blood cells, while the macroporous structure inside the micropattern allows nanoparticle permeation for affinity capture. The Péclet numbers of viral particle in the microscale gap and macroporous matrix are on the order of  $10^4$  and  $10^{-2}$  respectively. Thus different transport mechanisms are dominated inside and out of the microposts. Compared to solid microposts, porous microposts have two advantages for viral capture. First, the affinity area is improved by order of magnitude with the macroporous structures. Second, the porous micropattern allows penetration of streamlines and promotes transport of nanoparticles to the affinity surface. Since convection velocity at the boundary of porous micropatterns is non-zero,[24] nanoparticles are transported into the micropatterns by both convection and diffusion. In contrast, nanoparticles rely on diffusion to cross the boundary layer around solid posts before their interaction. As a result, the porous array captures up to 4 times more HIV virions than the solid array. Similarly, Chen *et al.*[24] demonstrated that a porous array of intertwined carbon nanotubes enhanced capture efficiency of cells and bacteria by ~6 times on the exterior surface of the microposts compared to a solid array of the same geometry, due to a reduced boundary layer.

While permeation is not expected to change with the flow rate, the residence time is reduced as the flow rate increases. Short residence time limits viral diffusion from the central streamline in the interpost gap to the micropost surface and leads to dampened capture efficiency at high flow rates. The capture yield, although less than 10% from either plasma or blood, is comparable to the yield of plasma extraction devices reported in the literature. Compared to simple plasma extraction, our device also offers the possibility to concentrate viruses through processing sample volumes much larger than the microchannel volume.

Different from prior work where circular microislands were designed, we selected a half-ring array to reduce the flow resistance of the porous island and promote permeation. The backside of the circular micropattern has a low probability to interact with the virus. By eliminating the less efficient volume, the permeation is increased by more than 6 times for the half-ring posts. Although simulation predicts better permeation with even narrower half-ring widths, a porous array can collapse during device assembly or fluid injection if the width becomes too narrow. The selected geometry represents a balance between performance and practicality. Also, the capture yield is expected to further improve with the capture-bed length and residence time. The micropatterned devices are operated with a simple flow-through process, which can continuously handle a large fluid volume. As a result, target particles can be separated and concentrated to facilitate downstream detection.

#### **4.5: Conclusions**

Microfluidic devices incorporating functionalized hierarchical structures are fabricated in this work and shown to capture viruses more efficiently than devices with microposts alone. The enhancement is a result of viral permeation into the porous posts and specific interaction with the large affinity area. The separation happens in a continuous-flow process relying on physical and biochemical interaction, while little infrastructure is required. As an easy-to-use device for multiscale separation, the device may find applications in pathogen sample processing in resource-limited settings.

#### **4.6: References**

1. Stevens, S.J.C., I. Pronk, and J.M. Middeldorp, *Toward standardization of Epstein-Barr virus DNA load monitoring: Unfractionated whole blood as preferred clinical specimen*. Journal of Clinical Microbiology, 2001. **39**(4): p. 1211-1216.
2. Towner, J.S., et al., *Rapid diagnosis of Ebola hemorrhagic fever by reverse transcription-PCR in an outbreak setting and assessment of patient viral load as a predictor of outcome*. Journal of Virology, 2004. **78**(8): p. 4330-4341.
3. Mironov, G.G., et al., *Viral quantitative capillary electrophoresis for counting intact viruses*. Analytical Chemistry, 2011. **83**(13): p. 5431-5435.
4. Morenweiser, R., *Downstream processing of viral vectors and vaccines*. Gene Therapy, 2005. **12**: p. S103-S110.
5. Burnouf, T. and M. Radosevich, *Nanofiltration of plasma-derived biopharmaceutical products*. Haemophilia, 2003. **9**(1): p. 24-37.
6. Fiksdal, L. and T. Leiknes, *The effect of coagulation with MF/UF membrane filtration for the removal of virus in drinking water*. Journal of Membrane Science, 2006. **279**(1-2): p. 364-371.
7. Lopez-Sabater, E.I., M.Y. Deng, and D.O. Cliver, *Magnetic immunoseparation PCR assay (MIPA) for detection of hepatitis A virus (HAV) in American oyster (Crassostrea virginica)*. Letters in Applied Microbiology, 1997. **24**(2): p. 101-104.
8. Dolnik, V., *Capillary electrophoresis of proteins 2003-2005*. Electrophoresis, 2006. **27**(1): p. 126-141.
9. Lopez, C.A., et al., *Characterization of HIV-1 RNA forms in the plasma of patients undergoing successful HAART*. Archives of Virology, 2010. **155**(6): p. 895-903.
10. Kalbfuss, B., et al., *Purification of cell culture-derived human influenza A virus by size-exclusion and anion-exchange chromatography*. Biotechnology and Bioengineering, 2007. **96**(5): p. 932-944.
11. Haeberle, S., et al., *Centrifugal extraction of plasma from whole blood on a rotating disk*. Lab on a Chip, 2006. **6**(6): p. 776-781.

12. Kim, B.C., et al., *Quantitative detection of HIV-1 particles using HIV-1 neutralizing antibody-conjugated beads*. *Anal Chem*, 2009. **81**(6): p. 2388-2393.
13. Chen, G.D., et al., *Concentration and purification of human immunodeficiency virus type 1 virions by microfluidic separation of superparamagnetic nanoparticles*. *Analytical Chemistry*, 2010. **82**(2): p. 723-728.
14. Wang, S.Q., et al., *Simple filter microchip for rapid separation of plasma and viruses from whole blood*. *International Journal of Nanomedicine*, 2012. **7**: p. 5019-5028.
15. Chirica, G., J. Lachmann, and J. Chan, *Size exclusion chromatography of microliter volumes for on-line use in low-pressure microfluidic systems*. *Analytical Chemistry*, 2006. **78**(15): p. 5362-5368.
16. Akin, D., H.B. Li, and R. Bashir, *Real-time virus trapping and fluorescent imaging in microfluidic devices*. *Nano Letters*, 2004. **4**(2): p. 257-259.
17. Yamada, M., M. Nakashima, and M. Seki, *Pinched flow fractionation: Continuous size separation of particles utilizing a laminar flow profile in a pinched microchannel*. *Analytical Chemistry*, 2004. **76**(18): p. 5465-5471.
18. Cheng, X., et al., *A microfluidic device for practical label-free CD4+T cell counting of HIV-infected subjects*. *Lab on a Chip*, 2007. **7**(2): p. 170-178.
19. Mairhofer, J., K. Roppert, and P. Ertl, *Microfluidic Systems for Pathogen Sensing: A Review*. *Sensors*, 2009. **9**(6): p. 4804-4823.
20. Nagrath, S., et al., *Isolation of rare circulating tumour cells in cancer patients by microchip technology*. *Nature*, 2007. **450**(7173): p. 1235-1239.
21. Gleghorn, J.P., et al., *Capture of circulating tumor cells from whole blood of prostate cancer patients using geometrically enhanced differential immunocapture (GEDI) and a prostate-specific antibody*. *Lab on a Chip*, 2010. **10**(1): p. 27-29.
22. Xiao, Z.Y., et al., *Practical approach for macroporous structure embedded microfluidic system and the catalytic microchemical application*. *Lab on a Chip*, 2011. **11**(1): p. 57-62.
23. Fachin, F., et al., *Integration of bulk nanoporous elements in microfluidic devices with application to biomedical diagnostics*. *Journal of Microelectromechanical Systems*, 2011. **20**(6): p. 1428-1438.

24. Chen, G.D., et al., *Nanoporous elements in microfluidics for multiscale manipulation of bioparticles*. *Small*, 2011. **7**(8): p. 1061-1067.
25. Hu, Y., X.H. Cheng, and H.D. Ou-Yang, *Enumerating virus-like particles in an optically concentrated suspension by fluorescence correlation spectroscopy*. *Biomedical Optics Express*, 2013. **4**(9): p. 1646-1653.
26. Chan, L., et al., *Conjugation of lentivirus to paramagnetic particles via nonviral proteins allows efficient concentration and infection of primary acute myeloid leukemia cells*. *Journal of Virology*, 2005. **79**(20): p. 13190-13194.
27. Turitto, V.T., A.M. Benis, and E.F. Leonard, *Platelet diffusion in flowing blood*. *Industrial & Engineering Chemistry Fundamentals*, 1972. **11**(2): p. 216-&.
28. Lee, T.R., et al., *On the near-wall accumulation of injectable particles in the microcirculation: smaller is not better*. *Scientific Reports*, 2013. **3**.
29. Kim, S., et al., *The cell-free layer in microvascular blood flow*. *Biorheology*, 2009. **46**(3): p. 181-189.
30. Toy, R., et al., *The effects of particle size, density and shape on margination of nanoparticles in microcirculation*. *Nanotechnology*, 2011. **22**(11).
31. Charoenphol, P., R.B. Huang, and O. Eniola-Adefeso, *Potential role of size and hemodynamics in the efficacy of vascular-targeted spherical drug carriers*. *Biomaterials*, 2010. **31**(6): p. 1392-1402.

# Chapter 5

## Summary and Future outlook

### 5.1: Summary

Bioseparation technologies impact many fields from diagnostics and pharmaceutical production to food and environmental assessment. Although conventional technologies are effective, the requirement of expensive and bulky instruments, complex reagents and setups, and well-trained technicians makes them difficult to adopt in resource-limited regions.

In this dissertation, a materials-engineering approach is taken to answer the need of alternative separation approaches suitable for resource-poor settings. Macroporous and multiscale materials are designed to perform size-exclusion and affinity chromatography, which allow enrichment and separation of viruses from a complex mixture, such as whole blood. The materials are further integrated into microfluidic channels to enable portable and easy-to-operate devices. Combining both computational and experimental methods, not only do we demonstrate efficient separation using the rationally designed materials, we also provide fundamental insight about transport in these materials.

In term of material formation, two porous structures are fabricated with tunable characteristic dimensions to match those of target particles in the submicron range through template synthesis. The first structure is a nanopost array template from porous anodic aluminum oxide (AAO) films. Though AAO films contain a self-ordered porous structure from the conventional anodization, the degree of order is far from ideal. In this work, pre-patterning on aluminum substrate by nanobeads is introduced to successfully control the AAO formation. The results show that the AAO cell and pore sizes can be adjusted continuously under submicron range with a narrow size distribution. Moreover, the degree of order is improved while the anodization was under control without oxide film breakdown even at high anodizing voltages. The second structure is a spherical porous network with small openings in submicron range, created by templating self-assembled 1- $\mu\text{m}$  beads.

The porosities of both structures are  $\sim 70\%$  which is significantly higher than that of  $\sim 40\%$  in bead packing in chromatographic columns. Therefore, higher fluid permeation in the porous capture bed is allowed. The high surface-to-volume ratio of  $10^4$  folds over a flatbed further enhances the particle-surface interaction. Incorporated within a microfluidic device, these structures thus offer a great promise for nanoparticle separation. As a proof of principle, the porous materials are tested for HIV capture. The results show that functionalized nanopost arrays and spherical pore matrices can capture up to 99% and 80% of HIV from a buffer solution, respectively.

To demonstrate multi-scale separation, different micropatterns incorporating the macroporous materials are then designed. Computational methods are utilized to



investigate micropattern shapes and dimensions. A half-ring pattern is found to have much reduced flow resistance than a circular pattern, thus allowing more fluid permeation. Fluid permeation is further controllable through the pattern radius and gap distance. When evaluated for HIV separation from whole blood, the porous half-ring array captures ~4 times more HIV than a solid array in both plasma and whole blood.

While microfluidic devices in this dissertation mainly aim to separate HIV viruses, they can be adapted for other bionanoparticles. The device performance can be optimized by means of micropattern designs and material selection. The separation devices can be further integrated with detection modules for fully functioning diagnostics. Plans and examples of device development are discussed in the Future Outlook chapter.

## **5.2: Future outlook**

As mentioned previously, this work aims to create novel materials for bionanoparticle separation. Microdevices incorporating these materials have shown a potential in separating viruses from human whole blood. The devices can be optimized in many aspects and integrated with detection modules for fully functioning diagnostics usable at the point of care.

The separation mechanism of the devices is size-exclusion and affinity separation. While large particles are screened by the micropatterned porous element and driven through the device, target particles are brought to the porous element and become trapped in front or inside the structure. This dissertation demonstrates that HIV separation can be achieved using a spherical pore network containing interconnected openings of ~200 nm. Additionally, the porous network can be used to separate other particles as intended by appropriately tuning the pore sizes. Moreover, the porous element can be functionalized specifically for different target species [1]. This makes micropatterned devices able to be used for capture of other bio-nanoparticles in addition to viruses. . As for the spherical pore network, many research reported a tunable interconnected openings ranging from tens of nanometers to several micrometers dependent on the template particles [2, 3]. The highest porosity for spherical pore network would be limited at ~75% corresponding to the perfect crystal packing of spheres.

Alternatively, a selection of porous materials can be made which may yield a higher capture efficiency. In Chapter 3, we demonstrate that not only the spherical pore network can be used for viral capture, but also a nanopost array. In fact, the nanopost

array performs a high capture efficiency up to 99%. Unlike that of spherical pore network, the dimension of nanopost array can be adjusted independently corresponding to the template mold as demonstrated in Chapter 2. The independency of pore size, interpore distance, and porosity make nanoposts workable in a wide range separation of particles sizing from a few nanometers to hundreds of nanometers. In addition, a porosity of more than 90% can be achieved as well. However, a micropatterning method suitable for nanopost array has to be justified. Specific to the process of templating a nanopost array from AAO porous membrane, patterning must be completed before anodizing AAO films or before molding nanoposts. We demonstrate here a patterning technique based on photolithography which is processed before a final AAO anodization [4]. The patterning involves multiple steps which briefly are 1) 1<sup>st</sup> anodization of AAO film and removal, 2) vapor deposition of silica on the dimpled aluminum surface, 3) micropatterning of photoresist as a mask on top of silica layer, 4) removal of exposed silica, and 5) 2<sup>nd</sup> anodization of AAO film on the open surface. The unetched silica as a protective layer prevents a growth of anodic oxide film underneath it. As a result, a micropatterned porous AAO can be fabricated (Figure 5.1(A)). Next, PMMA nanoposts can be formed inside the AAO pores using the same method in Chapter 3 as seen in Figure 5.1(B). Nevertheless, the AAO growth rate becomes slower in the micropatterned substrate than in a regular substrate. As a result, anodization conditions need to be adjusted to control the proper pattern thickness. Another issue is non-uniform growth of micropatterned AAO. It is observed that the edge of micropatterned AAO is thinner than that in the center (Figure 5.2(A)). Moreover, a tilted growth of AAO pores is formed at the

boundary between AAO and silica layer (Figure 5.2(B) and (C)). This may be a result of the electric field redistribution around the edge which causes a slower growth rate and tilted growth of micropatterned AAO. The issue needs to be further investigated so that micropatterned AAO films can be used as a template for a micropatterned nanopost array.

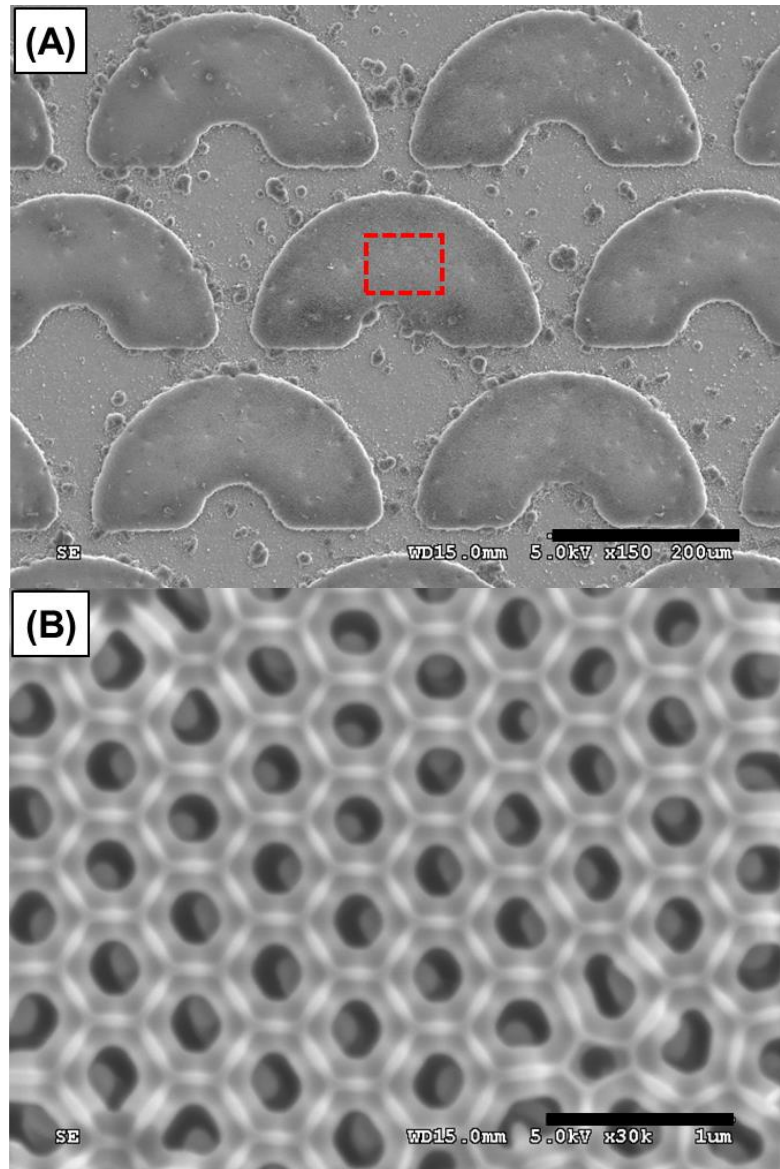


Figure 5.1: SEM images of (A) a micropatterned AAO array and (B) a zoom-in area of the dashed box in (A) showing PMMA nanoposts inside the AAO channels. Scale bars are 200  $\mu\text{m}$  in (A) and 1  $\mu\text{m}$  in (B).

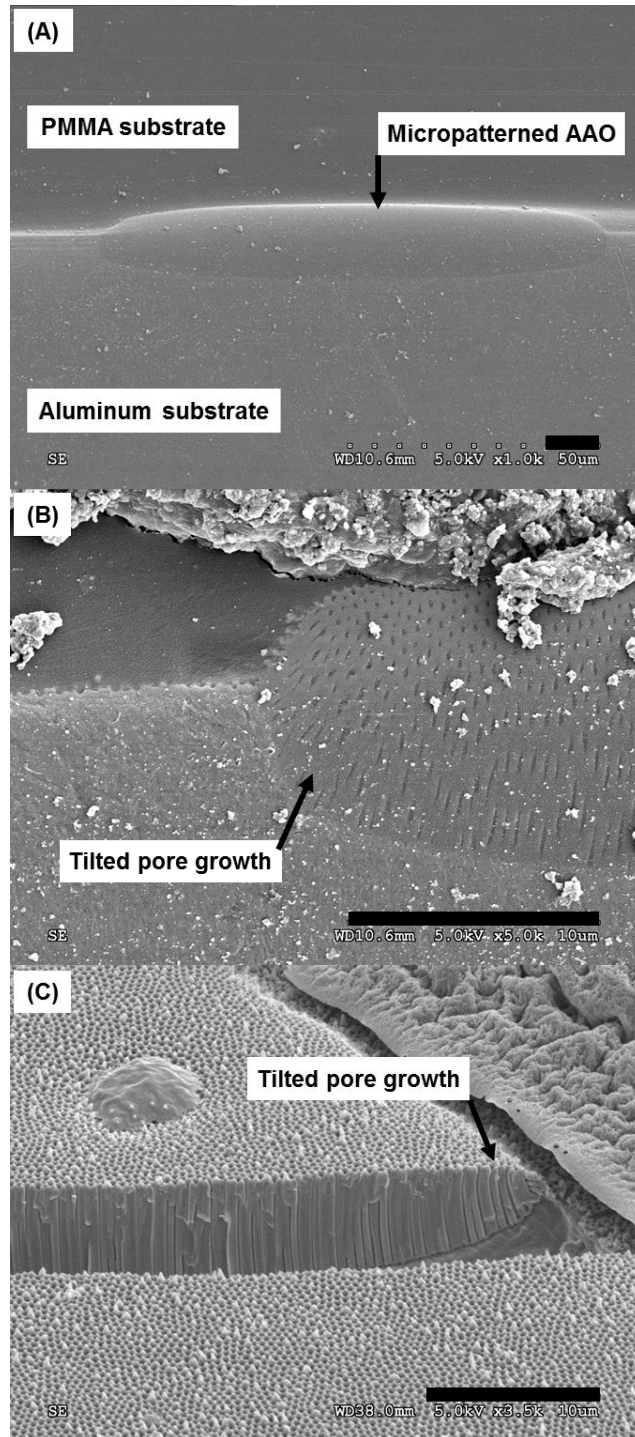


Figure 5.2: SEM images of micropatterned AAO. (A) A non-uniform growth where the edge of the oxide film is thinner than in the center. The growth of AAO pores are tilted near the boundary between AAO and silica layer as shown in cross-sectioned views by (B) polishing and (C) cracking the AAO film. Scale bars are 10  $\mu\text{m}$ .

The separation efficiency is not only affected by porous materials, but also the design of the micropattern array. Even though the half-ring pattern showed a higher fluid permeation compared with the circle and half-circle patterns in this work, the dimensions of micropattern itself can be optimized to enhance viral capture efficiency as discussed in Chapter 4. In addition, other micropatterns which may improve fluid permeation may be investigated and compared with our study.

To fully utilize the micropatterned device as a diagnostic or monitoring tool, a detection module is needed. Detection methods for microfluidic technology have been demonstrated based on various techniques for example, electrical, optical, biochemical detections or a combination of those techniques [5-8]. A detection module is under development by Kathryn Kundrod and John Fraser at Lehigh University. In their work, a voltammetric technique is used to measure currents from ion transport through the spherical pore network. In the presence of captured particles, the resistance to current flow is increased. The measured peak current consequently reduces proportionally to the captured viruses. Although this project is still under development and measurements need to be collected statistically, it has been demonstrated that the concentration of simulated virus particles could be measured quantitatively to perform a viral load measurement.

All in all, several materials suitable for viral separation are presented in this work. When incorporated into microfluidics, the devices offer simple flow-through separation and can be modified for a wide range of particle sizes. Moreover, with the further design of porous materials and micropatterns, the separation performance could be enhanced. At last, combining the sample preparation and detection modules will provide a fully

functional lab-on-a-chip device that is versatile, low-cost, and disposable. By employing the microfluidic technology, diagnostics and monitoring shall be widely accessed for a global health care.



### **5.3: References**

1. Butler, J.E., et al., The physical and functional-behavior of capture antibodies adsorbed on polystyrene. *Journal of Immunological Methods*, 1992. **150**(1-2): p. 77-90.
2. Gates, B., Y.D. Yin, and Y.N. Xia, Fabrication and characterization of porous membranes with highly ordered three-dimensional periodic structures. *Chemistry of Materials*, 1999. **11**(10): p. 2827-2836.
3. Weldon, A.L., et al., Fabrication of macroporous polymeric membranes through binary convective deposition. *ACS Applied Materials & Interfaces*, 2012. **4**(9): p. 4532-4540.
4. Park, J., et al., Fabrication of aluminum/alumina patterns using localized anodization of aluminum. *International Journal of Precision Engineering and Manufacturing*, 2012. **13**(5): p. 765-770.
5. de la Escosura-Muniz, A. and A. Merkoci, A nanochannel/nanoparticle-based filtering and sensing platform for direct detection of a cancer biomarker in blood. *Small*, 2011. **7**(5): p. 675-682.
6. Akin, D., H.B. Li, and R. Bashir, Real-time virus trapping and fluorescent imaging in microfluidic devices. *Nano Letters*, 2004. **4**(2): p. 257-259.
7. Sia, S.K., et al., An integrated approach to a portable and low-cost immunoassay for resource-poor settings. *Angew. Chem. Int. Ed. Engl.*, 2004. **43**(4): p. 498-502.
8. Chin, C.D., et al., Microfluidics-based diagnostics of infectious diseases in the developing world. *Nature Medicine*, 2011. **17**(8): p. 1015-1019.

# Vita

Krissada Surawathanawises was born in Thailand to Surawathanawises family as the youngest among four children. He attended a high school at Suankularb Wittayalai Nonthaburi and graduated in 2001. Then, he attended a Bachelor of Engineering (B.E.) in Materials Engineering at Kasetsart University in Bangkok, Thailand. In his junior year, Krissada had an internship at Spansion (Thailand) Limited company and was hired to continue a project titled “Study of Characteristics of Intermetallic Compounds on Lead-Free Solder Joints” as for his senior project. His work was awarded as an Outstanding Senior Project Award at Kasetsart University in 2005. In the same year, Krissada graduated Kasetsart University with his Bachelor’s degree with second class honours.

In 2005, Krissada became a research assistant in Materials Engineering department at Kasetsart University and cooperates with Belton Industrial (Thailand) Limited company. He had worked in material characterizations for electronic materials for the company as well as other related company. Later in 2006, Krissada was appointed as a lecturer in Materials Engineering department at Kasetsart University. During year 2006-2008, he had opportunities to teach in lecture and lab classes including Materials Science for Engineers, Materials Characterization, Materials Processing Laboratory, and Physical Metallurgy Laboratory.

Krissada had received a scholarship as a Thai Royal Scholar and later in 2008 he moved to Bethlehem, Pennsylvania, USA to pursue his doctorate in Materials Science and Engineering at Lehigh University. He worked as a research assistant with Professor

Xuanhong Cheng in The Lab of Micro- and Nanotechnology for Diagnostics and Biology. He has a strong interest in microfluidic technology and works on developing microfluidic devices towards viral diagnostics as a global health care.

Outside the academic research, Krissada enjoys both indoor and outdoor sports such as basketball, tennis, golf, bowling, and go-kart. These activities help maintain his physical balance and strength very well. Also, he spends time on practicing a guitar and ukulele for his musical life style which can relax his stresses from academic work. Krissada likes to travel around and learns new cultures while he has a chance. Indeed, he was inspired to learn photography which helps him impressively memorize the places he has visited. Indeed, photographic skills help him take nice images both academic and recreation purposes.